UNIVERSITY OF NOVA GORICA
GRADUATE SCHOOL

LOCAL COLLOCATION METHOD FOR PHASE-CHANGE PROBLEMS

MASTER'S THESIS

Robert Vertnik

Mentor: Prof. Dr. Božidar Šarler

Nova Gorica, 2007

Acknowledgements

My collaboration with Professor Božidar Šarler began when I was an undergraduate student at the Faculty of Mechanical Engineering, University of Ljubljana in year 2002. Research projects of industrial applications, such as continuous casting of steel and semi-continuous casting of aluminium alloys were immediately possessed me. After finishing my diploma, I joined his Laboratory for Multiphase Processes at the University of Nova Gorica and continued my research on phase-change problems and meshless numerical methods. I thank Professor Šarler for his support, guidance and to stimulate me finishing this thesis. His great deal of understanding is virtue.

I would also like to thank my life partner Ana and my son Maks for supporting me at my work and also to make me enthusiastic for other life things.

Further I thank my parents to guide me through my life and for understanding of my interest in computer science.

Local Radial Basis Function Collocation Method for Phase-Change Problems

Abstract

This thesis represents a new meshless method for the solution of the temperature field in the nonlinear convective-diffusive phase-change problems. The velocity field is assumed to be known. The method is based on multiquadric radial basis function collocation, made locally over a set of overlapping influence domains. Each influence domain is presented by usually five nodes, situated around of the central node. The strong formulation is used without any integration and time stepping is performed in an explicit way. The solution procedure for general transport equation is fully described. Five numerical examples are given with description, results and assessments. First, the diffusion boundary value problem is solved. Example is taken from the NAFEMS benchmark tests. The results are compared with the benchmark test, analytical solution and the results obtained by the finite difference method. Also the initial value problem of the diffusion is performed, analyzed and compared with the analytical solution and finite difference method. Next, the one-dimensional convective-diffusive problem with and without phase change is elaborated. Calculations are performed with different Péclet number, Stefan number, and material properties for solid and liquid phase. Results are compared with the analytical solution. The method is also used in solving the direct-chill semi-continuous casting model with temperature dependent material properties in Cartesian coordinates. The results are compared with the results obtained with the finite volume method. Last example represents an axisymmetric transient solution of the previous example with material moving boundaries (growing domain). The results are also compared with the finite volume method at different times. In all listed examples the calculations are made at different values of the multiquadric free parameter and number of nodes. In the first and fourth example the random displacement of nodes is used to show the ability of the developed meshless method of calculating partial differential equations on scattered node arrangements. This thesis confirms the suitability of using the developed method for numerical simulation of continuous casting processes.

Key words:

Lokalna kolokacijska metoda za večfazne probleme

Povzetek

Delo predstavlja novo brezmrežno metodo za izračun temperaturnega polja pri nelinearnih konvektivno-difuzivnih primerih s faznim prehodom, kjer je hitrostno polje vnaprej podano. Metoda je razvita na podlagi kolokacije z radialnimi baznimi funkcijami. Kolokacija je izvedena lokalno preko prekrivajočih se pod-domen, ki so predstavljene običajno s petimi točkami okoli središčne točke. Uporabljena je močna formulacija brez integracije in eksplicitno časovno diskretizacijo. Popolnoma je predstavljen rešitveni postopek generalne transportne enačbe. Podanih je pet numeričnih primerov s opisom posameznega primera, rezultati in raznimi primerjavami. Najprej je rešen problem robnih vrednosti difuzijske enačbe. Primer je vzet iz NAFEMS testnih primerov. Rezultati so primerjani z NAFEMS rešitvami, analitično rešitvijo in z rešitvami metode končnih razlik. Prav tako je rešen problem začetnih vrednosti difuzije, kjer so rezultati primerjani z analitično rešitvijo in z rešitvami metode končnih razlik. Nato je podan eno-dimenzijski konvektivno-difuzivni problem s faznim in prav tako brez faznega prehoda. Izračuni so bili izvedeni pri različnih Pécle-jevih in Štefan-ovih številih ter termofizikalnih lasnosti tekoče in trdne faze materiala. Rezultati so primerjani samo z analitično rešitvijo. Metoda je nato uporabljena na industrijskem primeru, in sicer pol-kontinuiranem ulivanju aluminijevih zlitin za brame s temperaturno odvisnimi termofizikalnimi lastnostmi. Rezultati so primerjani z metodo kontrolnih prostornin. Zadnji primer predstavlja časovno odvisni izračun prejšnjega primera v osno-simetričnem koordinatnem sistemu s premikajočo se robno mejo. Primerjava je prav tako izvedena z metodo končnih prostornin. Pri vsakem od naštetih primerov so vzete različne vrednosti prostega parametra radialnih baznih funkcij in različnim številom točk. V prvem in četrtem primeru so izvedeni izračuni z naključno postavljenimi točkami, s katerimi smo skušali prikazati sposobnost omenjene metode za izračun parcialne diferencialne enačbe na raztroseni razporeditvi točk. To znanstveno delo potrjuje primernost in uporabnost razvite numerične metode za simulacije kontinuirnih procesov ulivanja.

Ključne besede:

radialne bazne funkcije, lokalna kolokacija, fazni prehod, aluminijeve zlitine, pol-kontinuirano ulivanje

Contents

List of Figures

List of Tables

List of Symbols

Latin symbols

B	arbitrary differential operator on the boundary
c	multiquadric free parameter
c_A	solute concentration of species A
c_p	specific heat at constant pressure
c_{random}	random number
D_S	diffusion coefficient of solute atoms
$\underline{\mathbf{D}}$	diffusion tensor
f_i, g_i	function value
$f_\wp$	fraction of phase $\wp$
F	function
h	enthalpy
h_m	melting enthalpy
h_{TC}	heat transfer coefficient
k	thermal conductivity
k_{LS}	coefficient in the solidification models
K	number of the shape functions
L	arbitrary differential operator in the domain
$m_\wp$	slope of a line of phase $\wp$
$\mathbf{n}$	normal vector
N	number of points
p_x	Cartesian coordinate in x direction
p_y	Cartesian coordinate in y direction
$\mathbf{p}_i$	point p vector
Pe	Péclet number
r	radial distance between two points
r_0	maximum nodal distance in the influence domain
S	source
Ste	Stefan number
t	time

t_f	local solidification time
T	temperature
T_m	melting temperature
T_{ref}	reference temperature
T_{ste}	steady-state convergence margin
u	approximate solution
$\mathbf{u}$	column vector of solutions
$\mathbf{v}$	velocity vector
x, y	Cartesian coordinates

Greek symbols

α_i	expansion coefficient
α_t	Brody-Flemings constant
$\alpha_\wp$	thermal diffusivity
$\boldsymbol{\alpha}$	column vector of variables
β	extended multiquadric free parameter
δ	displacement factor
ϕ	transport variable
λ_a	dendrite arm spacing
ρ	density
ω	influence domain
ψ_i	radial basis function
Ψ	matrix of coefficients
Γ	boundary
Ω	domain
Υ	indicators
$\wp$	phase, $\wp = S, L$

Subscripts

ana	analytical solution
avg	average solution
i, j, k	counters
l	influence domain
L	liquidus
max	maximum value
min	minimum value
S	solidus

Superscripts

d   spatial dimension
D   Dirichlet boundary conditions
N   Neumann boundary conditions
R   Robin boundary conditions
V   volumetric

Acronyms

BEM   Boundary Element Method
GS   Gaussian
DAM   Diffuse Approximate Method
DC   Direct-Chill
FEM   Finite Element Method
FVM   Finite Volume Method
FDM   Finite Difference Method
IMQ   Inverse Multiquadric
LRBFCM   Local Radial Basis Function Collocation Method
MQ   Multiquadric
NAFEMS   National Agency for Finite Element Methods & Standards
PDE   Partial Differential Equation
RBF   Radial Basis Function
RBFCM   Radial Basis Function Collocation Method
RMS   Root Mean Square Error
TPS   Thin Plate Spline

1 Introduction

A large number of technically important problems in materials processing involve phase-change phenomena. Phase change or phase transition is the transformation of a thermodynamic system from one phase to another, typically from liquid to solid, solid to solid, or gas to solid, etc. Most important phase transformation in materials processing is from liquid to solid where products are produced through solidification processes, such as for example, direct-chill casting of aluminium alloys. The prediction of the behaviour of this systems is highly challenging due to the involved strongly coupled phase-change kinetics, transport and solid mechanics effects, occurring on different length scales. They are often defined by the nonlinear partial differential equations (PDEs), nonlinear boundary conditions and temperature dependent thermo-physical properties. As a result, the analytical solution of the solidification problems are not possible to obtain, particularly in the complex-shaped cases. In order to find their solution, the numerical methods have to be employed.

The numerical solutions of the problems in science and engineering have been dominated by either finite difference method (FDM) [Özisik, 1994], finite element method (FEM) [Zienkiewicz, 2000], finite volume method (FVM) [Hong, 2004], and boundary element method (BEM) [Šarler and Kuhn, 1998a and 1998b]. Despite the powerful features of these methods, there are often substantial difficulties in their application to realistic, geometrically complex three dimensional transient situations with moving and/or deforming boundaries. A common problem in the mentioned methods is the need to create a polygonization (mesh) to support the localized approximants, either in the domain and/or on its boundary. Another property is that low order approximations are usually used which lead to un-accurate solution of the spatial derivatives. To overcome this difficulty, the refinement (re-meshing) of the discretization must be, used which is often the most time consuming part of the solution process and is far from being fully automated.

In recent years the "meshless methods" have become a useful alternative for solving the PDEs. This methods do not require polygonization but use only a set of nodes to approximate the solution. The rapid development of these types of

meshless (meshfree, polygon-free, mesh-reduction) methods and their classification is elaborated in the very recent monographs [Atluri and Shen, 2002; Liu, 2003; Atluri, 2004; Šarler, 2004; Liu and Gu, 2005]. A broad class of meshless methods in development today are based on Radial Basis Functions (RBFs) [Buhmann, 2003]. The RBF collocation method (RBFCM) or Kansa method [Kansa, 1990a and 1990b] is the simplest of them.

In this work, the Local Radial Basis Function Collocation Method (LRBFCM) is developed for solving the diffusion and convection-diffusion equation with phase change, nonlinear material properties and boundary conditions. Phase-change phenomena with mathematical formulations is presented in the Chapter 2. The Chapter 3 introduces the collocation with RBF. The RBF interpolation procedure, which is the crucial part of the developed LRBFCM, is presented and compared with the polynomial interpolation procedure. One example is given, where the multiquadric radial basis function (MQ-RBF) is used with the variable free parameter. The Chapter 4 presents the developed LRBFCM in its detail. Two approaches are explained to overcome the problem of setting the optimal free parameter. In Chapter 5, the solution procedures for all governing equations are presented. And finally, in Chapter 6, the numerical examples are given with a problem description, governed equations, results and comparisons. To analyze the convergence and accuracy of the developed method we used reference analytical solutions, FDM and FVM solutions, all coded in Laboratory for Multiphase Processes.

Our previous work

In the Laboratory for Multiphase Processes, numerous numerical methods were used to find the solution of various solidification processes, such as continuous casting of steel and direct-chill casting of aluminium alloys. First, the FVM (the representative of the mesh methods) was used to calculate the temperature field in the continuous casting of steel [Šarler, 1996] and direct-chill (DC) semi-continuous casting of alluminum alloys [Šarler and Mencinger, 1999]. The DC casting process was further calculated by the dual reciprocity boundary element method (DRBEM) [Šarler and Kuhn, 1998a and 1998b; Šarler and Mencinger, 1999], which belongs to the semi-mesh methods. The scaled augmented thin plate splines were used for transforming the domain integrals into a finite series of boundary integrals. First truly meshless method developed for calculating the temperature field in DC casting process was the Diffuse Approximate Method (DAM) [Vertnik *et al.*, 2004]. The axisymmetric steady-state convective-diffusive thermal field problem was solved on the basis of moving least square

approximation with the polynomial basis functions. At least six polynomial basis functions and nine neighbor nodes must be used to successfully calculate the derivates of the second-order PDE. Despite the good accuracy and ability to solve the PDE on complex geometry, the need for even simpler meshless version was identified. Since, the polynomial basis functions can not be used for collocation (interpolation) of scattered data, the RBF was chosen. The LRBFCM was developed and successfully used for calculating two-dimensional diffusion problem [Šarler and Vertnik, 2006] and phase-change problems [Vertnik and Šarler, 2006]. The method was further upgraded to calculate the solution of transient DC casting problem with simultaneous material and phase-change interface moving boundaries [Vertnik *et al.*, 2006].

2 Physical background

A large number of applications in materials processing are described as a heat transfer problem involving melting or solidification. Representative applications include such technologies as crystal growth, continuous casting, shape casting, welding, etc. They generally refer as phase-change or moving boundary problems. In these type of problems, the boundary of the domain is not known in advance but has to be determined as part of the solution. It is time-dependent problem where the position of the boundary is a function of time and space.

First, the basic concept of the phase-change phenomena is explained for pure materials and alloys. Simple binary phase-change diagram and some models are presented for evaluating the relation between the solid fraction and temperature. Next, two different numerical formulations of the phase-change solution are presented: multiple-domain formulation and one-domain formulation. The general characteristics of both methods are given.

2.1 Phase-change phenomena

Heat transfer problems involving melting or solidification are generally referred to as phase-change or moving boundary problems, and also as Stefan problems. Melting is the phenomena, where solid phase is changed into liquid, by absorbing heat energy. Solidification is the inverse phenomena of melting, where liquid phase is change to solid, by releasing heat energy. Absorbed or released heat energy is often termed as latent heat of melting or latent heat of solidification, which determines the melting or solidification velocity.

For pure substances or eutectic alloys, the phase-change phenomena occurs at a fixed single temperature, called the melting point temperature T_m. When the temperature of substance is equal to melting temperature, phase change commences. At this stage, the latent heat is absorbed to material or released from material to change its phase. During the melting or solidification, liquid and solid are in thermodynamic equilibrium, and the temperature of the substance

5

does not change. The solid and the liquid phases are separated by only one moving interface which determines the boundary between phases.

In the case of alloys, melting or solidification takes place over an extended range of temperature, where the solid and liquid phases are separated by a two-phase moving interface, the 'mushy zone'. The upper limit of this temperature range at which the mixture becomes completely liquid is termed as liquidus temperature T_L and the lower limit at which solidification is complete and the mixture is entirely solid is termed as the solidus temperature T_S. The mass fraction of the solid phase (solid fraction) in the mixture, f_s, is zero at T_L and unity at T_S, and in the mushy zone has values between zero and unity. The relation between the solid fraction and temperature may be evaluated from the phase-change diagrams, shown in Figure 2.1, where temperature is presented as a function of solute concentration c_A. For any given solute concentration, there exists an equilibrium liquidus and solidus temperature. Likewise, for any given temperature, there is an equilibrium solidus solute concentration $c_{A,S}$ and liquidus solute concentration $c_{A,L}$. The liquidus or solidus temperature can be approximated by the following equation

$$T_\wp = T_m + m_\wp c_{A,\wp} \, ; \ \xi = L, S \,, \tag{2.1}$$

where $m_\wp$ is the slope of the liquidus or solidus line at $c_{A,\xi}$.
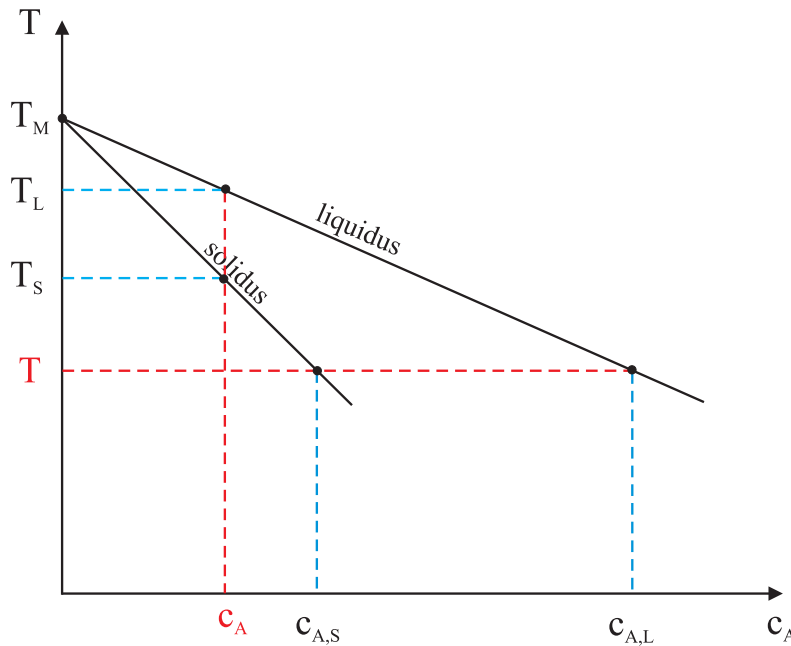
Figure 2.1: Binary phase-change diagram.

More detailed description of physical phenomena can be found in the following literature [Crank, 1984; Dantzig, 2001 and Šarler, 1995].

The relation between solid fraction and the temperature in practical solidification analyzes can be evaluated by the several models [Hong, 2004]:
a) Level rule (equilibrium solidification model)
Complete mixing of solute in liquid and solid is assumed. The solid fraction as a function of temperature (see Figure 2.1) is given by

$$f_S = \frac{T_L - T}{(1 - k_{LS})(T_m - T)} \qquad (2.2)$$

where k_0 is defined as

$$k_{LS} = \frac{c_{A,S}}{c_{A,L}} . \qquad (2.3)$$

b) Scheil model
Complete mixing of solute in liquid and no mixing in solid are assumed. In this case the solid fraction as a function of temperature is given by

$$f_S = 1 - \left(\frac{T_m - T}{T_m - T_L} \right)^{\frac{1}{(k_{LS} - 1)}} . \qquad (2.4)$$

c) Brody-Flemings model
Complete mixing in liquid and some mixing in solid are assumed. Here, the solid fraction as a function of temperature is given by

$$f_S = (1 + \alpha_t k_{LS}) \left[1 - \left(\frac{T_m - T_L}{T_m - T} \right)^{\frac{1}{(k_{LS} - 1)}} \right] \qquad (2.5)$$

where α_t is the Brody-Flemings constant and it is defined as

$$\alpha_t = \frac{4 D_s t_f}{\lambda_a^2} . \qquad (2.6)$$

In the equation (2.6) D_S, t_f and λ_a is diffusion coefficient of solute atoms in solid, the local solidification time and the dendrite arm spacing, respectively.

d) Linear distribution of latent heat

When f_S cannot easily be evaluated as a function of temperature since phase diagrams are not known for certain multi-component alloys, it is sometimes assumed that the latent heat is linearly distributed over the solidification range between T_L and T_S.

$$f_S = \frac{T_L - T}{T_L - T_S}.$$
(2.7)

In this thesis, only the latter model is used since in continuous casting of aluminium alloys the multi-component alloys are used where the phase diagrams are knot known in advance.

2.2 The multiple-domain formulation

The multiple-domain formulation uses independent conservation equations for each phase and couples them with appropriate boundary conditions at the phase-change interface. In the most simple cases, where the Fourier heat conduction equation is used for each phase and the density is constant and equal for all phases, the governing equations are defined as

heat transfer in solid

$$\rho c_{pS} \frac{\partial T_S}{\partial t} = \nabla \cdot (k_S \nabla T_S),$$
(2.8)

heat transfer in liquid

$$\rho c_{pL} \frac{\partial T_L}{\partial t} = \nabla \cdot (k_L \nabla T_L) \text{ and}$$
(2.9)

boundary condition at the solid-liquid interface

$$k_S \nabla T_S \cdot \mathbf{n}_{SL} - k_L \nabla T_L \cdot \mathbf{n}_{SL} = \rho h_m \mathbf{v} \cdot \mathbf{n}_{SL}.$$
(2.10)

where $\mathbf{n}_{SL}$ is the unit normal on the phase interface, $\mathbf{v}$ is velocity of the interface and h_m is the latent heat per unit mass of solid. The unit normal is pointing from the solid into the liquid (see Figure 2.2a).
For a number of simple geometries and conditions analytical and approximate solutions can be constructed [Crank, 1984; Šarler, 1995]. From the numerical point of view, the solution requires an explicit tracking of the solid-liquid interface, where the grid or mesh must be adopted or transformed in a such way, that the solid-liquid interface is always on a grid line or is fixed in the transformed domain [Crank, 1984; Minkowycz and Sparrow, 1997].

2.3 The one-domain formulation

The one-domain formulation of solid-liquid phase-change problems is based on the mixture enthalpy variable

$$h = \frac{\left(f_S^V \rho_S h_S + f_L^V \rho_L h_L \right)}{\rho}, \tag{2.11}$$

where the constitutive temperature-enthalpy relationships h_S and h_L are

$$h_S = \int_{T_{ref}}^{T} c_S dT \text{ and} \tag{2.12}$$

$$h_L = \int_{T_{ref}}^{T_S} c_S dT + \int_{T_S}^{T_L} c_L dT + h_m = h_S(T) + \int_{T_S}^{T} (c_L - c_S) dT + h_m, \tag{2.13}$$

respectively [Šarler and Kuhn, 1998a]. In terms of enthalpy, the multiple region formulation (equations (2.8)-(2.10)) is reduced into a single equation

$$\frac{\partial}{\partial t}(\rho h) = \nabla \cdot (k \nabla T). \tag{2.14}$$

Conservation holds in all phases (Figure 2.2b) and implicitly includes the boundary condition at the phase-change interface.

In continuation of this thesis, a continuum conserved equation for binary solid-liquid phase-change systems [Bennon and Incropera, 1987; Založnik, 2006] is used

$$\frac{\partial}{\partial t}(\rho h) + \nabla \cdot (\rho \mathbf{v} h) = \nabla \cdot (k \nabla T) + \nabla \cdot \left(\rho \mathbf{v} h - f_S^V \rho_S \mathbf{v}_S h_S - f_L^V \rho_L \mathbf{v}_L h_L \right), \tag{2.15}$$

where the second term on the right-hand side is a correction term, needed to accommodate the mixture formulation of the convective term. In next we neglect this term. In equation (2.15) mixture density and thermal conductivity are defined as

$$\rho = f_S^V \rho_S + f_L^V \rho_L \text{ and} \tag{2.16}$$

$$k = f_S^V k_S + f_L^V k_L, \tag{2.17}$$

where $f_\wp^V$ represents the volume fraction of the phase $\wp$. The liquid volume fraction f_L^V is assumed to vary from 0 to 1 between solidus T_S and liquidus temperature T_L. Mixture velocity is defined as

$$\mathbf{v} = \frac{\left(f_S^V \rho_S \mathbf{v}_S + f_L^V \rho_L \mathbf{v}_L \right)}{\rho} \ . \tag{2.18}$$

From the numerical point of view, the main advantage of this formulation is that a solution does not require an explicit tracking of the solid-liquid interface. On the other hand, this formulation requires very dense discretization in the vicinity of the phase-change interface.
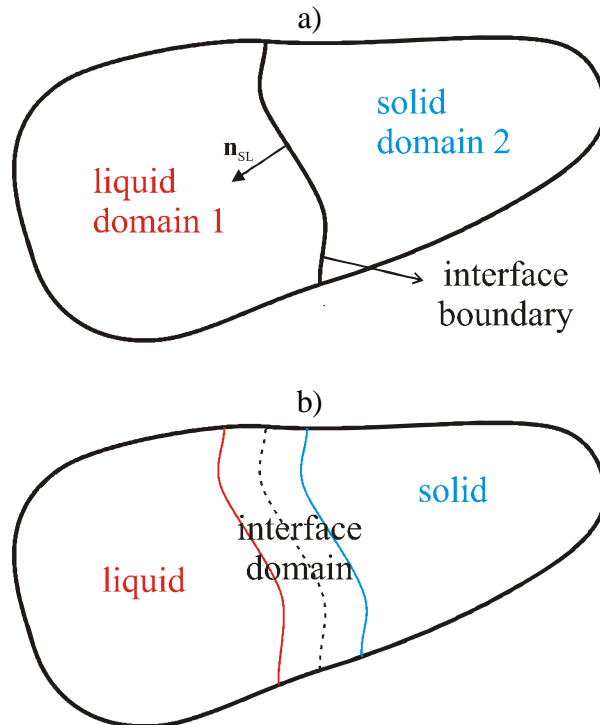
Figure 2.2: Graphic representation of two different formulations. a) two-domain formulation and b) one-domain formulation.

3 Introduction to collocation with RBF

RBF approximations have been shown to be most useful in many scientific and technological applications. Purposes and applications of such approximations and particular of interpolation are manifold. This chapter represents the RBFCM for interpolating scattered data and for solving the PDE problems. First, some of the most important types of radial basis functions are presented. Next, the RBFCM for interpolating scattered data is fully described and compared with the picewise polynomial interpolation technique. The comparison is presented on a one-dimensional case with the variable free parameter of the MQ-RBF.

The RBFCM, also named as Kansa method, has become very attractive for solving the PDE problems [Kansa, 1990a and 1990b]. Its local version is derived in Chapter 4 and used in numerical examples in this thesis. For better insight of local version, the Kansa method is shortly explained.

More detailed description of the RBF methods can be found in recent monographs [Buhmann, 2003; Liu, 2003; Liu ang Gu, 2005].

3.1 Radial basis functions

Radial basis functions can be expressed in the following form

$$\psi_i(r) = \psi(\mathbf{p} - \mathbf{p}_i) \, ; \, \psi_i : \mathbb{R}^d \to \mathbb{R} \, , \tag{3.1}$$

and depends only on the distance between vector point $\mathbf{p} \in \mathbb{R}^d$ and the fixed vector point $\mathbf{p}_i \in \mathbb{R}^d$ ($\mathbf{p}_i$ is usually called the center) and are radially symmetric. This means that any rotation makes no difference to the function value. This explains the term *radial*. In equation (3.1), $\mathbb{R}$ represents real number, d spatial dimension and r radial distance.

For two-dimensional Cartesian system vector point $\mathbf{p}$ is represented by

$$\mathbf{p} = p_x \mathbf{i}_x + p_y \mathbf{j}_y , \tag{3.2}$$

where p_x, p_y are the Cartesian coordinates and $\mathbf{i}_x$, $\mathbf{j}_y$ base vectors of the vector point $\mathbf{p}$. The radial distance between two vectors is defined by the Euclidean norm

$$r = \|\mathbf{p} - \mathbf{p}_i\| = \sqrt{(p_x - p_{x,i})^2 + (p_y - p_{y,i})^2} . \tag{3.3}$$

To explain *basis function* part, lets suppose we have fixed certain vector points (called centers) $\mathbf{p}_1,...,\mathbf{p}_N \in \mathbb{R}^d$ and the following function $F(\mathbf{p})$ which is represented as a linear combination of the function ψ centered at the points $\mathbf{p}_i$

$$F(\mathbf{p}) = \sum_{i=1}^{N} \alpha_i \psi_i (\mathbf{p}) ; \ \psi_i (\mathbf{p}) = \psi(\mathbf{p} - \mathbf{p}_i) . \tag{3.4}$$

So we have composed a function $F(\mathbf{p})$ which is in the function space spanned by the basis functions $\psi_i(\mathbf{p})$.
Some commonly used forms of radial basis function are:

- Gaussian (GA) (Figure 3.1a)

$$\psi(r) = e^{-(cr)^2} , \tag{3.5}$$

- multiquadric (MQ) (Figure 3.1b)

$$\psi(r) = \sqrt{r^2 + c^2} , \tag{3.6}$$

- inverse multiquadric (IMQ) (Figure 3.1c)

$$\psi(r) = \frac{1}{\sqrt{r^2 + c^2}} \text{ and} \tag{3.7}$$

- thin plate spline (TPS) (Figure 3.1d)

$$\psi(r) = r^{2c} \log(r) . \tag{3.8}$$

a)   b)

c)   d)
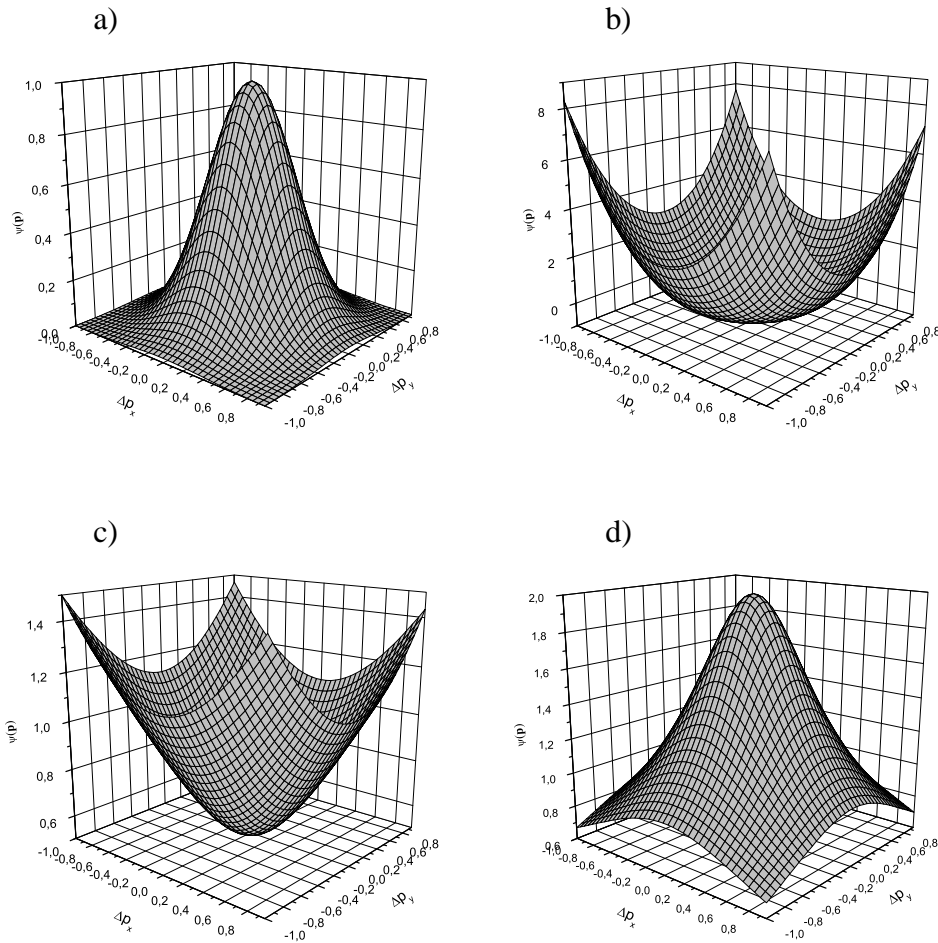
Figure 3.1: Some of the most commonly RBFs. a) GA-RBF, b) TPS-RBF, c) MQ-RBF, and d) IMQ-RBF. All functions are calculated with the free parameter $c = 0.5$.

In all examples in this thesis, only the MQ-RBF is used. The choice was made on the basis of multivariate interpolation tests [Franke, 1982], were the best accuracy was found with MQ-RBFs. This functions include the free parameter c, which has to be set by the user. Since there is no mathematical background for its determination, the parameter is chosen based on the numerical experiments. The MQ-RBF is plotted in Figure 3.2 as a function of the free parameter.
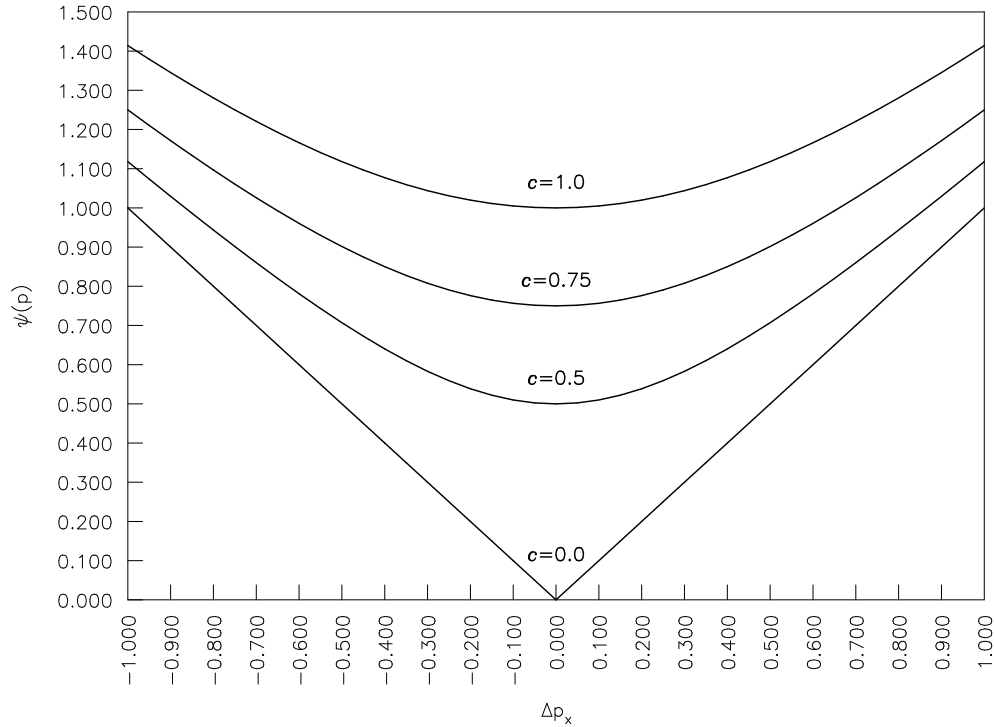
Figure 3.2: MQ-RBF with different values of the free parameter.

3.2 Radial basis function collocation method for interpolating scattered data

A problem frequently occurring in science and engineering is the approximation of a function F, the value of which is known only on a relatively small set of points. One way to obtain such an approximation is by interpolation. For one-dimensional problems, many methods exist for solving this problem. Most of them (e.g. polynomial and piecewise polynomial splines) involve the same general idea: for a given set of N data points $p_{x_1}, ..., p_{x_N} \in \mathbb{R}$ and corresponding data values $f_1, ..., f_N \in \mathbb{R}$, a set of basis functions $\psi_1(p_x), ..., \psi_N(p_x) \in \mathbb{R}$ is chosen such that a linear combination of these functions satisfies the interpolation conditions. To be more specific, a function $F(p_x)$ is sought of the form

$$F(p_x) = \sum_{i=1}^{N} \alpha_i \psi_i(p_x),$$ (3.9)

such that $F(p_{x_i}) = f_i$ for $i = 1, ..., N$. The interpolation conditions lead to a linear system of equations which determines the expansion coefficients α_i

$$\sum_{i=1}^{N} \alpha_i \psi_i \left(p_x \right) = f_i \, , \; i = 1, ..., N \, . \tag{3.10}$$

Procedure is also represented as a block diagram in Figure 3.3. For many choices of basis functions $\psi_i \left(p_x \right)$, this linear system is guaranteed to be non-singular whenever the data points $p_{x_1}, ..., p_{x_N} \in \mathbb{R}$ are distinct.

For data sets in more than one-dimension, the prescribed approach with polynomial basis (independent of the data points) no longer works. It can be shown that there exists distinct data sets, for which linear system of equation for determining the expansion coefficients becomes singular. (i.e. there does not exist an interpolator in the form of equation (3.9)). However, with piecewise polynomial splines, it is possible to interpolate data in two and three dimensions. This technique works very well for gridded or otherwise highly regularly distributed data sets. For scattered data sets, we usually need a triangulation, which is not a trivial task for complex two and especially for three dimensional problems. The reason for this is that it has to be decided where the pieces of the piecewise polynomials lie and where they are joined together. Moreover, it then has to be decided an smoothness they are joined together at common vertices, edges etc. and how that is done.

Instead of taking linear combinations of a set of basis functions that are independent of the data points, one takes a linear combination of translates of a single basis function that is radially symmetric about its center. This approach, pioneered by Hardy [Hardy, 1971], is referred to as the MQ method. Hardy used MQ-RBF as the basis function to solve a problem from cartography. Namely, given set of sparse, scattered measurements from some source points on a topographic surface, construct a "satisfactory" continuous function that represents the surface.

The RBFCM is a generalized version of the Hardy's MQ method, and is defined as follows: Given a set of N distinct data points $\mathbf{p}_1, ..., \mathbf{p}_N \in \mathbb{R}^d$ and corresponding data values $f_1, ..., f_N \in \mathbb{R}$, the RBF interpolator is given by

$$F \left(\mathbf{p} \right) = \sum_{i=1}^{N} \alpha_i \psi \left(r_i \right); \; r_i = \left\| \mathbf{p} - \mathbf{p}_i \right\|, \tag{3.11}$$

where $\psi \left(r_i \right)$ is some radial function and $\left\| \cdot \right\|$ is the Euclidean norm (3.3). The expansion coefficients α_i are determined from the interpolation conditions

$$F \left(\mathbf{p}_i \right) = f_i \, , \; i = 1, ..., N \, , \tag{3.12}$$

which leads to the following linear system of equations

$$\mathbf{\Psi \alpha} = \mathbf{u} \, , \tag{3.13}$$

where the components of $\mathbf{\Psi}$ are given by $\Psi_{i,j} = \psi\left(\left\|\mathbf{p}_i - \mathbf{p}_j\right\|\right)$. The whole procedure is also represented in 1D as a block diagram in Figure 3.4. The method has the ability to handle arbitrarily scattered data, to be easily generalized to several space dimensions, and to provide spectral accuracy. Respectively, the method become very popular in several different types of applications. Some of these applications include cartography, neural networks, medical imaging (Figure 3.8), surface fitting (Figure 3.5 and Figure 3.6), surface reconstruction (Figure 3.7), and the numerical solution of PDEs (examples in this thesis).

for a given set of N data nodes

$$p_{x_1}, ..., p_{x_N} \in \mathbb{R}$$

and function values

$$f_1, ..., f_N \in \mathbb{R}$$

a set of polynomial basis functions is chosen

$$\psi_1(p_x), ..., \psi_N(p_x) \in \mathbb{R}$$

linear combination of basis functions

$$F(p_x) = \sum_{i=1}^{N} \alpha_i \psi_i(p_x)$$

and the interpolation conditions are set

$$F(p_{x_i}) = f_i, \ i = 1, ..., N$$

a linear system of equations is solved

$$\sum_{i=1}^{N} \alpha_i \psi_i(p_x) = f_i, \ i = 1, ..., N$$
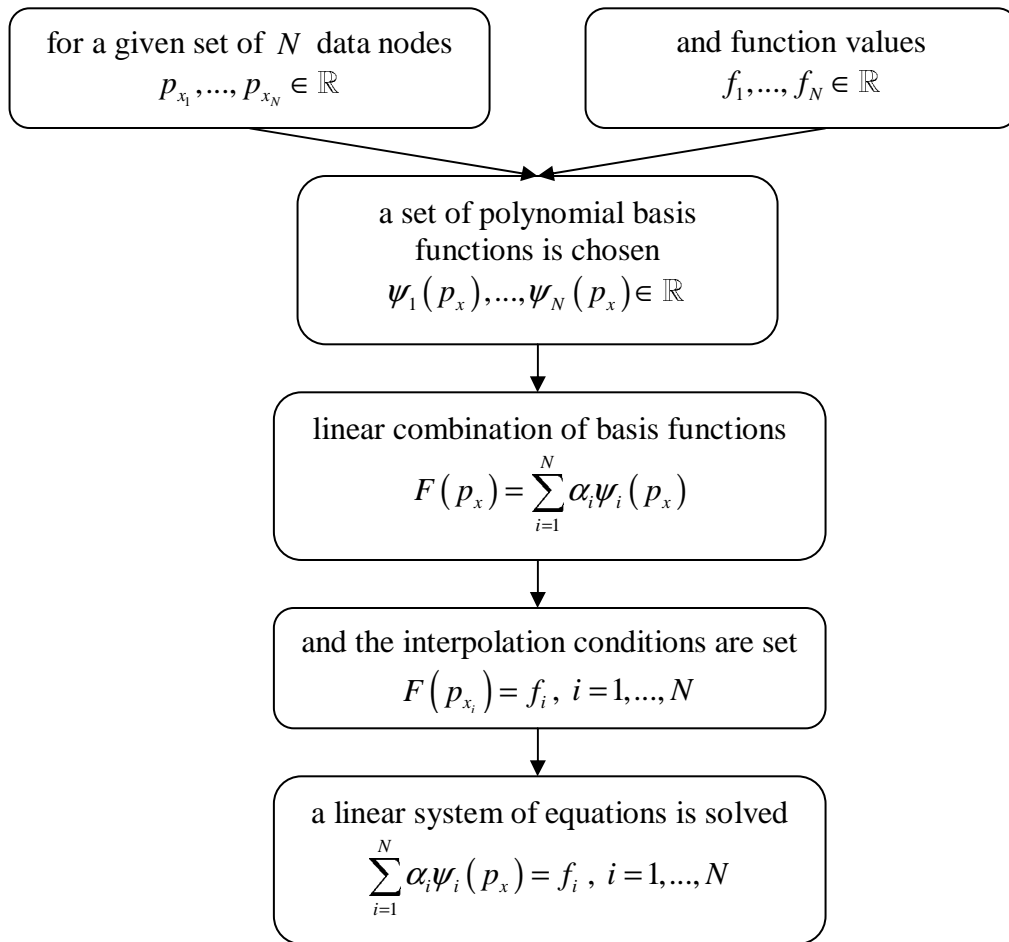
Figure 3.3: Block diagram of the polynomial interpolation in 1D.

for a given set of N data nodes
$$p_{x_1}, ..., p_{x_N} \in \mathbb{R}$$

and function values
$$f_1, ..., f_N \in \mathbb{R}$$

a single basis function is chosen
$$\psi\left(\left\|p_x - p_{x_i}\right\|\right) \in \mathbb{R}$$

linear combination of basis functions
$$F(p_x) = \sum_{i=1}^{N} \alpha_i \psi_i\left(\left\|p_x - p_{x_i}\right\|\right)$$

and the interpolation conditions are set
$$F\left(p_{x_i}\right) = f_i, \quad i = 1, ..., N$$

a linear system of equations is solved
$$\sum_{i=1}^{N} \alpha_i \psi\left(\left\|p_x - p_{x_i}\right\|\right) = f_i, \quad i = 1, ..., N$$
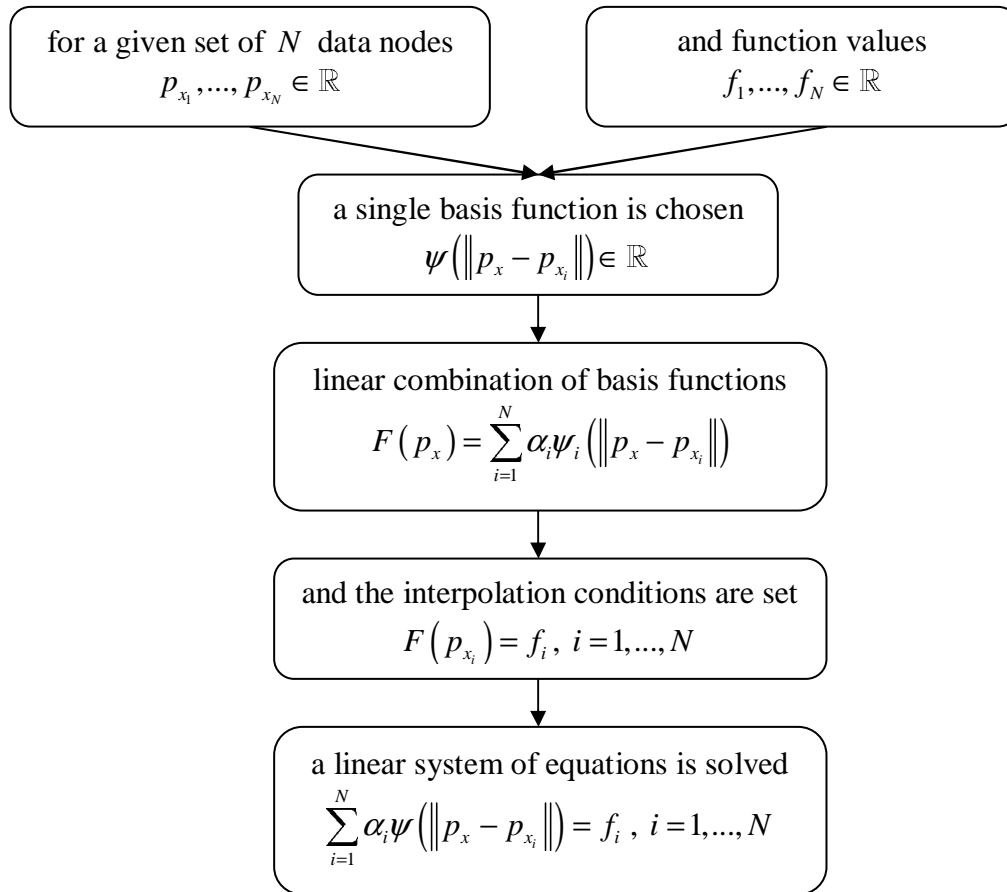
Figure 3.4: Block diagram of the RBF interpolation in 1D.

Figure 3.5: Surface fitting problem. Left picture - raw point-cloud from a LIDAR scan of the Statue of Liberty, right picture - surface, reconstructed by the RBF interpolation. The few viewpoints, oblique scanning angles and large gaps make this a difficult problem for other techniques [Carr *et al.*, 2003].
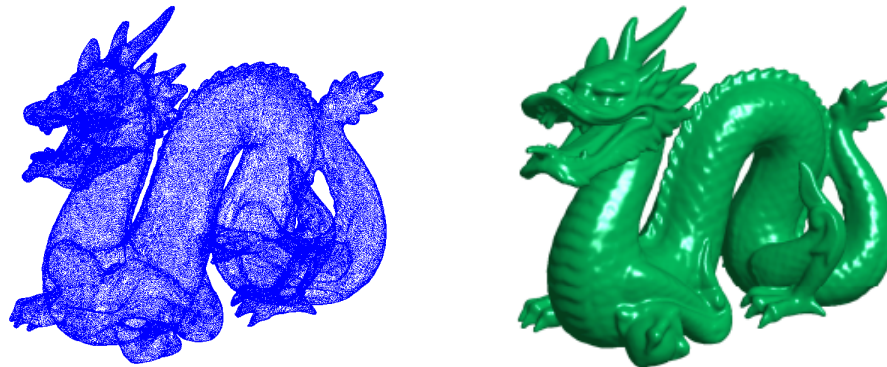
Figure 3.6: Fitting a RBF to a 438.000 point-cloud [Carr *et al.*, 2001].
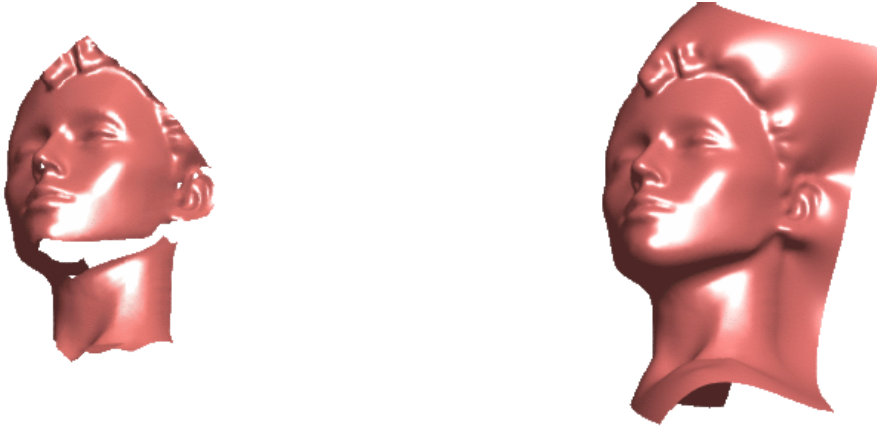
Figure 3.7: Automatic mesh repair [Carr *et al.*, 2001].
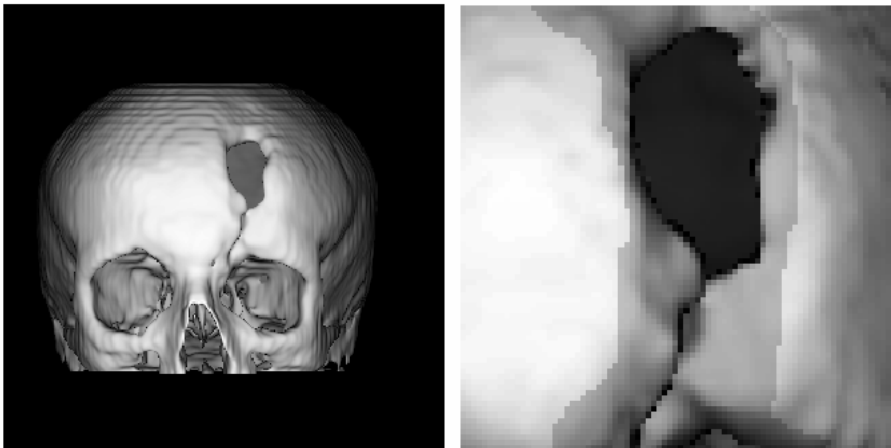
Figure 3.8: Medical imaging example [Carr *et al.*, 1997].

3.2.1 Example of interpolation with RBFCM

An example of interpolation for one-dimensional data set (Table 3.1) is presented to compare and show the effect of the free parameter of RBFs. We choose the MQ-RBF and vary the free parameter from 0.0 to 22.0.

Table 3.1: Function values of the example data set.

i	p_{xi}	$f_i(p_x)$
1	0.0	0.0000
2	1.0	0.8415
3	2.0	0.9093
4	3.0	0.1411
5	4.0	-0.7568
6	5.0	-0.9589
7	6.0	-0.2794

Figures 3.9 and 3.10 represent the interpolation results obtained with the polynomial interpolation and interpolation with RBFs. The comparison between both methods is made where the polynomial one is treated as analytical or reference solution. The numerical results are presented in Table 3.2, where the average and maximum errors are given as a function of c. Errors were calculated at 600 nodes, regularly distributed between 0.0 and 6.0. The average error is also plotted in Figure 3.11. On the basis of results, the following conclusions can be made:

- With the increasing of the c the accuracy of the results becomes better and converges to results obtained by polynomial interpolation. The errors monotonically diminish as shown in Table 3.2 and Figure 3.11. This conclusion is valid when the condition $c \geq 4.0$ is satisfied.
- Previous conclusion is expected to be valid for all values of c. However in this example, the values of c from 1.0 to 3.0 gives smaller errors than at $c = 4.0$. The reason is in the shape of the polynomial interpolated function, which can be fitted well with the RBFs at mentioned values of c. This phenomena is somehow exception in this example, but can be observed in other cases too (see Chapter 6).
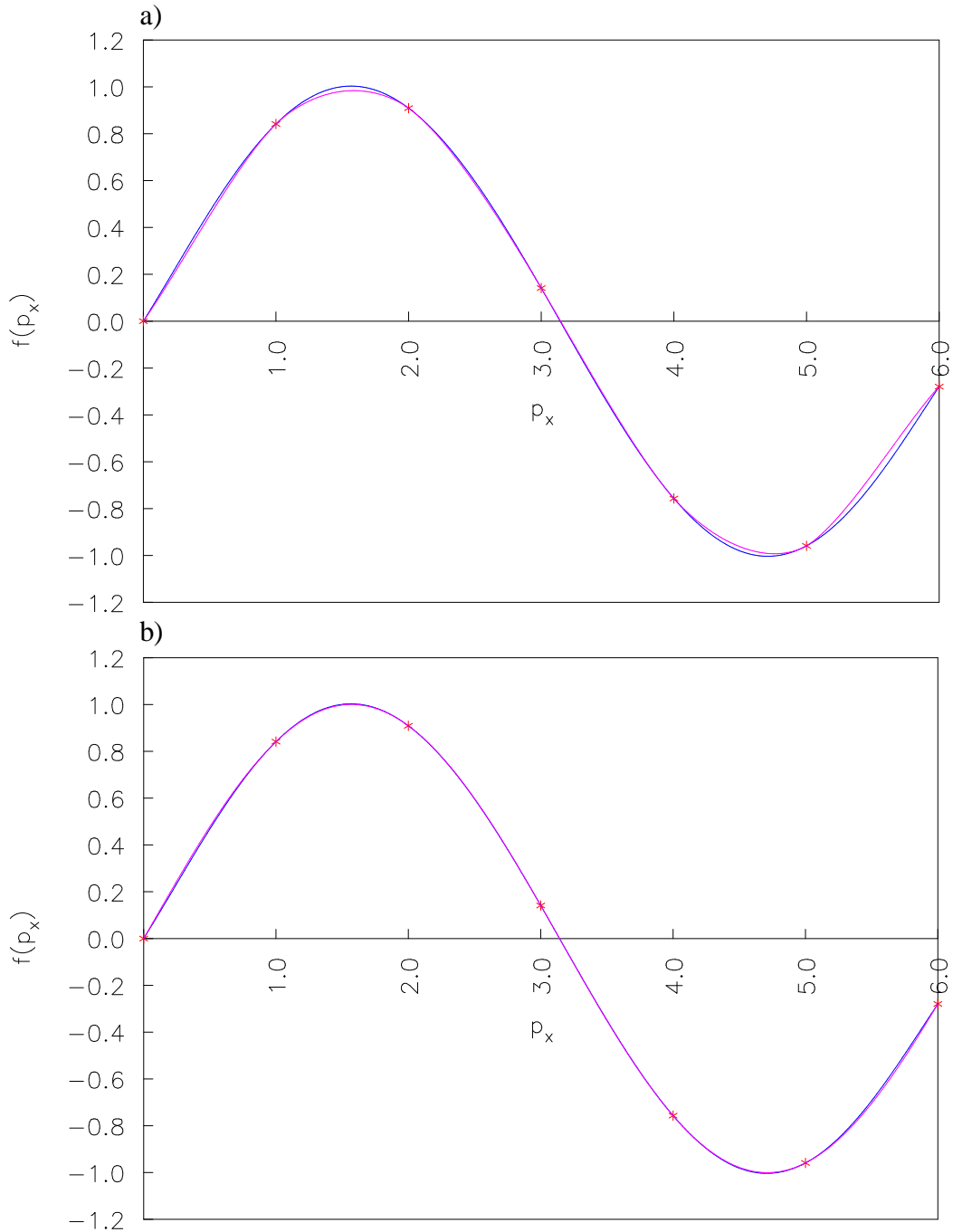
Figure 3.9: Effect of the MQ free parameter. a) $c = 0.0$, b) $c = 10.0$. Blue solid line – polynomial interpolation. Red solid line – RBF interpolation. Red stars represent the function values.

a)

b)
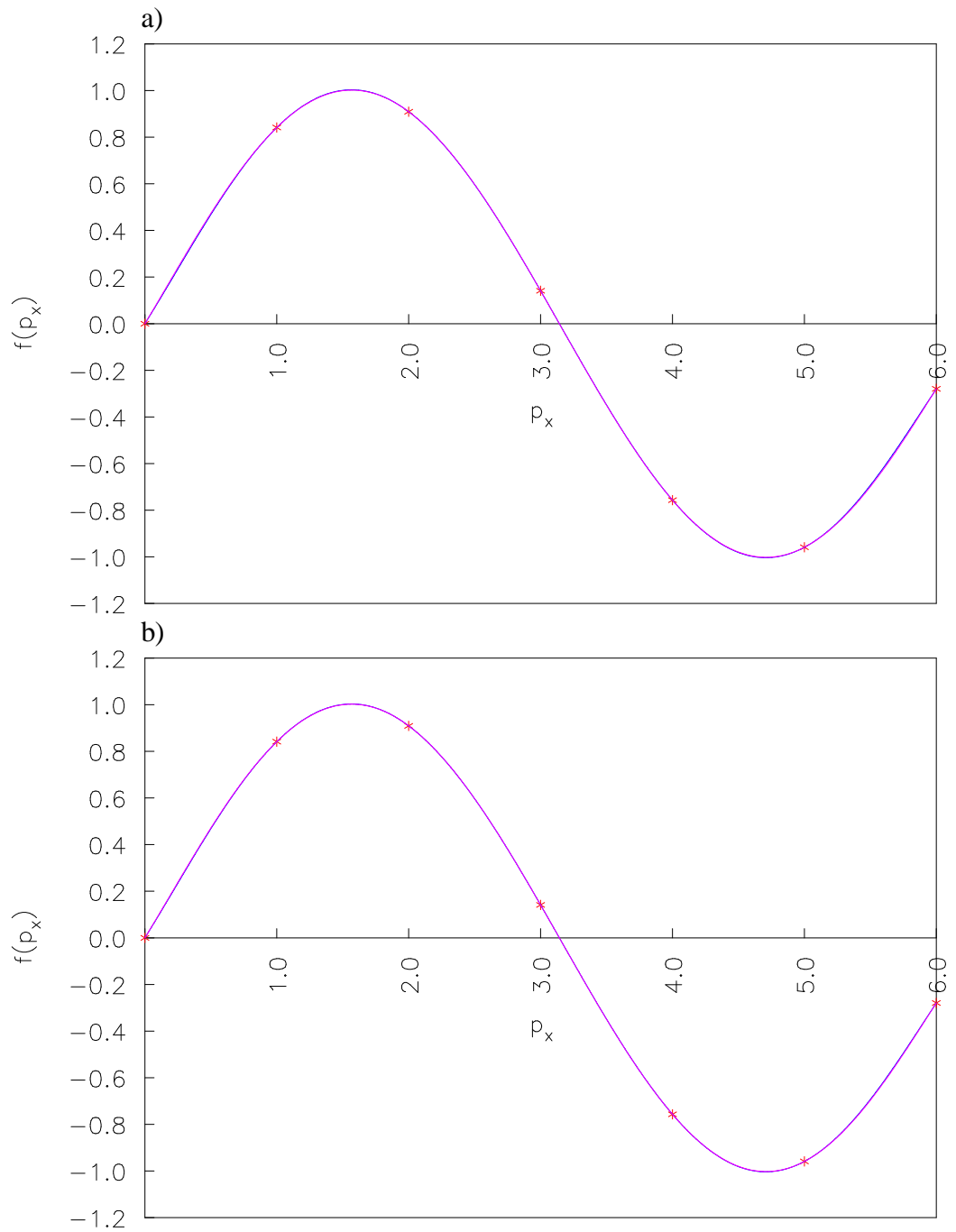
Figure 3.10: Effect of the MQ free parameter. a) $c = 15.0$, b) $c = 20.0$. Blue solid line – polynomial interpolation. Red solid line – RBF interpolation.

Table 3.2: Average and maximum error as a function of free parameter.

c	Δf_{avg}	Δf_{max}
0.0	0.0171	0.0438
1.0	0,0028	0,0142
2.0	0,0038	0,0181
3.0	0,0069	0,0240
4.0	0,0075	0,0252
5.0	0,0070	0,0244
6.0	0,0062	0,0221
7.0	0,0054	0,0195
8.0	0,0046	0,0170
9.0	0,0040	0,0148
10.0	0,0034	0,0128
11.0	0,0030	0,0112
12.0	0,0026	0,0098
13.0	0,0023	0,0087
14.0	0,0020	0,0077
15.0	0,0018	0,0069
16.0	0,0016	0,0061
17.0	0,0014	0,0055
18.0	0,0013	0,0050
19.0	0,0012	0,0045
20.0	0,0011	0,0041
21.0	0,0010	0,0039
22.0	0,0009	0,0034
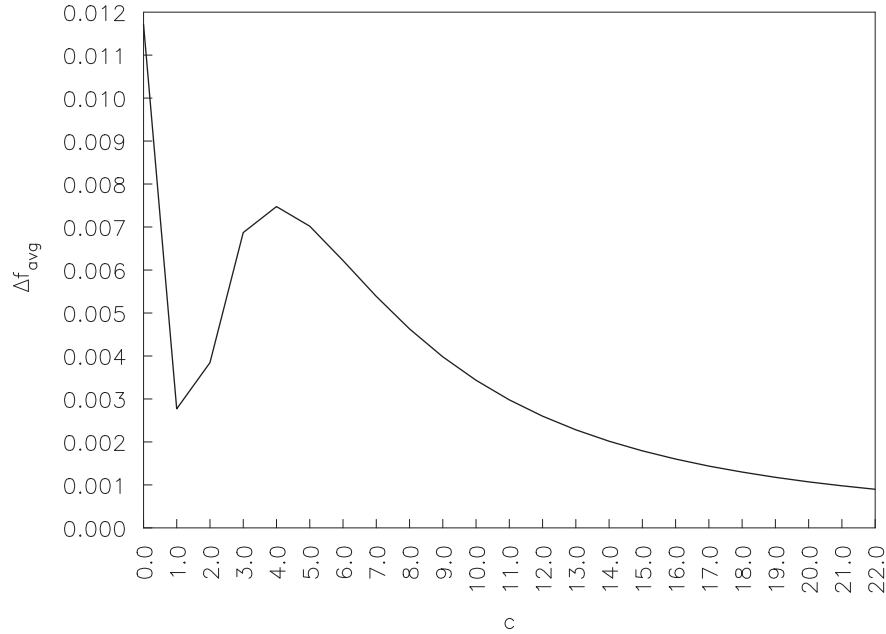
Figure 3.11: Average error as a function of free parameter.

3.3　Radial basis function collocation method (Kansa) for solving PDEs

In recent years radial basis function collocation method become a useful alternative to FDM and FEM for solving partial differential equations. We are going to focus on pure collocation method which was first introduced by Kansa [Kansa, 1990a and 1990b]. In this method, the PDE and the boundary conditions are satisfied by collocation.

Consider a general boundary value problem

$$Lu(\mathbf{p}) = f(\mathbf{p}) \text{ in } \Omega \in \mathbb{R}^d \text{ and} \tag{3.14}$$

$$Bu(\mathbf{p}) = g(\mathbf{p}) \text{ in } \Gamma \in \mathbb{R}^d, \tag{3.15}$$

where L and B are arbitrary differential operators in the domain Ω and on boundary Γ, respectively. The operator B can specify Dirichlet, Neumann, Robin, or mixed boundary conditions

To solve the problem as given in equations (3.14) and (3.15), we use N collocation points in Ω, where $\mathbf{p}_1,...,\mathbf{p}_{N_\Omega}$ are interior nodes, and Γ, where $\mathbf{p}_{N_\Omega+1},...,\mathbf{p}_{N_\Omega+N_\Gamma}$ are boundary nodes. Typical node arrangement is shown in Figure 3.12.
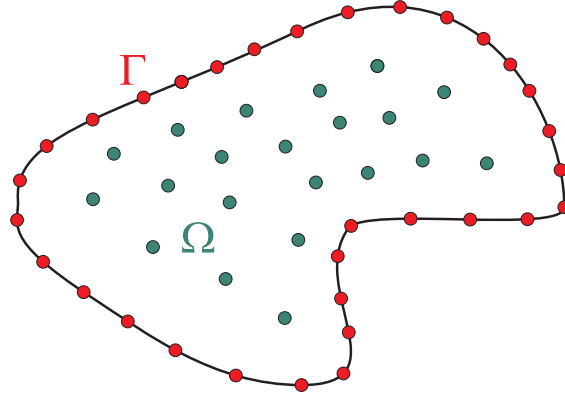
Figure 3.12: Typical node arrangement for the meshless methods. Red points represents boundary nodes and green points domain nodes.

In Kansa's method, the approximate solution for the problem (3.14)-(3.15) can be expressed as

$$u(\mathbf{p}) = \sum_{i=1}^{N} \alpha_i \psi(\mathbf{p} - \mathbf{p}_i); \ N = N_\Omega + N_\Gamma, \tag{3.16}$$

where α_i are expansion coefficients to be determined by collocation (i.e. interpolation), $\psi(\mathbf{p} - \mathbf{p}_i)$ is a radial basis function, N_Ω is the number of domain nodes and N_Γ the number of boundary nodes, respectively.

By substituting equation (3.16) into equations (3.14) and (3.15), we have

$$\sum_{j=1}^{N} (L\psi)(\mathbf{p}_i - \mathbf{p}_j)\alpha_j = f(\mathbf{p}_i), \ i = 1, 2, ..., N_\Omega \ \text{and} \tag{3.17}$$

$$\sum_{j=1}^{N} (B\psi)(\mathbf{p}_i - \mathbf{p}_j)\alpha_j = g(\mathbf{p}_i), \ i = N_\Omega + 1, N_\Omega + 2, ..., N. \tag{3.18}$$

Hence we have to solve the following $N \times N$ linear system of equations

$$\begin{bmatrix} \mathbf{\Psi}_{11} & \mathbf{\Psi}_{12} \\ \mathbf{\Psi}_{21} & \mathbf{\Psi}_{22} \end{bmatrix} \begin{bmatrix} \boldsymbol{\alpha}^{(f)} \\ \boldsymbol{\alpha}^{(g)} \end{bmatrix} = \begin{bmatrix} \mathbf{f} \\ \mathbf{g} \end{bmatrix} \tag{3.19}$$

for the unknowns $\boldsymbol{\alpha}^f = \left[\alpha_1, ..., \alpha_{N_\Omega}\right]^T$, $\boldsymbol{\alpha}^g = \left[\alpha_{N_\Omega+1}, ..., \alpha_N\right]^T$. Then the approximate solution can be obtained by equation (3.16) at any node in the domain Ω. The sub-matrices in equation (3.19) are

$$\mathbf{\Psi}_{11} \text{ with element } \left(L\psi\right)\left(\mathbf{p}_i - \mathbf{p}_j\right), \ i = 1, 2, ..., N_\Omega, j = 1, 2, ..., N_\Omega, \quad (3.20)$$

$$\mathbf{\Psi}_{12} \text{ with element } \left(L\psi\right)\left(\mathbf{p}_i - \mathbf{p}_j\right), \ i = 1, 2, ..., N_\Omega,$$

$$j = N_\Omega + 1, N_\Omega + 2, ..., N, \quad (3.21)$$

$$\mathbf{\Psi}_{21} \text{ with element } \left(B\psi\right)\left(\mathbf{p}_i - \mathbf{p}_j\right), \ i = N_\Omega + 1, N_\Omega + 2, ..., N,$$

$$j = 1, 2, ..., N_\Omega, \quad (3.22)$$

$$\mathbf{\Psi}_{22} \text{ with element } \left(B\psi\right)\left(\mathbf{p}_i - \mathbf{p}_j\right),$$

$$i = N_\Omega + 1, N_\Omega + 2, ..., N, \ j = N_\Omega + 1, N_\Omega + 2, ..., N, \quad (3.23)$$

and vectors

$$\mathbf{f} = \left[f\left(\mathbf{p}_1\right), f\left(\mathbf{p}_2\right), ..., f\left(\mathbf{p}_{N_\Omega}\right) \right]^T, \quad (3.24)$$

$$\mathbf{g} = \left[g\left(\mathbf{p}_{N_\Omega+1}\right), g\left(\mathbf{p}_{N_\Omega+2}\right), ..., g\left(\mathbf{p}_N\right) \right]^T. \quad (3.25)$$

We can easily see that the implementation of Kansa's method is quite simple and straightforward. These are the main reasons that this technique is getting popular and has been applied to many areas such as the solution of Navier-Stokes equations [Mai-Duy and Tran-Cong, 2001; Šarler, 2005] or porous media flow [Šarler *et al.*, 2004] and the solution of solid-liquid phase-change problems [Kovačević *et al.*, 2003]. In contrast to advantages of this method, collocation systems are often very badly conditioned, especially for larger problems (more than approximately thousand centers). The free parameter c has to be very carefully chosen in order to achieve convergence. The method has been further upgraded to symmetric collocation [Fasshauer, 1997; Power and Barraco, 2002], to modified collocation [Chen, 2002] and to indirect collocation [Mai-Duy and Tran-Cong, 2003]. In contrast to advantages over mesh generation, all the listed methods unfortunately fail to perform for large problems, because they produce fully populated matrices, sensitive to the choice of the free parameters in RBFs. One of the possibilities for mitigating this problem is to employ the domain decomposition [Mai-Duy and Tran-Cong, 2002]. However, the domain decomposition re-introduces some sort of meshing which is not attractive. The concept of local collocation in the context of RBF-based solution of Poisson equation has been introduced in [Lee *et al.*, 2003; Tolstykh and Shirobokov, 2003]. For interpolation of the function value in a certain node the authors use

only data in the (neighbor) nodes that fall into the influence domain of this node. The procedure results in a matrix that is of the same size as the matrix in the original Kansa method, however it is sparse. The circular influence domains have been used in [Lee *et al.*, 2003] where one-dimensional and two-dimensional Poisson equation has been solved by using MQ-RBFs and IMQ-RBFs with a detailed analysis of the influence of the free parameter on the results. In [Tolstykh and Shirobokov, 2003] the stencil-shaped domains have been used where a class of linear and non-linear elasticity problems have been solved with a fixed free parameter. The differential quadrature method, that calculates the derivatives of a function by a weighted linear sum of functional values at its neighbor nodes has been structured with the RBFs in [Shu *et al.*, 2003]. Despite the local properties, the matrix still has a similar form as in [Lee *et al.*, 2003; Tolstykh and Shirobokov, 2003].

4 Local radial basis function collocation method

Here, in this section, we are presenting one of the techniques to circumvent the ill-conditioning problem with MQ-RBFs when solving large PDE problems with Kansa method. The idea comes from diffuse approximate method (DAM) [Nayroles *et al.*, 1988; Sadat and Couturier, 2000; Vertnik *et al.*, 2004]. To approximate the solution of the PDE, this method needs only some neighbor nodes which are usually situated around the vicinity of the observed node.

4.1 Local collocation

We start with the representation of the function over a set of $_lN$ scattered nodes $_l\mathbf{p}_n$; $n = 1, 2, ..., {}_lN$ in the following way

$$u(\mathbf{p}) \approx \sum_{k=1}^{{}_lK} {}_l\psi_k(\mathbf{p}){}_l\alpha_k,\tag{4.1}$$

where $_l\psi_k$ stands for the shape functions, $_l\alpha_k$ for the expansion coefficients of the shape functions, and $_lK$ represents the number of the shape functions. The left lower index on entries of equation (4.1) represents the influence domain $_l\omega$ on which the coefficients $_l\alpha_k$ are determined. The sub domains $_l\omega$ can in general be contiguous (overlapping) or non-contiguous (non-overlapping). Each of the influence domains $_l\omega$ includes $_lN$ nodes of which $_lN_\Omega$ can in general be in the domain and $_lN_\Gamma$ on the boundary, i.e. $_lN = {}_lN_\Omega + {}_lN_\Gamma$. The influence domain of the node $_l\mathbf{p}$ is defined with the nodes having the nearest $_lN - 1$ distances to the node $_l\mathbf{p}$. The five node $_lN = 5$ and nine node $_lN = 9$ influence domains are used in this thesis. Typically chosen influence domains are shown in Figure 4.1. For the domain node, the influence domain contains the domain and boundary nodes. While for the boundary node, the influence domain usually contains this boundary node and rest the domain nodes.
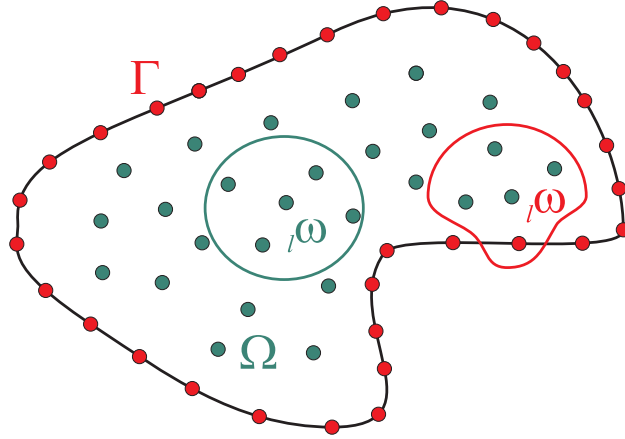
Figure 4.1: Node arrangement with typical influence domains. Green circle represents the internal influence domain and red circle the boundary influence domain.

The expansion coefficients can be calculated from the influence domain nodes in two distinct ways. The first way is collocation (interpolation) and the second way is approximation by the least squares method. Only the simpler collocation version for calculation of the coefficients is considered in this thesis. Let us assume the known function values $_l u_n$ in the nodes $_l \mathbf{p}_n$ of the influence domain $_l \omega$. The collocation implies

$$u\left(_l \mathbf{p}_n \right) = \sum_{k=1}^{_l N} {}_l \psi_k \left(_l \mathbf{p}_n \right) {}_l \alpha_k .$$

$$(4.2)$$

For the coefficients to be computable, the number of the shape functions has to match the number of the collocation nodes $_l K = {}_l N$, and the collocation matrix has to be non-singular. The system of equations (4.2) can be written in a matrix-vector notation

$$_l \underline{\Psi} \, _l \boldsymbol{\alpha} = {}_l \mathbf{u} \, ; \; _l \underline{\psi}_{kn} = {}_l \psi_k \left(_l \mathbf{p}_n \right), \; _l u_n = u\left(_l \mathbf{p}_n \right).$$

$$(4.3)$$

The coefficients $_l \boldsymbol{\alpha}$ can be computed by inverting the system (4.3)

$$_l \boldsymbol{\alpha} = {}_l \underline{\psi}^{-1} {}_l \mathbf{u} .$$

$$(4.4)$$

By taking into account the expressions for the calculation of the coefficients $_l \boldsymbol{\alpha}$, the collocation representation of function $u(\mathbf{p})$ on influence domain $_l \omega$ can be expressed as

$$u(\mathbf{p}) \approx \sum_{k=1}^{_lN} {}_l\Psi_k(\mathbf{p}) \sum_{n=1}^{_lN} {}_l\underline{\psi}_{kn}^{-1} {}_l u_n \;.$$ (4.5)

Let us introduce a two dimensional Cartesian coordinate system with base vectors $\mathbf{i}_\varsigma; \varsigma = x, y$ and coordinates $p_\varsigma; \varsigma = x, y$, i.e. $\mathbf{p} = \mathbf{i}_x p_x + \mathbf{i}_y p_y$. The first partial spatial derivatives of $u(\mathbf{p})$ on influence domain ${}_l\omega$ can be expressed as

$$\frac{\partial}{\partial p_\varsigma} u(\mathbf{p}) \approx \sum_{k=1}^{_lN} \frac{\partial}{\partial p_\varsigma} {}_l\Psi_k(\mathbf{p}) \sum_{n=1}^{_lN} {}_l\underline{\psi}_{kn}^{-1} {}_l u_n \;;\; \varsigma = x, y \;.$$ (4.6)

The second partial spatial derivatives of $u(\mathbf{p})$ on influence domain ${}_l\omega$ can be expressed as

$$\frac{\partial^2}{\partial p_\varsigma p_\zeta} u(\mathbf{p}) \approx \sum_{k=1}^{_lN} \frac{\partial^2}{\partial p_\varsigma p_\zeta} {}_l\Psi_k(\mathbf{p}) \sum_{n=1}^{_lN} {}_l\underline{\psi}_{kn}^{-1} {}_l u_n \;;\; \varsigma, \zeta = x, y \;.$$ (4.7)

The MQ-RBF is used for the shape functions

$${}_l\Psi_k(\mathbf{p}) = \left[{}_lr_k^2(\mathbf{p}) + c^2 \right]^{1/2} \;;\; {}_lr_k^2 = (\mathbf{p} - {}_l\mathbf{p}_k) \cdot (\mathbf{p} - {}_l\mathbf{p}_k) \;,$$ (4.8)

where c represents the free parameter. The explicit values of the involved first and second derivatives of $\psi_k(\mathbf{p})$ are

$$\frac{\partial}{\partial p_\varsigma} {}_l\Psi_k(\mathbf{p}) = \frac{p_\varsigma - {}_lp_{k\varsigma}}{\left({}_lr_k^2 + c^2 \right)^{1/2}} \;;\; \varsigma = x, y \;,$$ (4.9)

$$\frac{\partial^2}{\partial p_\varsigma^2} {}_l\Psi_k(\mathbf{p}) = \frac{\left(p_y - {}_lp_{k\varsigma} \right)^2 + c^2}{\left({}_lr_k^2 + c^2 \right)^{3/2}} \;;\; \varsigma = x, y \;\text{ and}$$ (4.10)

$$\frac{\partial^2}{\partial p_\varsigma p_\zeta} {}_l\Psi_k(\mathbf{p}) = \frac{\partial^2}{\partial p_\xi p_\zeta} {}_l\Psi_k(\mathbf{p}) = -\frac{\left(p_\varsigma - {}_lp_{k\varsigma} \right)\left(p_\zeta - {}_lp_{k\zeta} \right)}{\left({}_lr_k^2 + c^2 \right)^{3/2}} \;;$$

$$\varsigma, \zeta = x, y \;.$$ (4.11)

4.2 Optimal free parameter

Selecting the optimal free parameter is one of the important task in using the RBF. The choice of the optimum value of this parameter is still an unresolved problem, and the optimum value is usually at the present state-of-the-art found

using numerical experiments. Some authors [Mai-Dui and Tranh-Cong, 2001] claim that the free parameter is related to the typical grid distance. Other researchers [Zhang *et al*., 2000] did not find any relation, and claim simply that the optimum free parameter is problem dependent. Very recently [Wang and Liu, 2002] analyzed the extended MQ, i.e.

$$_l\psi_k(\mathbf{p}) = \left[_lr_k^2(\mathbf{p}) + c^2 \right]^{\beta},$$
(4.12)

were the exponent β is free parameter as well. The authors concluded that by proper fixing of both parameters the solution becomes independent on the node density, node distribution and problem. [Lee *et al*., 2003] found that the results are less sensitive to the choice of the free parameter in the local collocation method as in the global ones. The optimal value depends on the number of nodes, position of nodes and the function value of the nodes in the influence domain. The number of nodes is usually fixed for all influence domains for an application, so the influence of the number of nodes is not considered. Since the nodes in the influence domain are usually scattered, the scale of the influence domain region for each reference node could be different, and the optimal free parameter for accurate numerical results may also be different. To assign different values of the free parameter for each node is very difficult. This difficulty can be handled at least in the following two ways:

q) By using the dimensionless free parameter c
The MQ radial basis function (equation (4.8)) is changed into the following form

$$_l\psi_k(\mathbf{p}) = \left[_lr_k^2(\mathbf{p}) + \left(c\,_lr_0\right)^2 \right]^{1/2},$$
(4.13)

where $_lr_0^2$ represents the scaling parameter. The scaling parameter $_lr_0$ is set to the maximum nodal distance in the influence domain

$$_lr_0 = \max \, _lr_m\left(_l\mathbf{p}_n\right); \; m,n = 1,2,...,_lN .$$
(4.14)

The derivatives are calculated by the equations (4.9)-(4.11), where the free parameter c is replaced by the dimensionless free parameter $c\,_lr_0$.
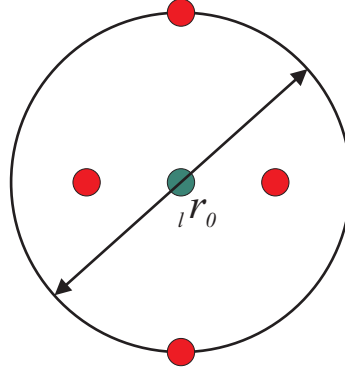
Figure 4.2: Local influence domain with the maximum nodal distance $_l r_0$. Green node – reference node, red node – neighbor nodes.

b) By using the normalized influence domain region

The normalization of the influence domain is performed by scaling the distance in x and y direction. In equation (4.8) the scaled radial distance $_l r_k$ between two nodes is calculated as

$$_l r_k^2 = \left(\frac{p_x - {_l p_{kx}}}{_l p_{x_{max}}} \right)^2 + \left(\frac{p_y - {_l p_{ky}}}{_l p_{y_{max}}} \right)^2 , \tag{4.15}$$

where the scaling parameters $_l p_{x_{max}}$ and $_l p_{y_{max}}$ are set to the maximum nodal distance in both directions of the influence domain

$$_l p_{\varsigma_{max}} = \max \left({_l p_{\varsigma m}} - {_l p_{\varsigma n}} \right); \ m,n = 1,2,...,{_l N} ; \ \varsigma = x,y . \tag{4.16}$$

The derivatives are calculated by the following equations

$$\frac{\partial}{\partial p_\varsigma} {_l \Psi_k}(\mathbf{p}) = \frac{1}{_l p_{\varsigma_{max}}} \frac{p_\varsigma - {_l p_{k\varsigma}}}{\left({_l r_k^2} + c^2 \right)^{1/2}} ; \ \varsigma = x,y , \tag{4.17}$$

$$\frac{\partial^2}{\partial p_\varsigma^2} {_l \Psi_k}(\mathbf{p}) = \frac{1}{_l p_{\varsigma_{max}}^2} \frac{\left(p_\varsigma - {_l p_{k\varsigma}} \right)^2 + c^2 {_l r_0^2}}{\left({_l r_k^2} + c^2 \right)^{3/2}} ; \ \varsigma = x,y \ \text{and} \tag{4.18}$$

$$\frac{\partial^2}{\partial p_\varsigma p_\zeta} {_l \Psi_k}(\mathbf{p}) = \frac{\partial^2}{\partial p_\zeta p_\varsigma} {_l \Psi_k}(\mathbf{p}) =$$

$$= -\frac{1}{_l p_{\varsigma_{max}} \cdot {_l p_{\zeta_{max}}}} \frac{\left(p_\varsigma - {_l p_{k\varsigma}} \right) \left(p_\zeta - {_l p_{k\zeta}} \right)}{\left({_l r_k^2} + c^2 \right)^{3/2}} ; \ \varsigma,\zeta = x,y \tag{4.19}$$
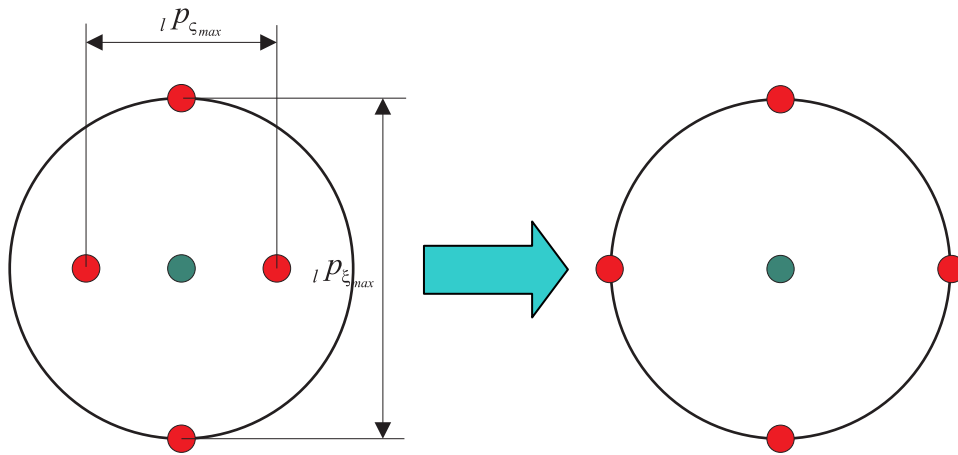
Figure 4.3: Local influence domain scaled with the maximum nodal distance in ς and ξ direction. Left picture represents influence domain before scaling and right picture after scaling.

5 Solution procedures

In this chapter the solution procedures for the numerical solution of various heat transfer problems are presented. First, the solution procedure of the general transport equation is given. The derived procedure stands as a base for solution of all other equations. It is further specified for the diffusive equation, the convective-diffusive equation with phase change, and the convective-diffusive equation with phase change and a material moving boundary. For better understanding, the exact solution procedure of each equation is provided. The time discretization is also described.

5.1 Time discretization

The transient problems have numerous important applications in science and engineering. Almost all industrial process experience transients during various stages of the operation. For example, the start-up phase of the direct chill casting process of aluminum alloys, where the billet moves from mould to secondary cooling zone and is therefore exposed to a different boundary conditions which result in transient variations of boundary solid-liquid interface position and temperature field.

In time-dependent problems, transport variable $\phi(\mathbf{p})$ besides the space, also depends on time, i.e. $\phi(\mathbf{p},t)$, which is additional variable to be discretized. The time discretization defines the direction for information transfer, namely from the past into the future. The common types of the time discretization procedures are explicit, implicit and Crank-Nicolson.

Explicit scheme involves only one unknown variable for the future time, which can be directly calculated from known variables from current time step.

$$\frac{\partial \phi(\mathbf{p},t)}{\partial t} \approx \frac{\phi(\mathbf{p},t_0+\Delta t) - \phi(\mathbf{p},t_0)}{\Delta t} = \mathrm{F}\big(\phi(\mathbf{p},t_0)\big) + \mathrm{O}(\Delta t). \qquad (5.1)$$

An explicit time discretization form is only conditionally stable. The stability criteria for diffusion equation is defined by the Fourier number

$$\text{Fo} = \frac{k \cdot \Delta t}{c_p \cdot \rho \cdot (\Delta p_x)^2} . \tag{5.2}$$

The stability analysis leads to the following requirement

$$\text{Fo} \le \frac{1}{2} \tag{5.3}$$

and restricted time step

$$\Delta t \le \frac{c_p \cdot \rho \cdot (\Delta p_x)^2}{2 \cdot k} . \tag{5.4}$$

The stability criteria for convection equation is defined by the Courant number

$$C_r = \frac{|\bar{v}| \Delta t}{\Delta p_x} \tag{5.5}$$

and here the stability analysis leads to the following requirement

$$C_r \le 1 \tag{5.6}$$

and restricted time step

$$\Delta t \le \frac{\Delta p_x}{|\bar{v}|} . \tag{5.7}$$

The convection-diffusion equation contains both physical phenomena, diffusion and convection. In order to get stable results, the stability criteria of both phenomena must be satisfied.
When implicit procedure is used, equivalent of equation (5.1) is

$$\frac{\partial \phi(\mathbf{p}, t)}{\partial t} \approx \frac{\phi(\mathbf{p}, t_0 + \Delta t) - \phi(\mathbf{p}, t_0)}{\Delta t} = \text{F}\big(\phi(\mathbf{p}, t_0 + \Delta t)\big) + \text{O}(\Delta t) . \tag{5.8}$$

To get the second order accuracy and unconditionally stable solution, the Crank-Nicolson procedure can be used. Here, the solution at next time depends on known values from previous time step and unknown values for next time step, i.e.

$$\frac{\partial \phi(\mathbf{p},t)}{\partial t} \approx \frac{\phi(\mathbf{p},t_0+\Delta t)-\phi(\mathbf{p},t_0)}{\Delta t} = 0.5\text{F}\big(\phi(\mathbf{p},t_0+\Delta t)\big)+$$
$$0.5\text{F}\big(\phi(\mathbf{p},t_0)\big)+\text{O}\big(\Delta t^2\big) \tag{5.9}$$

In all numerical examples, only the simple explicit time discretization is used to derive the solution procedure of various conservative equations. The reasons for using explicit time discretizaton are:

- For domain nodes the matrix of the system of equations (4.3) is constant. For this purpose the LU (lower/upper) factorization of the matrix is performed for domain nodes before the start-up of calculation. The system of linear equations (4.3) is then solved with pre-calculated coefficient matrix of the LU factorization. This procedure strongly increases the calculation speed of the system (4.3).
- The matrix are small, only from 5×5 to 9×9 dimension (in this work), depending on the number of influence domain nodes.
- To deal with nonlinear thermo-physical properties and nonlinear boundary conditions of the convective-diffusive phase-change problems, the time step is often restricted to small value, similar that would be used in implicit scheme. The stability issue is then of less importance.

5.2 Treatment of the general transport equation

Consider the general transport equation, defined on a connected fixed domain Ω with boundary Γ, standing for a reasonably broad spectra of mass, energy, momentum, and species transfer problem

$$\frac{\partial}{\partial t}\big(\rho\text{C}(\phi)\big)+\nabla\cdot\big(\rho\mathbf{v}\text{C}(\phi)\big)=\nabla\cdot\big(\underline{\mathbf{D}}\nabla\phi\big)+S \tag{5.10}$$

with ρ, ϕ, t, $\mathbf{v}$, $\underline{\mathbf{D}}$, and S standing for density, transport variable, time, velocity, diffusion tensor

$$\underline{\mathbf{D}}=\begin{bmatrix} D_{11} & D_{12} & D_{13} \\ D_{21} & D_{22} & D_{23} \\ D_{31} & D_{32} & D_{33} \end{bmatrix} \tag{5.11}$$

and source, respectively. The scalar function C stands for possible more involved constitutive relations between the conserved $\text{C}(\phi)$ and diffused ϕ quantities. We seek the solution of the governing equation for the transport

variable at the final time $t_0 + \Delta t$, where t_0 represents initial time and Δt the positive time increment. The solution is constructed by the initial and boundary conditions that follow. The initial value of the transport variable $\phi(\mathbf{p},t)$ at a node with position vector $\mathbf{p}$ and time t_0 is defined through the known function ϕ_0

$$\phi(\mathbf{p},t) = \phi_0(\mathbf{p}) \, ; \, \mathbf{p} \in \Omega + \Gamma \, . \tag{5.12}$$

The boundary Γ is divided into not necessarily connected parts $\Gamma = \Gamma^D \cup \Gamma^N \cup \Gamma^R$ with Dirichlet, Neumann and Robin type boundary conditions, respectively. At the boundary node $\mathbf{p}$ with normal $\mathbf{n}_\Gamma$ and time $t_0 \leq t \leq t_0 + \Delta t$, these boundary conditions are defined through known functions ϕ_Γ^D, ϕ_Γ^N, ϕ_Γ^R, $\phi_{\Gamma ref}^R$

$$\phi = \phi_\Gamma^D \, ; \, \mathbf{p} \in \Gamma^D \, , \tag{5.13}$$

$$\frac{\partial}{\partial n_\Gamma} \phi = \phi_\Gamma^N \, ; \, \mathbf{p} \in \Gamma^N \text{ and} \tag{5.14}$$

$$\frac{\partial}{\partial n_\Gamma} \phi = \phi_\Gamma^R \left(\phi - \phi_{\Gamma ref}^R \right) \, ; \, \mathbf{p} \in \Gamma^R \, . \tag{5.15}$$

The numerical discretization of equation (5.10), using explicit (Euler) time discretization has the form

$$\frac{\partial \left(\rho C(\phi) \right)}{\partial t} \approx \frac{\rho_0 C(\phi) - \rho_0 C(\phi_0)}{\Delta t} = -\nabla \cdot \left(\mathbf{v}_0 \rho_0 C(\phi_0) \right) + \nabla \cdot \left(\underline{\mathbf{D}} \nabla \phi_0 \right) . \tag{5.16}$$

From equation (5.16) the unknown function value $C(\phi)_l$ in domain node $\mathbf{p}_l$ can be calculated as

$$C(\phi)_l = C(\phi)_{0l} + \frac{\Delta t}{\rho_0} \left(-\nabla \cdot \left(\mathbf{v}_0 \rho_0 C(\phi)_{0l} \right) + \nabla \underline{\mathbf{D}}_{0l} \cdot \nabla \phi_{0l} + \underline{\mathbf{D}}_{0l} \cdot \nabla^2 \phi_{0l} \right) . \tag{5.17}$$

In continuation, the assumption of the diffusion tensor $\underline{\mathbf{D}}$ is made

$$\underline{\mathbf{D}} = D \begin{bmatrix} 1 & 0 & 0 \\ 0 & 1 & 0 \\ 0 & 0 & 1 \end{bmatrix} . \tag{5.18}$$

The explicit calculation of expression (5.17) in 2D Cartesian coordinates (p_x, p_y) is

$$\mathrm{C}(\phi)_{l} = \mathrm{C}(\phi)_{0l} + \frac{\Delta t}{\rho_0}\left(\sum_{k=1}^{{}_l N} \frac{\partial}{\partial p_x}\,{}_l\Psi_k(\mathbf{p}_l)\sum_{n=1}^{{}_l N}\,{}_l\underline{\psi}_{kn}^{-1}{}_l\left(v_{0x}\rho_0\mathrm{C}(\phi)_0\right)_n + \right.$$

$$\sum_{k=1}^{{}_l N} \frac{\partial}{\partial p_y}\,{}_l\Psi_k(\mathbf{p}_l)\sum_{n=1}^{{}_l N}\,{}_l\underline{\psi}_{kn}^{-1}{}_l\left(v_{0y}\rho_0\mathrm{C}(\phi)_0\right)_n +$$

$$\left(\sum_{k=1}^{{}_l N} \frac{\partial}{\partial p_x}\,{}_l\Psi_k(\mathbf{p}_l)\sum_{n=1}^{{}_l N}\,{}_l\underline{\psi}_{kn\,l}^{-1}D_{0n}\right)\cdot\left(\sum_{k=1}^{{}_l N} \frac{\partial}{\partial p_x}\,{}_l\Psi_k(\mathbf{p}_l)\sum_{n=1}^{{}_l N}\,{}_l\underline{\psi}_{kn\,l}^{-1}\phi_{0n}\right) +$$

$$\left(\sum_{k=1}^{{}_l N} \frac{\partial}{\partial p_y}\,{}_l\Psi_k(\mathbf{p}_l)\sum_{n=1}^{{}_l N}\,{}_l\underline{\psi}_{kn\,l}^{-1}D_{0n}\right)\cdot\left(\sum_{k=1}^{{}_l N} \frac{\partial}{\partial p_y}\,{}_l\Psi_k(\mathbf{p}_l)\sum_{n=1}^{{}_l N}\,{}_l\underline{\psi}_{kn\,l}^{-1}\phi_{0n}\right) +$$

$$\sum_{n=1}^{{}_l N} \frac{\partial^2}{\partial p_x^2}\,{}_l\Psi_k(\mathbf{p}_l)\sum_{n=1}^{{}_l N}\,{}_l\underline{\psi}_{kn\,l}^{-1}\phi_{0n} + \sum_{n=1}^{{}_l N} \frac{\partial^2}{\partial p_y^2}\,{}_l\Psi_k(\mathbf{p}_l)\sum_{n=1}^{{}_l N}\,{}_l\underline{\psi}_{kn\,l}^{-1}\phi_{0n}\right)$$

$$(5.19)$$

and in axisymmetry (p_r, p_z) is

$$\mathrm{C}(\phi)_{l} = \mathrm{C}(\phi)_{0l} + \frac{\Delta t}{\rho_0}\left(\sum_{k=1}^{{}_l N} \frac{\partial}{\partial p_r}\,{}_l\Psi_k(\mathbf{p}_l)\sum_{n=1}^{{}_l N}\,{}_l\underline{\psi}_{kn}^{-1}{}_l\left(v_{0r}\rho_0\mathrm{C}(\phi)_0\right)_n + \right.$$

$$\sum_{k=1}^{{}_l N} \frac{\partial}{\partial p_z}\,{}_l\Psi_k(\mathbf{p}_l)\sum_{n=1}^{{}_l N}\,{}_l\underline{\psi}_{kn}^{-1}{}_l\left(v_{0z}\rho_0\mathrm{C}(\phi)_0\right)_n +$$

$$\left(\sum_{k=1}^{{}_l N} \frac{\partial}{\partial p_r}\,{}_l\Psi_k(\mathbf{p}_l)\sum_{n=1}^{{}_l N}\,{}_l\underline{\psi}_{kn\,l}^{-1}D_{0n}\right)\cdot\left(\sum_{k=1}^{{}_l N} \frac{\partial}{\partial p_r}\,{}_l\Psi_k(\mathbf{p}_l)\sum_{n=1}^{{}_l N}\,{}_l\underline{\psi}_{kn\,l}^{-1}\phi_{0n}\right) +$$

$$\left(\sum_{k=1}^{{}_l N} \frac{\partial}{\partial p_z}\,{}_l\Psi_k(\mathbf{p}_l)\sum_{n=1}^{{}_l N}\,{}_l\underline{\psi}_{kn\,l}^{-1}D_{0n}\right)\cdot\left(\sum_{k=1}^{{}_l N} \frac{\partial}{\partial p_z}\,{}_l\Psi_k(\mathbf{p}_l)\sum_{n=1}^{{}_l N}\,{}_l\underline{\psi}_{kn\,l}^{-1}\phi_{0n}\right) +$$

$$\left(\frac{1}{p_r}\sum_{n=1}^{{}_l N} \frac{\partial}{\partial p_r}\,{}_l\Psi_k(\mathbf{p}_l)\sum_{n=1}^{{}_l N}\,{}_l\underline{\psi}_{kn\,l}^{-1}\phi_{0n} + \sum_{n=1}^{{}_l N} \frac{\partial^2}{\partial p_r^2}\,{}_l\Psi_k(\mathbf{p}_l)\sum_{n=1}^{{}_l N}\,{}_l\underline{\psi}_{kn\,l}^{-1}\phi_{0n} + \right.$$

$$\left.\left.\sum_{n=1}^{{}_l N} \frac{\partial^2}{\partial p_z^2}\,{}_l\Psi_k(\mathbf{p}_l)\sum_{n=1}^{{}_l N}\,{}_l\underline{\psi}_{kn\,l}^{-1}\phi_{0n}\right)\right)$$

$$(5.20)$$

where in both equations the formulas (4.6) and (4.7) have been employed.

The complete solution procedure follows the below defined steps 1-5.

Step 1
First, the initial conditions are set in the domain and boundary nodes and the required derivatives are calculated from the known nodal values.

Step 2
The equation (5.19) or (5.20) is used to calculate the new values of the variable $_l C(\phi)_n$ at time $t_0 + \Delta t$ in the domain nodes.

Step 3
The transport variable $_l \phi_n$ is calculated from the constitutive relation $C(\phi)$ in the domain nodes.

$$_l \phi_n = C(\phi). \tag{5.21}$$

Step 4
The unknown transport variable $_l \phi_n$ at time $t_0 + \Delta t$ in the Dirichlet, Neumann, and Robin boundary nodes is calculated. The coefficients $_l \alpha$ have to be determined from the new values in the domain, calculated in step 3, and from the information on the boundary conditions. Let us introduce domain, Dirichlet, Neumann, and Robin boundary indicators for this purpose. These indicators are defined as

$$\Upsilon_{\Omega n} = \begin{cases} 1; \mathbf{p}_n \in \Omega \\ 0; \mathbf{p}_n \notin \Omega \end{cases}, \quad \Upsilon_{\Gamma n}^{D} = \begin{cases} 1; \mathbf{p}_n \in \Gamma^{D} \\ 0; \mathbf{p}_n \notin \Gamma^{D} \end{cases}, \quad \Upsilon_{\Gamma n}^{N} = \begin{cases} 1; \mathbf{p}_n \in \Gamma^{N} \\ 0; \mathbf{p}_n \notin \Gamma^{N} \end{cases} \text{ and}$$

$$\Upsilon_{\Gamma n}^{R} = \begin{cases} 1; \mathbf{p}_n \in \Gamma^{R} \\ 0; \mathbf{p}_n \notin \Gamma^{R} \end{cases}. \tag{5.22}$$

The coefficients $_l \alpha$ are calculated from the system of linear equations

$$\sum_{k=1}^{_l N} {}_l \Upsilon_{\Omega n} {}_l \psi_k \left({}_l \mathbf{p}_n \right) {}_l \alpha_k + \sum_{k=1}^{_l N} {}_l \Upsilon_{\Gamma n}^{D} {}_l \psi_k \left({}_l \mathbf{p}_n \right) {}_l \alpha_k$$

$$+ \sum_{k=1}^{_l N} {}_l \Upsilon_{\Gamma n}^{N} \frac{\partial}{\partial n_\Gamma} {}_l \psi_k \left({}_l \mathbf{p}_n \right) {}_l \alpha_k + \sum_{k=1}^{_l N} {}_l \Upsilon_{\Gamma n}^{R} \frac{\partial}{\partial n_\Gamma} {}_l \psi_k \left({}_l \mathbf{p}_n \right) {}_l \alpha_k =$$

$$= {}_l \Upsilon_{\Omega n} {}_l \phi_n + {}_l \Upsilon_{\Gamma n}^{D} {}_l \phi_n^{D} + {}_l \Upsilon_{\Gamma n}^{N} {}_l \phi_n^{N} + {}_l \Upsilon_{\Gamma n}^{R} {}_l \phi_{\Gamma n}^{R} \left(\sum_{k=1}^{_l N} {}_l \psi_k \left({}_l \mathbf{p}_n \right) {}_l \alpha_k - {}_l \phi_{\Gamma ref\, n}^{R} \right).$$

$$\tag{5.23}$$

The system (5.23) can be written in a compact form

$$_l \underline{\boldsymbol{\Psi}}_l \boldsymbol{\alpha} = {}_l \mathbf{b} \qquad (5.24)$$

with the following system matrix entries

$$
\begin{aligned}
_l \underline{\boldsymbol{\Psi}}_{nk} = {}_l \Upsilon_{\Omega n} {}_l \psi_k \left({}_l \mathbf{p}_n \right) + {}_l \Upsilon_{\Gamma n}^D {}_l \psi_k \left({}_l \mathbf{p}_n \right) \\
+ {}_l \Upsilon_{\Gamma n}^N \frac{\partial}{\partial n_\Gamma} {}_l \psi_k \left({}_l \mathbf{p}_n \right) + {}_l \Upsilon_{\Gamma n}^R \left[\frac{\partial}{\partial n_\Gamma} {}_l \psi_k \left({}_l \mathbf{p}_n \right) - {}_l \phi_{\Gamma n}^R \sum_{k=1}^{{}_l N} {}_l \psi_k \left({}_l \mathbf{p}_n \right) \right]
\end{aligned}
\qquad (5.25)
$$

and with the following explicit form of the augmented right hand side vector

$$
_l \mathbf{b}_n = {}_l \Upsilon_{\Omega n} \phi_n + {}_l \Upsilon_{\Gamma n}^D \phi_{\Gamma n}^D + {}_l \Upsilon_{\Gamma n}^N \phi_{\Gamma n}^N - {}_l \Upsilon_{\Gamma n}^R {}_l \phi_{\Gamma n}^R {}_l \phi_{\Gamma ref\, n}^R . \qquad (5.26)
$$

Step 5
The unknown boundary values are set from equation (4.5).

When searching the steady-state solution the following criterion

$$\max |\phi_n - \phi_{0n}| \le \phi_{ste} \qquad (5.27)$$

must be met. The parameter ϕ_{ste} is defined as the steady-state convergence margin. In case the steady-state criterion is fulfilled or the time of calculation exceeds the foreseen time of interest, the calculation is stopped.

5.3 Treatment of the heat conduction equation

The heat conduction equation can be derived from the general transport equation (5.10), where the transport variable, scalar function, velocity and diffusion matrix are

$$\phi = T , \qquad (5.28)$$

$$C(\phi) = c_p \cdot T , \qquad (5.29)$$

$$\mathbf{v} = 0 \text{ and} \qquad (5.30)$$

$$\underline{\mathbf{D}} = k \begin{bmatrix} 1 & 0 & 0 \\ 0 & 1 & 0 \\ 0 & 0 & 1 \end{bmatrix} , \qquad (5.31)$$

respectively. With the above assumptions we get the following heat conduction equation

$$\rho c \frac{\partial}{\partial t} T = \nabla \cdot \left(k \nabla T \right) \tag{5.32}$$

with ρ, c_p, k, T and t standing for density, specific heat, thermal conductivity, temperature, and time. The material properties ρ, c_p and k may depend on the position and temperature, i.e. the problem might be inhomogeneous and nonlinear. The solution of the governing equation for the temperature at the final time $t_0 + \Delta t$ is sought, where t_0 represents the initial time and Δt the positive time increment. The solution is constructed by the initial and boundary conditions that are defined in Section 5.2, equations (5.12)-(5.15).

The diffusion equation (5.32) can be transformed into the following expression by taking into account the explicit time discretization

$$\rho c_p \frac{\partial T}{\partial t} \approx \frac{\rho_0 c_{p0} T - \rho_0 c_{p0} T_0}{\Delta t} = \nabla \cdot \left(k_0 \nabla T_0 \right). \tag{5.33}$$

The unknown function value T_l in domain node $\mathbf{p}_l$ can be calculated as

$$T_l = T_{0l} + \frac{\Delta t}{\rho_{0l} c_{p0l}} \nabla \cdot \left(k_{0l} \nabla T_{0l} \right) = T_{0l} + \frac{\Delta t}{\rho_{0l} c_{p0l}} \left[\nabla k_{0l} \cdot \nabla T_{0l} + k_{0l} \cdot \nabla^2 T_{0l} \right]. \tag{5.34}$$

The explicit calculation of upper expression in 2D Cartesian coordinates (p_x, p_y) is

$$
\begin{aligned}
T_l = T_{0l} &+ \frac{\Delta t}{\rho_{0l} c_{p0l}} \left(\sum_{k=1}^{lN} \frac{\partial}{\partial p_x} {}_l\Psi_k(\mathbf{p}_l) \sum_{n=1}^{lN} {}_l\underline{\psi}_{kn}^{-1} {}_l k_n \right) \left(\sum_{k=1}^{lN} \frac{\partial}{\partial p_x} {}_l\Psi_k(\mathbf{p}_l) \sum_{n=1}^{lN} {}_l\underline{\psi}_{kn}^{-1} {}_l T_{0n} \right) \\
&+ \frac{\Delta t}{\rho_{0l} c_{p0l}} \left(\sum_{k=1}^{lN} \frac{\partial}{\partial p_y} {}_l\Psi_k(\mathbf{p}_l) \sum_{n=1}^{lN} {}_l\underline{\psi}_{kn}^{-1} {}_l k_n \right) \left(\sum_{k=1}^{lN} \frac{\partial}{\partial p_y} {}_l\Psi_k(\mathbf{p}_l) \sum_{n=1}^{lN} {}_l\underline{\psi}_{kn}^{-1} {}_l T_{0n} \right) \\
&+ \frac{\Delta t k_{0l}}{\rho_{0l} c_{p0l}} \left(\sum_{n=1}^{lN} \frac{\partial^2}{\partial p_x^2} {}_l\Psi_k(\mathbf{p}_l) \sum_{n=1}^{lN} {}_l\underline{\psi}_{kn}^{-1} {}_l T_n + \sum_{n=1}^{lN} \frac{\partial^2}{\partial p_y^2} {}_l\Psi_k(\mathbf{p}_l) \sum_{n=1}^{lN} {}_l\underline{\psi}_{kn}^{-1} {}_l T_n \right)
\end{aligned}
$$

$$\tag{5.35}$$

and in axisymmetry (p_r, p_z) is

$$
\begin{aligned}
T_l = T_{0l} &+ \frac{\Delta t}{\rho_{0l} c_{p0l}} \left[\sum_{k=1}^{{}_l N} \frac{\partial}{\partial p_r}\, {}_l\Psi_k(\mathbf{p}_l) \sum_{n=1}^{{}_l N} {}_l\underline{\psi}_{kn}^{-1}\, {}_l k_n \right] \cdot \left[\sum_{k=1}^{{}_l N} \frac{\partial}{\partial p_r}\, {}_l\Psi_k(\mathbf{p}_l) \sum_{n=1}^{{}_l N} {}_l\underline{\psi}_{kn}^{-1}\, T_{0n} \right] \\[2mm]
&+ \frac{\Delta t}{\rho_{0l} c_{p0l}} \left[\sum_{k=1}^{{}_l N} \frac{\partial}{\partial p_z}\, {}_l\Psi_k(\mathbf{p}_l) \sum_{n=1}^{{}_l N} {}_l\underline{\psi}_{kn}^{-1}\, {}_l k_n \right] \cdot \left[\sum_{k=1}^{{}_l N} \frac{\partial}{\partial p_z}\, {}_l\Psi_k(\mathbf{p}_l) \sum_{n=1}^{{}_l N} {}_l\underline{\psi}_{kn}^{-1}\, T_{0n} \right] \\[2mm]
&+ \frac{\Delta t\, k_{0l}}{\rho_{0l} c_{p0l}} \left[\frac{1}{p_r} \sum_{n=1}^{{}_l N} \frac{\partial}{\partial p_r}\, {}_l\Psi_k(\mathbf{p}_l) \sum_{n=1}^{{}_l N} {}_l\underline{\psi}_{kn}^{-1}\, {}_l T_n + \sum_{n=1}^{{}_l N} \frac{\partial^2}{\partial p_r^2}\, {}_l\Psi_k(\mathbf{p}_l) \sum_{n=1}^{{}_l N} {}_l\underline{\psi}_{kn}^{-1}\, {}_l T_n \right. \\[2mm]
&\left. + \sum_{n=1}^{{}_l N} \frac{\partial^2}{\partial p_z^2}\, {}_l\Psi_k(\mathbf{p}_l) \sum_{n=1}^{{}_l N} {}_l\underline{\psi}_{kn}^{-1}\, {}_l T_n \right]
\end{aligned}
$$

,

$$(5.36)$$

where the formulas (4.6) and (4.7) have been employed.

The complete solution procedure follows the below defined steps 1-4.

Step 1
First, the initial conditions are set in the domain and boundary nodes and the required derivatives are calculated from the known nodal values.

Step 2
The equation (5.35) or (5.36) is used to calculate the new values of the variable ${}_l T_n$ at time $t_0 + \Delta t$ in the domain nodes.

Step 3
The unknown function variable ${}_l T_n$ at time $t_0 + \Delta t$ in the Dirichlet, Neumann, and Robin boundary nodes is calculated. The calculation is performed in the same way as in Section 5.2, equations (5.22)-(5.26).

Step 4
The unknown boundary values are set from equation (4.5).

The steady-state is achieved when the criterion

$$
\max \left| T_n - T_{0n} \right| \le T_{\text{ste}} \tag{5.37}
$$

is satisfied in all computational nodes $\mathbf{p}_n; n = 1, 2, ..., N$. The parameter T_{ste} is defined as the steady-state convergence margin. In case the steady-state criterion

is achieved or the time of calculation exceeds the foreseen time of interest, the calculation is stopped.

5.4 Treatment of the convective-diffusive equation with phase change

The convective-diffusive equation can be also derived from the general transport equation (5.10), where the transport variable, scalar function and diffusion matrix are

$$\phi = T \,, \tag{5.38}$$

$$C(\phi) = h \ \text{and} \tag{5.39}$$

$$\underline{\mathbf{D}} = k \begin{bmatrix} 1 & 0 & 0 \\ 0 & 1 & 0 \\ 0 & 0 & 1 \end{bmatrix}, \tag{5.40}$$

respectively. With the above assumptions we get the following mixture continuum formulation (equation (2.15)) of the enthalpy conservation

$$\frac{\partial}{\partial t}(\rho h) + \nabla \cdot (\rho \mathbf{v} h) = \nabla \cdot (k \nabla T) \tag{5.41}$$

with the temperature dependent mixture density ρ, enthalpy h, velocity $\mathbf{v}$ and thermal conductivity k.

We seek for mixture temperature at time $t_0 + \Delta t$ by assuming known initial temperature, velocity field, and boundary conditions at time t_0. The solution is constructed by the initial and boundary conditions that are defined in Section 5.2, equations (5.12)-(5.15).

The numerical discretization of equation (5.41), using explicit (Euler) time discretization and constant density has the form

$$\frac{\partial(\rho h)}{\partial t} \approx \frac{\rho_0 h - \rho_0 h_0}{\Delta t} = -\nabla \cdot (\mathbf{v}_0 \rho_0 h_0) + \nabla \cdot (k_0 \nabla T_0). \tag{5.42}$$

From equation (5.42) the unknown function value h_l in domain node $\mathbf{p}_l$ can be calculated as

$$h_l = h_{0l} + \frac{\Delta t}{\rho_0 c_0} \left(-\nabla \cdot (\mathbf{v}_0 \rho_0 h_{0l}) + \nabla k_{0l} \cdot \nabla T_{0l} + k_{0l} \cdot \nabla^2 T_{0l} \right). \tag{5.43}$$

The explicit calculation of expression (5.43) in 2D Cartesian coordinates (p_x, p_y) is

$$
\begin{aligned}
h_l = h_{0l} + \frac{\Delta t}{\rho_0} &\left(\sum_{k=1}^{lN} \frac{\partial}{\partial p_x}\,{}_l\Psi_k(\mathbf{p}_l) \sum_{n=1}^{lN} {}_l\underline{\psi}_{kn}^{-1}{}_l (v_{0x}\rho_0 h_0)_n + \sum_{k=1}^{lN} \frac{\partial}{\partial p_y}\,{}_l\Psi_k(\mathbf{p}_l) \sum_{n=1}^{lN} {}_l\underline{\psi}_{kn}^{-1}{}_l (v_{0y}\rho_0 h_0)_n + \right. \\
&\left(\sum_{k=1}^{lN} \frac{\partial}{\partial p_x}\,{}_l\Psi_k(\mathbf{p}_l) \sum_{n=1}^{lN} {}_l\underline{\psi}_{kn}^{-1}{}_l k_{0n} \right)\cdot\left(\sum_{k=1}^{lN} \frac{\partial}{\partial p_x}\,{}_l\Psi_k(\mathbf{p}_l) \sum_{n=1}^{lN} {}_l\underline{\psi}_{kn}^{-1}{}_l T_{0n} \right) + \\
&\left(\sum_{k=1}^{lN} \frac{\partial}{\partial p_y}\,{}_l\Psi_k(\mathbf{p}_l) \sum_{n=1}^{lN} {}_l\underline{\psi}_{kn}^{-1}{}_l k_{0n} \right)\cdot\left(\sum_{k=1}^{lN} \frac{\partial}{\partial p_y}\,{}_l\Psi_k(\mathbf{p}_l) \sum_{n=1}^{lN} {}_l\underline{\psi}_{kn}^{-1}{}_l T_{0n} \right) + \\
&\left. \left(\sum_{n=1}^{lN} \frac{\partial^2}{\partial p_x^2}\,{}_l\Psi_k(\mathbf{p}_l) \sum_{n=1}^{lN} {}_l\underline{\psi}_{kn}^{-1}{}_l T_{0n} + \sum_{n=1}^{lN} \frac{\partial^2}{\partial p_y^2}\,{}_l\Psi_k(\mathbf{p}_l) \sum_{n=1}^{lN} {}_l\underline{\psi}_{kn}^{-1}{}_l T_{0n} \right) \right)
\end{aligned}
$$

$$(5.44)$$

and in axisymmetry (p_r, p_z) is

$$
\begin{aligned}
h_l = h_{0l} + \frac{\Delta t}{\rho_0} &\left(\sum_{k=1}^{lN} \frac{\partial}{\partial p_r}\,{}_l\Psi_k(\mathbf{p}_l) \sum_{n=1}^{lN} {}_l\underline{\psi}_{kn}^{-1}{}_l (v_{0x}\rho_0 h_0)_n + \right. \\
&\sum_{k=1}^{lN} \frac{\partial}{\partial p_z}\,{}_l\Psi_k(\mathbf{p}_l) \sum_{n=1}^{lN} {}_l\underline{\psi}_{kn}^{-1}{}_l (v_{0y}\rho_0 h_0)_n + \\
&\left(\sum_{k=1}^{lN} \frac{\partial}{\partial p_r}\,{}_l\Psi_k(\mathbf{p}_l) \sum_{n=1}^{lN} {}_l\underline{\psi}_{kn}^{-1}{}_l k_{0n} \right)\cdot\left(\sum_{k=1}^{lN} \frac{\partial}{\partial p_r}\,{}_l\Psi_k(\mathbf{p}_l) \sum_{n=1}^{lN} {}_l\underline{\psi}_{kn}^{-1}{}_l T_{0n} \right) + \\
&\left(\sum_{k=1}^{lN} \frac{\partial}{\partial p_z}\,{}_l\Psi_k(\mathbf{p}_l) \sum_{n=1}^{lN} {}_l\underline{\psi}_{kn}^{-1}{}_l k_{0n} \right)\cdot\left(\sum_{k=1}^{lN} \frac{\partial}{\partial p_z}\,{}_l\Psi_k(\mathbf{p}_l) \sum_{n=1}^{lN} {}_l\underline{\psi}_{kn}^{-1}{}_l T_{0n} \right) + \\
&\left(\frac{1}{p_r} \sum_{n=1}^{lN} \frac{\partial}{\partial p_r}\,{}_l\Psi_k(\mathbf{p}_l) \sum_{n=1}^{lN} {}_l\underline{\psi}_{kn}^{-1}{}_l T_{0n} + \sum_{n=1}^{lN} \frac{\partial^2}{\partial p_r^2}\,{}_l\Psi_k(\mathbf{p}_l) \sum_{n=1}^{lN} {}_l\underline{\psi}_{kn}^{-1}{}_l T_{0n} + \right. \\
&\left.\left. \sum_{n=1}^{lN} \frac{\partial^2}{\partial p_z^2}\,{}_l\Psi_k(\mathbf{p}_l) \sum_{n=1}^{lN} {}_l\underline{\psi}_{kn}^{-1}{}_l T_{0n} \right) \right)
\end{aligned}
$$
,

$$(5.45)$$

where the formulas (4.6) and (4.7) have been employed.

The complete solution procedure follows the below defined steps 1-5.

Step 1
First, the initial conditions are set in the domain and boundary nodes and the required derivatives are calculated from the known nodal values.

Step 2
The equation (5.44) is used to calculate the new values of the variable $_l h_n$ at time $t_0 + \Delta t$ in the domain nodes.

Step 3
The temperature field is calculated from the enthalpy field using the inverse of the constitutive temperature-enthalpy relationships (equations (2.12) and (2.13)), i.e.

$$T_l = T(h) \qquad (5.46)$$

Step 4
The unknown function variable $_l T_n$ at time $t_0 + \Delta t$ in the Dirichlet, Neumann, and Robin boundary nodes is calculated. The calculation is performed in the same way as in Section 5.2, equations (5.22)-(5.26).

Step 5
The unknown boundary values are set from equation (4.5).

The steady-state is achieved when the criterion (5.27) is met.

5.5 Treatment of the convective-diffusive equation with phase change and a material moving boundaries

The solution of the problem is given, which is characterized by a moving mushy domain between the solid and the liquid phase and a material moving boundary. While the boundary interface is moving, the domain is growing or shrinking. There are several industrial applications with such kind of physical behaviour, like semi-continuous casting of aluminium alloys where the bottom block is moving downwards. The solution is obtained with the same equations (5.38)-(5.45) and the same solution procedure as in Section 5.4, except two additional steps are added.

The complete solution procedure is defined by steps 1-7.

Steps 1-5

The *Steps 1-5* in Section 5.4 are used.

Step 6

The boundary nodes on a material moving boundary are moved according to the velocity and time step length

$$\Delta s_l = \mathbf{v}_{0l} \cdot \Delta t \ . \tag{5.47}$$

Step 7

The unknown values of $\Gamma(t_0 + \Delta t)$ on a material moving boundary are extrapolated by equation (4.5). When the distance between the moving boundary nodes and the fixed domain exceeds two times the typical node distance of the discretization, new inner nodes are inserted between the moving boundary nodes and the inner nodes. Their values are obtained by the LRBFCM, equation (4.5). The growth of the domain and the respective node manipulations are represented in Figure 5.1.
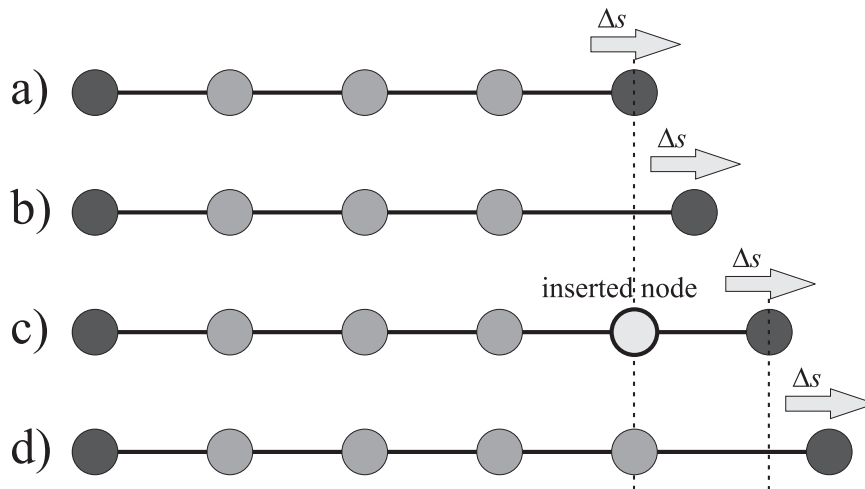
Figure 5.1: Schematic representation of nodes manipulations. a,b) Boundary node is moved by Δs ; c) New node is inserted between the boundary and the domain node; d) Boundary node is moved by Δs . Black points represent the boundary nodes and the gray points the domain nodes.

The calculation is stopped when the time of calculation exceeds the foreseen time of interest. The steady-state can also be achieved when the criterion (5.27) is met.

6 Numerical examples

In this section numerical examples are presented to demonstrate the ability, accuracy and stability of the LRBFCM. Five examples, further named as tests, are given with complete description, solution procedure and numerical results. The results are compared with solutions obtained with classical mesh methods or analytical solutions.

Tests 1 and 2
Both tests show the ability of solving 2D diffusion problem with different boundary conditions. The first test is the boundary value problem (NAFEMS test) associated with the steady temperature field with simultaneous involvement of the Dirichlet, Neumann and Robin boundary conditions on a rectangle. The second test is the initial value problem, associated with the Dirichlet jump problem on a square. Results of both tests are compared with the analytical and FDM solutions.

Test 3
The one-dimensional steady-state convective-diffusive problem is solved with and without phase change. The results are compared with the analytical solution and solutions solved with the FEM and the DR-BEM.

Test 4
The steady-state DC casting problem with non-linear material properties is solved. The results are compared with the FVM solution.

Test 5
DC casting with start-up phase simulation. This test shows the ability of solving problems with a material moving boundaries. The results are compared with the FVM solution.

By default in all tests the uniform node arrangements are used. In order to show the power of meshless method we also perform some calculations for the *First*

and *Fourth* tests on non-uniform node arrangements with random node distribution. All tests with numerical characteristics are presented in Table 6.1.

Table 6.1: Tests with numerical characteristics.

	Test 1	*Test 2*	*Test 3*	*Test 4*	*Test 5*
Diffusion	YES	YES	YES	YES	YES
Convection	NO	NO	YES	YES	YES
Phase change	NO	NO	YES	YES	YES
Time dependent	NO	YES	NO	NO	YES
Non-linear material properties	NO	NO	NO	YES	YES
Dimensions	2D	1D	1D	2D	axisymmetry
Boundary conditions					
Dirichlet	YES	YES	YES	YES	YES
Neumann	YES	YES	YES	YES	YES
Robin	YES	NO	NO	YES nonlinear	YES nonlinear
Published in	[Šarler and Vertnik, 2006]	[Šarler and Vertnik, 2006]	[Vertnik and Šarler, 2006]	[Vertnik and Šarler, 2006]	[Vertnik *et al.*, 2006]

6.1 Error measures

For all tests the following error measures of the numerical solution was choosen:
a) the maximum absolute error

$$\phi_{\max} = \max \left| \phi\left(\mathbf{p}_n, t\right) - \phi_{\text{ana}}\left(\mathbf{p}_n, t\right) \right|; \ n = 1, 2, ..., N , \qquad (6.1)$$

b) the average absolute error

$$\phi_{\text{avg}} = \frac{1}{N} \sum_{n=1}^{N} \left| \phi\left(\mathbf{p}_n, t\right) - \phi_{\text{ana}}\left(\mathbf{p}_n, t\right) \right|; \ n = 1, 2, ..., N \ \text{and} \qquad (6.2)$$

c) the root mean square error

$$\phi_{RMS} = \frac{1}{N}\sqrt{\sum_{n=1}^{N}\big(\phi(\mathbf{p}_n,t)-\phi_{\mathrm{ana}}(\mathbf{p}_n,t)\big)^2} \; ; \; n=1,2,...,N \,, \qquad (6.3)$$

where ϕ and ϕ_{ana} stand for numerical and analytical solution of the transport variable, N represents the total number of all nodes $\mathbf{p}_n$ of which first N_Γ nodes correspond to the boundary and the remaining N_Ω to the domain. The node with the maximum temperature error is denoted as $\mathbf{p}_{\mathrm{max}}$.

6.2 Diffusion problem

6.2.1 Test 1: Boundary value problem

6.2.1.1 Problem description
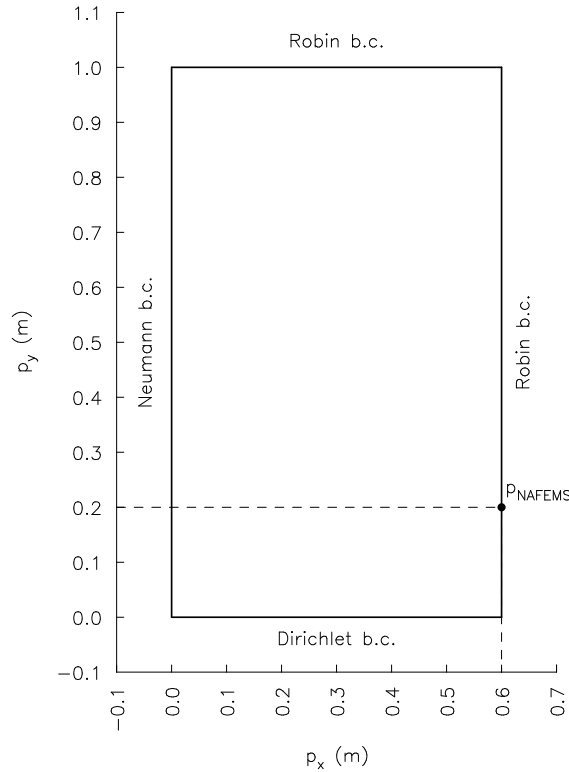
Figure 6.1: Test 1: NAFEMS benchmark test with boundary conditions and dimensions.

The problem is posed on a two dimensional rectangular domain $\Omega: p_x^- < p_x < p_x^+$, $p_y^- < p_y < p_y^+$, and boundary $\Gamma_x^-: p_x = p_x^-$, $p_y^- \le p_y \le p_y^+$, $\Gamma_x^+: p_x = p_x^+$, $p_y^- \le p_y \le p_y^+$, $\Gamma_y^-: p_y = p_y^-$, $p_x^- \le p_x \le p_x^+$, $\Gamma_y^+: p_y = p_y^+$, $p_x^- \le p_x \le p_x^+$ with $p_x^- = 0\,\mathrm{m}$, $p_x^+ = 0.6\,\mathrm{m}$, $p_y^- = 0\,\mathrm{m}$, $p_y^+ = 1.0\,\mathrm{m}$ (Figure 6.1). The material

properties are $\rho_0 = 7850\,\text{kg/m}^3$, $c_{p0} = 460\,\text{J/(kgK)}$, and $k_0 = 52\,\text{W/(mK)}$. The boundary conditions are on the south boundary Γ_y^- of the Dirichlet type with $T_\Gamma^D = 100\,^\circ\text{C}$, on the east and north boundaries Γ_x^+ and Γ_y^+ of the Robin type with $T_\Gamma^R = -h_{TC}/k$, $h_{TC} = 750\,\text{W/(m}^2\text{K)}$, $T_{\Gamma ref}^R = 0\,^\circ\text{C}$ and on the west boundary Γ_x^- of the Neumann type with $T_\Gamma^N = 0\,\text{W/m}^2$.

This solution represents the NAFEMS benchmark test 10 and is in document [Cameron *et al.*, 1986] given in terms of analytical value for temperature $T_{\text{NAFEMS}} = 18.25\,^\circ\text{C}$ at $p_{\text{NAFEMS}x} = 0.6\,\text{m}$, $p_{\text{NAFEMS}y} = 0.2\,\text{m}$. The rounded eight digit accurate analytical solution $T_{\text{NAFEMS}} = 18.253756\,^\circ\text{C}$ is used in this thesis calculated by the analytical solution defined in Appendix A.1. The analytical solution has been calculated also in all computational nodes in order to be able to calculate the error measures that follow.

6.2.1.2 Numerical results

The calculations are performed on three uniform node arrangements 13×21 ($N = 269, N_\Gamma = 60, N_\Omega = 209$), 31×51 ($N = 1577, N_\Gamma = 156, N_\Omega = 1421$), 61×101 ($N = 6157, N_\Gamma = 316, N_\Omega = 5841$), and on the non-uniform node arrangement 61×101 ($N = 6157, N_\Gamma = 316, N_\Omega = 5841$). A schematics of the uniform node arrangement 31×51 is shown in Figure 6.2(left). A randomly displaced non-uniform node arrangement is generated from the uniform node arrangement through transformation

$$p_{n\varsigma(\text{nonuniform})} = p_{n\varsigma(\text{uniform})} + c_{\text{random}}\,\delta r_{\min}\,p_{n\varsigma(\text{uniform})}\,;\ \varsigma = x, y\,, \tag{6.4}$$

where c_{random} represents a random number $-1 \le c_{\text{random}} \le +1$, δ represents a displacement factor (in this work fixed to 0.25), and $r_{\min}$ the minimum distance between the two nodes in uniform node arrangement. The boundary nodes are displaced only in the direction perpendicular to the boundary normal. A schematics of the randomly displaced non-uniform node arrangement 31×51 is shown in Figure 6.2(right). The steady state is approached by a transient calculation using a fixed time-step $\Delta t = 1\,\text{s}$ in uniform node arrangements and $\Delta t = 0.5\,\text{s}$ in non-uniform node arrangement. The steady state criterion used in all computations is $T_{ste} = 10^{-6}\,^\circ\text{C}$. Figure 6.3 shows the calculated temperature field with isotherms.
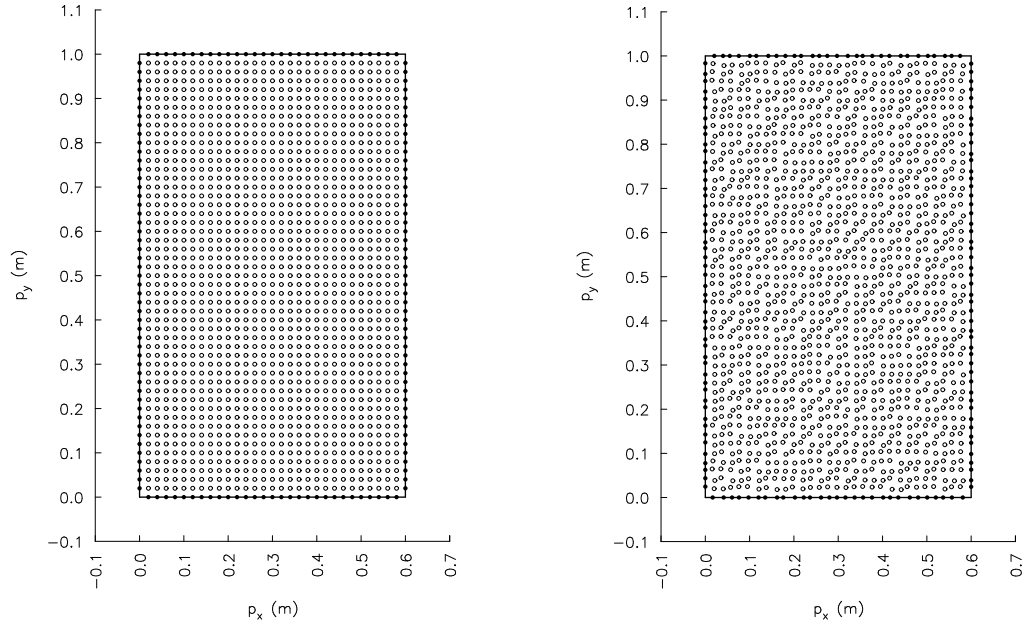
Figure 6.2: Test 1: Node arrangements. Left - $31{\times}51$ uniform node arrangement. Right - $31{\times}51$ non-uniform randomly displaced node arrangement.
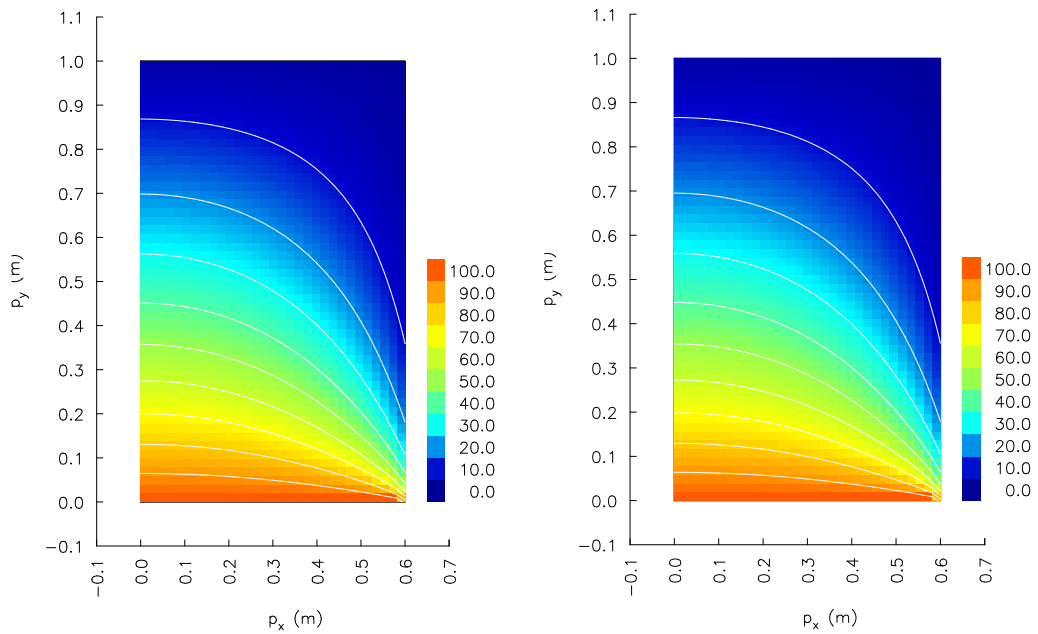
Figure 6.3: Test 1: Calculated temperature field. Left - $31{\times}51$ uniform node arrangement with $5{\times}5$ influence domain and $c = 32$. Right - $31{\times}51$ non-uniform randomly displaced node arrangement with $9{\times}9$ influence domain and $c = 5$. White lines represent isotherms with the spacing $10.0\,°C$. The first plotted isotherm on the bottom is $90.0\,°C$.

Tables 6.2-6.4 show accuracy of the solution as a function of MQs free parameter c for different node arrangements and five-noded influence domain. One can observe the improvement of the accuracy with higher values of c (Figures 6.4 and 6.6) and denser nodes (Figure 6.5). One can also observe that in case the value of c is fixed far from the optimal value (i.e. 1 or 2) the method does not converge with denser nodes. The solution above $c = 8$ shows only slight improvement in maximum error, however the average error can still be significantly improved when changing the parameter c from 8 to 16. The solution with node arrangement 13×21 and $c = 32$ did not converge. Table 6.5 shows the same type of information as Table 6.4, however with the nine-noded influence domain. In this case the solution with $c = 16$ and $c = 32$ did not converge. This result is consistent with the fact that more nodes are used in MQs collocation methods more the free parameter is restricted to smaller values. Comparison of Tables 6.4 and 6.5 shows that better results can be achieved with smaller influence domain. At the fixed parameter $c = 8$ the average error is smaller with the smaller influence domain and the maximum error is smaller with the larger influence domain. Next, the calculations are performed on the non-uniform randomly displaced node arrangement. Here, the results did not converge with the five-noded influence domain. Comparison of Tables 6.5 and 6.6 shows the expected degradation of the accuracy with the node arrangement randomization. Tables 6.7 and 6.8 show accuracy of the LRBFCM in the NAFEMS reference point as compared with the classical FDM. The accuracy of the meshless method with the uniform 61×101 node arrangement and five-noded influence domain is almost two orders of magnitude higher than with the FDM structured in the same grid nodes. The error is increased in case of non-uniform node arrangement. However, also in non-uniform case, the error in the reference point is only $0.2143\,°C$ (i.e. in the percent range) compared to the characteristic problem temperature difference of $100\,°C$.

Table 6.2: Test 1: Accuracy of the solution as a function of MQs free parameter c in terms of average and maximum errors and the position of maximum error for 13×21 node arrangement and five-noded influence domain.

c	$\Delta T_{avg}\,(°C)$	$\Delta T_{max}\,(°C)$	$p_{max\,x}\,(m)$	$p_{max\,y}\,(m)$
1	12.8558	29.9918	0.0000	0.3000
2	2.6133	5.5789	0.0000	0.3500
4	0.3114	3.4979	0.6000	0.0500
8	0.0891	3.1707	0.6000	0.0500
16	0.0719	3.0920	0.6000	0.0500
32	div			

Table 6.3: Test 1: Accuracy of the solution as a function of MQs free parameter c in terms of average and maximum errors and the position of maximum error for 31×51 node arrangement and five-noded influence domain.

c	ΔT_{avg} (˚C)	ΔT_{max} (˚C)	$p_{\max x}$ (m)	$p_{\max y}$ (m)
1	23.0263	57.0299	0.0000	0.2000
2	9.8407	21.5167	0.0000	0.3200
4	1.1828	2.9379	0.6000	0.0200
8	0.1087	2.5910	0.6000	0.0200
16	0.0261	2.5172	0.6000	0.0200
32	0.0196	2.4996	0.6000	0.0200

Table 6.4: Test 1: Accuracy of the solution as a function of MQs free parameter c in terms of average and maximum errors and the position of maximum error for 61×101 node arrangement and five-noded influence domain.

c	ΔT_{avg} (˚C)	ΔT_{max} (˚C)	$p_{\max x}$ (m)	$p_{\max y}$ (m)
1	27.8036	72.9256	0.0000	0.1300
2	18.5475	42.4449	0.0000	0.2500
4	3.9476	8.3054	0.0000	0.3500
8	0.3210	1.7675	0.6000	0.0100
16	0.0314	1.7042	0.6000	0.0100
32	0.0107	1.6903	0.6000	0.0100

Table 6.5: Test 1: Accuracy of the solution as a function of MQs free parameter c in terms of average and maximum error and the position of maximum error for 61×101 node arrangement and nine-noded influence domain.

c	ΔT_{avg} (˚C)	ΔT_{max} (˚C)	$p_{\max x}$ (m)	$p_{\max y}$ (m)
1	21.3924	50.4141	0.0000	0.2200
2	7.0673	15.0366	0.0000	0.3300
4	0.6918	1.4331	0.0000	0.3700
8	0.0704	0.8284	0.6000	0.0100
16	div			
32	div			

Table 6.6: Test 1: Accuracy of the solution as a function of MQs free parameter c in terms of average and maximum error and the position of maximum error for 61×101 non-uniform node arrangement and nine-noded influence domain.

c	ΔT_{avg} (°C)	$\Delta T_{\max}$ (°C)	$p_{\max x}$ (m)	$p_{\max y}$ (m)
1	22.5573	53.1913	0.0000	0.2113
2	9.3926	20.0383	0.0000	0.3191
4	1.2326	2.5587	0.0000	0.3897
5	0.5637	1.1684	0.0000	0.3897
16	div			
32	div			

Table 6.7: Test 1: Accuracy of the solution in NAFEMS reference point $\mathbf{p}_{\mathit{NAFEMS}}$ as a function of nodes density for different node arrangements and number of nodes in the influence domain.

node arrangement	nodes	c	T (°C)	$T - T_{\mathrm{NAFEMS}}$ (°C)
13×21	5	16	18.3613	0.1075
31×51	5	32	18.2855	0.0317
61×101	5	32	18.2594	0.0056
61×101 (uniform)	9	8	18.2512	-0.0026
61×101 (nonuniform)	9	5	18.0395	0.2143

Table 6.8: Test 1: Accuracy of the classical FDM solution in NAFEMS reference point as a function of regular grid density.

Grid	T (°C)	$T - T_{\mathrm{NAFEMS}}$ (°C)
61×101	17.9827	-0.2711
121×201	18.1074	-0.1464
241×401	18.1754	-0.0783
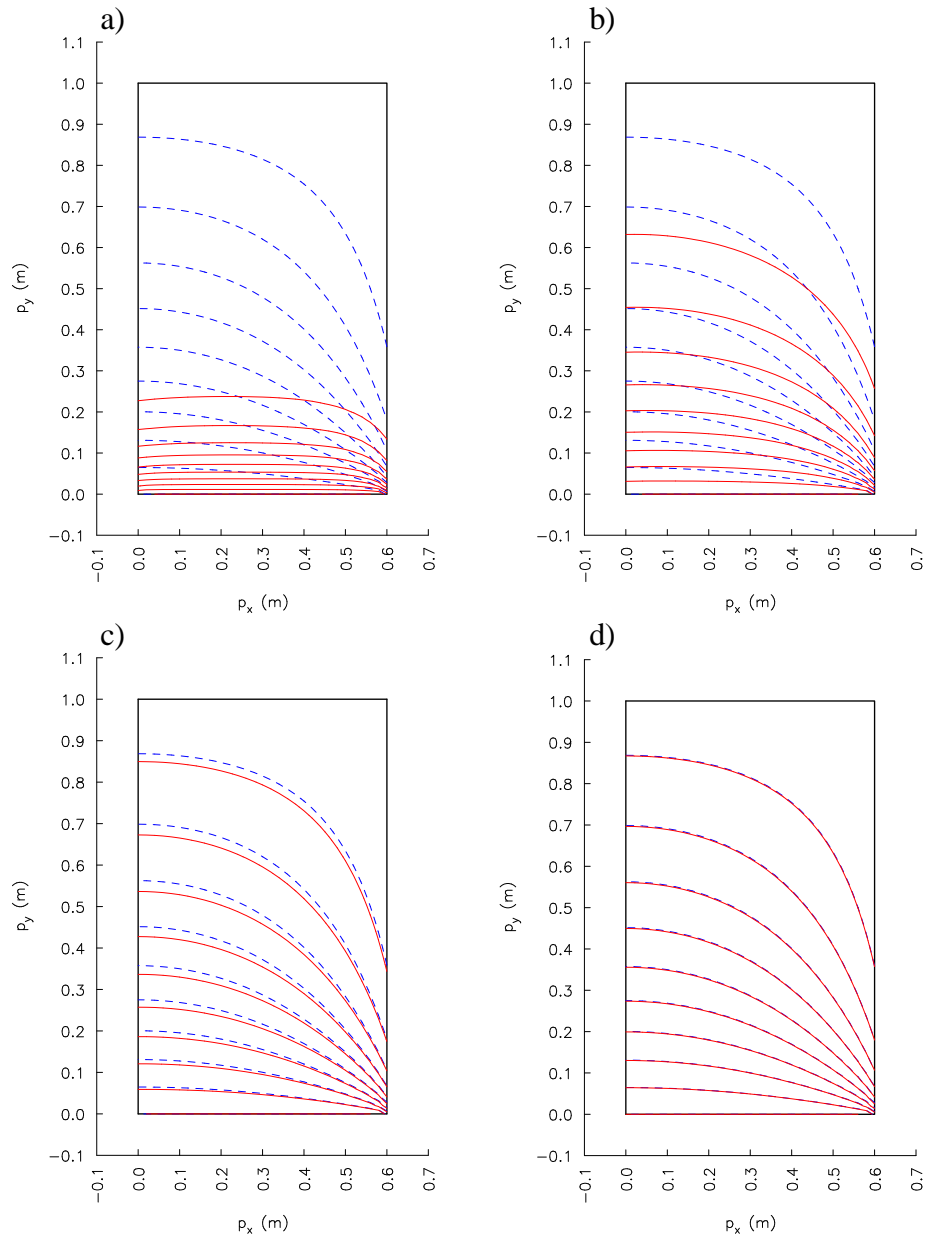
Figure 6.4: Test 1: Calculated isotherms by the LRBFCM with different values of free parameter for 31×51 uniform node arrangement. Blue isotherms with dashed line style represents analytical solution. Red isotherms with solid line style represents solution calculated with LRBFCM with the following values of free parameter: a) $c = 1$, b) $c = 2$, c) $c = 4$ and d) $c = 8$. The spacing between the isotherms is $10.0\,^{\circ}\text{C}$. The first plotted isotherm on the bottom is at $90.0\,^{\circ}\text{C}$.
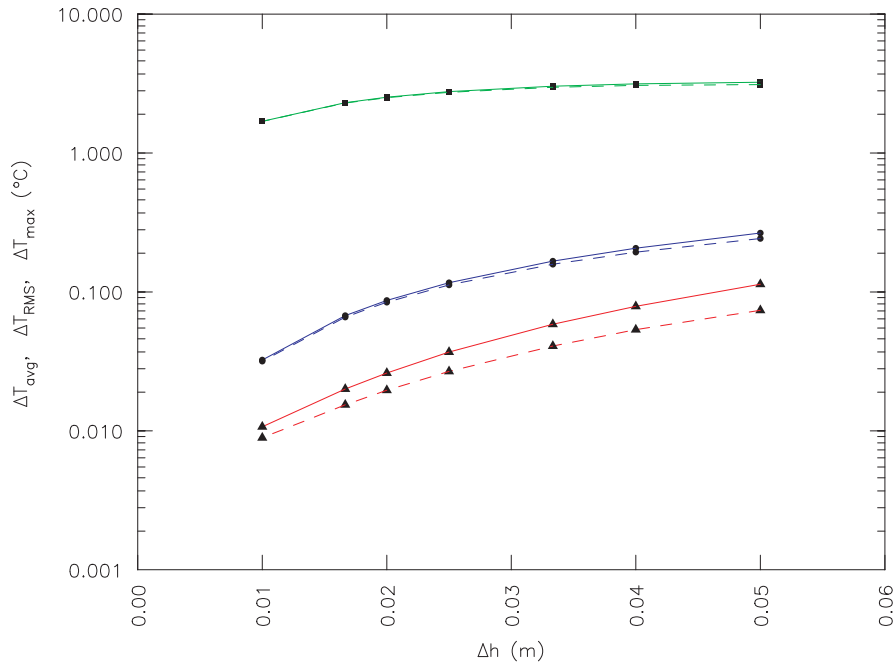
Figure 6.5: Test 1: Convergence plots as a function of the minimum node distance for the five-noded influence domain and two node arrangements. Green curves – the maximum error, blue curves – the RMS error and red curves – the average error. Solid line – 31×51 node arrangement, dashed line – 61×101 node arrangement. ■ – maximum error, ● – RMS error and ▲ – average error.
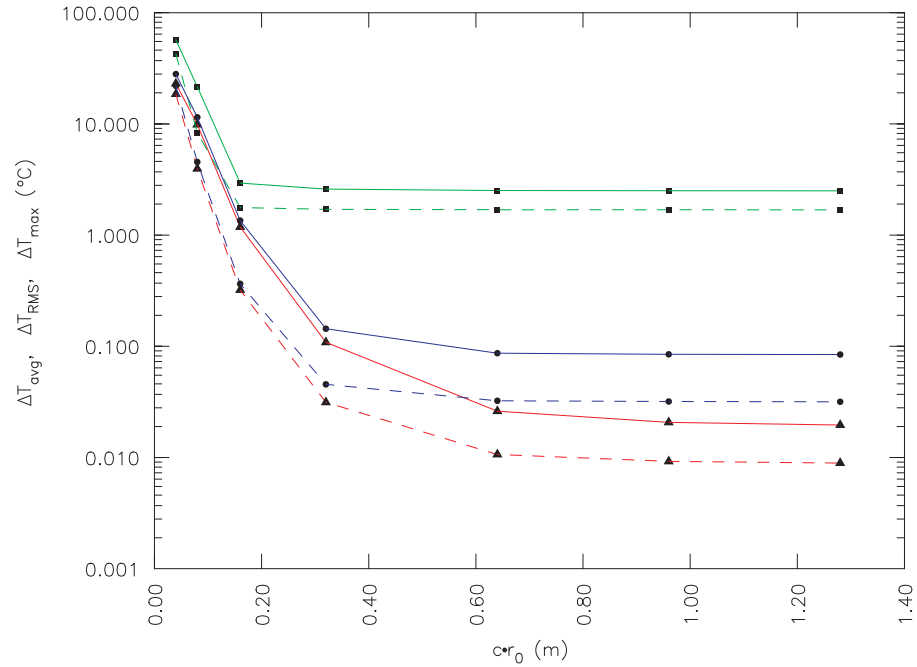
Figure 6.6: Test 1: Convergence plots as a function of the MQs parameters for the five-noded influence domain and two node arrangements. Green curves - the maximum error, blue curves – the RMS error and red curves – the average error. Solid line – 31×51 node arrangement, dashed line – 61×101 node arrangement. ■ – maximum error, ● – RMS error and ▲ – average error.

6.2.2 Test 2: Initial value problem

6.2.2.1   Problem description
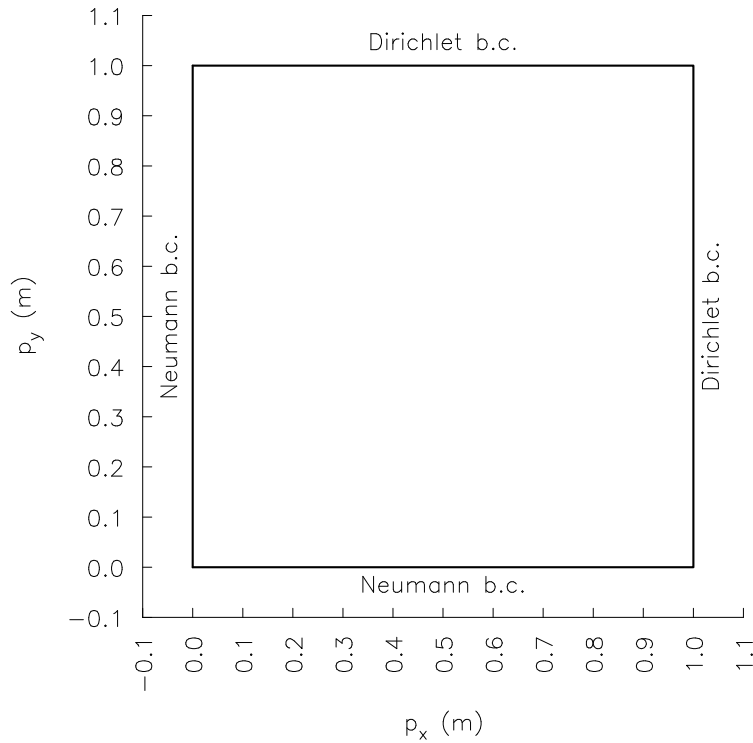
Figure 6.7: Test 2: Initial value problem with boundary conditions and dimensions.

The geometry of the problem is formally posed on a similar region as the first test case, however the region is square with $p_x^- = 0\,\text{m}$ $p_x^+ = 1.0\,\text{m}$ $p_y^- = 0\,\text{m}$ $p_y^+ = 1.0\,\text{m}$ (Figure 6.7). The material properties are set to unit values $\rho_0 = 1\,\text{kg/m}^3$, $c_{p0} = 1\,\text{J/(kgK)}$, $k_0 = 1\,\text{W/(mK)}$. Boundary conditions on the east Γ_x^+ and north boundaries Γ_y^+ are of the Dirichlet type with $T_\Gamma^D = 0\,^\circ\text{C}$, and on the west Γ_x^- and south boundaries Γ_y^- are of the Neumann type with $T_\Gamma^N = 0\,\text{W/m}^2$. The initial conditions are $T_0 = 1\,^\circ\text{C}$. The analytical solution of the test can be found in Appendix A.2, where here only the solution of the upper-right quadrant is considered.
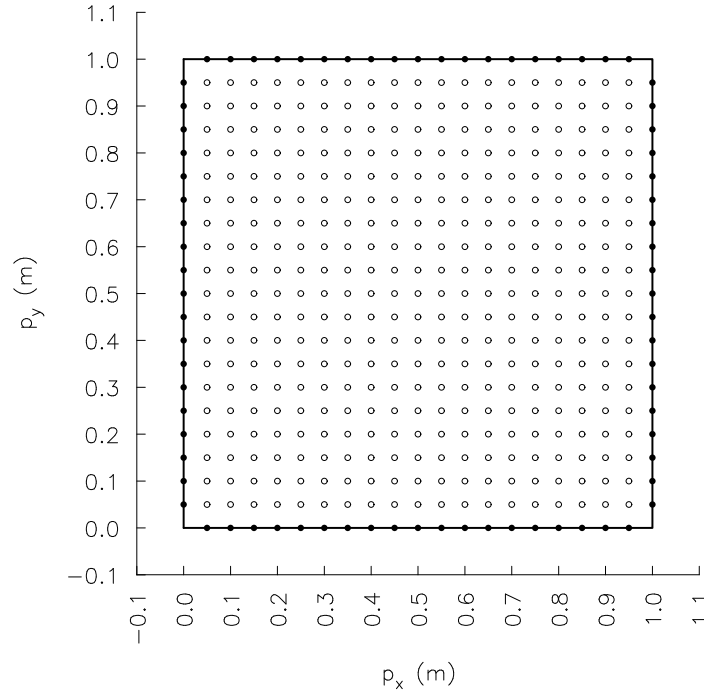
Figure 6.8: Test 2: Representation of the 21×21 uniform node arrangement.

6.2.2.2   Numerical results

The calculations are performed on four different uniform node arrangements 11×11 ($N=117$, $N_\Gamma=36$, $N_\Omega=81$), 21×21 ($N=437$, $N_\Gamma=76$, $N_\Omega=361$), 41×41 ($N=1677$, $N_\Gamma=156$, $N_\Omega=1521$), 101×101 ($N=10197$, $N_\Gamma=396$, $N_\Omega=9801$), and five-noded influence domain, respectively. 21×21 node arrangement is represented in Figure 6.8. The time-steps $\Delta t=10^{-4}$ s and $\Delta t=10^{-5}$ s are used in the calculations with 41×41 node arrangement. The accuracy of the method is assessed in terms of the maximum and average errors at times $t=0.001$ s, $t=0.01$ s, $t=0.1$ s, and $t=1.0$ s. Tables 6.9-6.11 show accuracy of the solution as a function of MQs free parameter c for different grid arrangements and five-noded influence domain. Calculated temperature fields for 41×41 node arrangement are plotted in Figure 6.9. As in previous test, one can observe the improvement of the accuracy with higher values of c and denser node arrangement. Comparison of Tables 6.11 and 6.12 shows expected convergence properties of the method, that better results can be achieved with reduction of the time-step from $\Delta t=10^{-4}$ s to $\Delta t=10^{-5}$ s. Information in Tables 6.13 and 6.14 show similar accuracy of the developed method as compared with the classical FDM at shorter times $t=0.001$ s and $t=0.01$ s immediately after the abrupt boundary conditions jump, and an order of magnitude better accuracy at longer transient times $t=0.1$ s and $t=1.0$ s. The comparison is also shown in

Figure 6.10, where the different errors are plotted as a function of time. The method is unstable with the time-step $\Delta t = 10^{-3}$ s because of the explicit approach.

Table 6.9: Test 2: Accuracy of the solution as a function of MQs free parameter c at times $t = 0.001$ s, $t = 0.01$ s, $t = 0.1$ s, and $t = 1.0$ s in terms of average error, maximum error and the position of the maximum error for 11×11 node arrangement with five-noded influence domain and $\Delta t = 10^{-4}$ s.

t (s)	c	ΔT_{avg} (°C)	ΔT_{max} (°C)	$p_{max\,x}$ (m)	$p_{max\,y}$ (m)
0.001	8	1.184E-2	1.259E-1	0.900	0.900
0.001	16	1.182E-2	1.255E-1	0.900	0.900
0.001	32	1.181E-2	1.254E-1	0.900	0.900
0.01	8	4.862E-3	2.286E-2	0.700	0.700
0.01	16	4.767E-3	2.245E-2	0.700	0.700
0.01	32	4.746E-3	2.235E-2	0.700	0.700
0.1	8	1.242E-3	3.471E-3	0.200	0.200
0.1	16	7.139E-4	2.592E-3	0.200	0.200
0.1	32	6.239E-4	2.403E-3	0.200	0.200
1.0	8	6.997E-5	1.792E-4	0.100	0.100
1.0	16	9.068E-6	2.818E-5	0.100	0.100
1.0	32	4.681E-6	1.120E-5	0.300	0.000

Table 6.10: Test 2: Accuracy of the solution as a function of MQs free parameter c at times $t = 0.001$ s, $t = 0.01$ s, $t = 0.1$ s, and $t = 1.0$ s in terms of average error, maximum error and the position of the maximum error for 21×21 node arrangement with five-noded influence domain and $\Delta t = 10^{-4}$ s.

t (s)	c	ΔT_{avg} (°C)	ΔT_{max} (°C)	$p_{max\,x}$ (m)	$p_{max\,y}$ (m)
0.001	8	4.593E-3	4.413E-2	0.900	0.900
0.001	16	4.527E-3	4.377E-2	0.900	0.900
0.001	32	4.512E-3	4.368E-2	0.900	0.900
0.01	8	1.574E-3	7.121E-3	0.750	0.750
0.01	16	1.329E-3	6.421E-3	0.750	0.750
0.01	32	1.282E-3	6.255E-3	0.750	0.750
0.1	8	1.241E-3	2.387E-3	0.200	0.200
0.1	16	4.344E-4	1.032E-3	0.150	0.150
0.1	32	2.868E-4	8.154E-4	0.150	0.150
1.0	8	1.071E-4	2.695E-4	0.050	0.050
1.0	16	2.046E-5	5.262E-5	0.050	0.050
1.0	32	4.730E-6	1.337E-5	0.050	0.050

Table 6.11: Test 2: Accuracy of the solution as a function of MQs free parameter c at times $t = 0.001\,$s, $t = 0.01\,$s, $t = 0.1\,$s, and $t = 1.0\,$s in terms of average error, maximum error and the position of the maximum error for 41×41 node arrangement with five-noded influence domain and $\Delta t = 10^{-4}\,$s.

t (s)	c	ΔT_{avg} (˚C)	ΔT_{max} (˚C)	$p_{max\,x}$ (m)	$p_{max\,y}$ (m)
0.001	8	1.798E-3	2.405E-2	0.950	0.950
0.001	16	1.699E-3	2.319E-2	0.950	0.950
0.001	32	1.679E-3	2.298E-2	0.950	0.950
0.01	8	1.033E-3	3.678E-3	0.825	0.825
0.01	16	6.092E-4	2.647E-3	0.825	0.825
0.01	32	5.415E-4	2.418E-3	0.825	0.825
0.1	8	2.036E-3	3.761E-3	0.025	0.025
0.1	16	3.815E-4	6.548E-4	0.400	0.400
0.1	32	1.815E-4	3.200E-4	0.450	0.450
1.0	8	2.113E-4	5.277E-4	0.025	0.025
1.0	16	3.115E-5	7.810E-5	0.025	0.025
1.0	32	9.160E-6	2.332E-5	0.025	0.025

Table 6.12: Test 2: Accuracy of the solution as a function of MQs free parameter c at times $t = 0.001\,$s, $t = 0.01\,$s, $t = 0.1\,$s, and $t = 1.0$ s in terms of average error, maximum error and the position of the maximum error for 41×41 node arrangement with five-noded influence domain and $\Delta t = 10^{-5}\,$s.

t (s)	c	ΔT_{avg} (˚C)	ΔT_{max} (˚C)	$p_{max\,x}$ (m)	$p_{max\,y}$ (m)
0.001	8	1.239E-3	1.571E-2	0.925	0.925
0.001	16	1.179E-3	1.502E-2	0.925	0.925
0.001	32	1.168E-3	1.485E-2	0.925	0.925
0.01	8	8.092E-4	2.641E-3	0.250	0.250
0.01	16	3.828E-4	1.772E-3	0.275	0.275
0.01	32	3.332E-4	1.623E-3	0.275	0.275
0.1	8	1.969E-3	3.864E-3	0.975	0.975
0.1	16	3.155E-4	6.328E-4	0.900	0.900
0.1	32	1.098E-4	3.037E-4	0.925	0.925
1.0	8	2.065E-4	5.152E-4	0.025	0.025
1.0	16	2.619E-5	6.539E-5	0.025	0.025
1.0	32	4.191E-6	1.058E-5	0.025	0.025

Table 6.13: Test 2: Accuracy of the solution at times $t = 0.001$ s, $t = 0.01$ s, $t = 0.1$ s, and $t = 1.0$ s in terms of average and maximum errors and the position of maximum error for 101×101 node arrangement, five-noded influence domain, fixed MQs free parameter $c = 32$ and $\Delta t = 10^{-5}$ s.

t (s)	c	ΔT_{avg} (°C)	ΔT_{max} (°C)	ΔT_{RMS} (°C)	$p_{max\,x}$ (m)	$p_{max\,y}$ (m)
0.001	32	2.352E-4	2.809E-3	5.190E-4	0.940	0.940
0.01	32	9.371E-5	3.523E-4	1.265E-4	0.800	0.800
0.1	32	9.243E-5	1.582E-4	1.069E-4	0.270	0.270
1.0	32	8.324E-6	2.066E-5	1.032E-5	0.010	0.010

Table 6.14: Test 2: Accuracy of the FDM solution at times $t = 0.001$ s, $t = 0.01$ s, $t = 0.1$ s, and $t = 1.0$ s in terms of average and maximum errors and the position of maximum error for 101×101 regular grid and $\Delta t = 10^{-5}$ s.

t (s)	Δt	ΔT_{avg} (°C)	ΔT_{max} (°C)	$p_{max\,x}$ (m)	$p_{max\,y}$ (m)
0.001	1.0E-5	1.368E-4	1.273E-3	0.925	0.950
0.01	1.0E-5	3.722E-4	1.298E-3	0.020	0.890
0.1	1.0E-5	3.363E-4	2.786E-3	0.000	0.010
1.0	1.0E-5	2.029E-4	5.649E-4	0.000	0.010
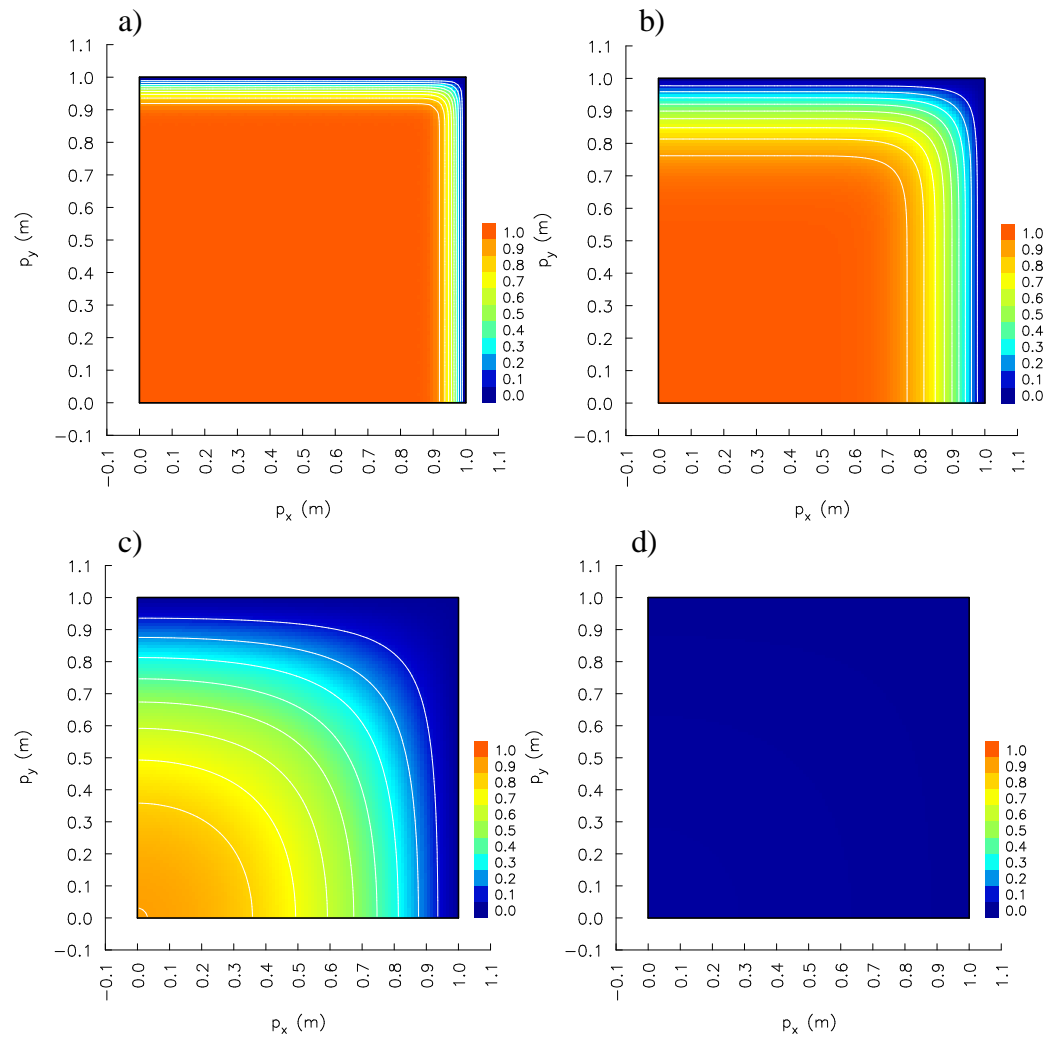
Figure 6.9: Test 2: Calculated temperature fields with LRBFCM for $41{\times}41$ node arrangement at different times. a) $t = 0.001\,\text{s}$, b) $t = 0.01\,\text{s}$, c) $t = 0.1\,\text{s}$ and d) $t = 1.0$ s. White lines represents isotherms with the spacing 0.1 K. The first plotted isotherm on the top is at 0.1 K.
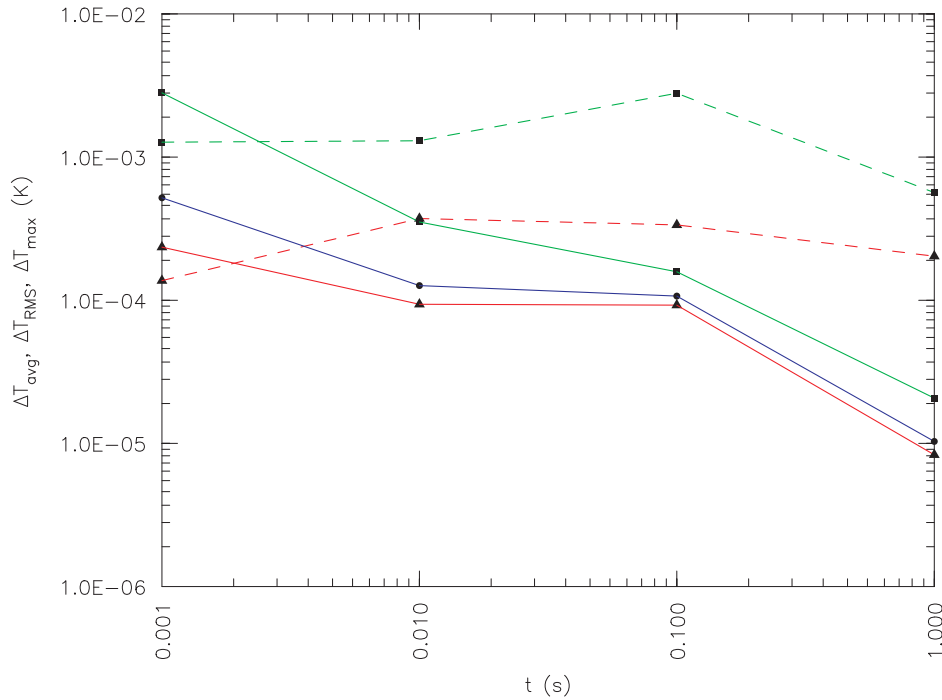
Figure 6.10: Test 2: Average (red curves), RMS (blue curves) and maximum (green curves) errors as a function of time calculated with the FDM and the developed method. Solid line – developed method, dashed line – FDM. ■ – maximum error, ● – RMS error and ▲ – average error.

6.3 Test 3: One-dimensional convective-diffusive phase-change problem

6.3.1 Problem description

The computations are done with uniform domain discretizations of the type $N' \times 3$, with $N = 3 \times N' - 4$, $N_\Gamma = 2 \times (N - 2) + 2$ and $N_\Omega = N - 2$, defined on a strip-shaped domains with longitudinal coordinates $p_x^- = 0\,\text{m}$, $p_x^+ = 1\,\text{m}$, and transversal coordinates $p_y^\pm = \pm 1.0\ \text{m}/(N' - 1)$. The schematics of 21×3 discretization is shown in Figure 6.11. The steady-state solution is reached through a transient from the initial uniform temperature $T_0 = T_\Gamma^-$ and a jump of the boundary conditions at p_x^- from $T_\Gamma^- = 0\,\text{K}$ to $T_\Gamma^+ = 1\,\text{K}$ for $t > t_0$ and stopped through the steady state criterion (equation (5.27)). The steady-state criterion used in all calculations in this test is $T_{\text{ste}} = 10^{-7}\,\text{K}$, reached with time-step $\Delta t = 10^{-5}$.
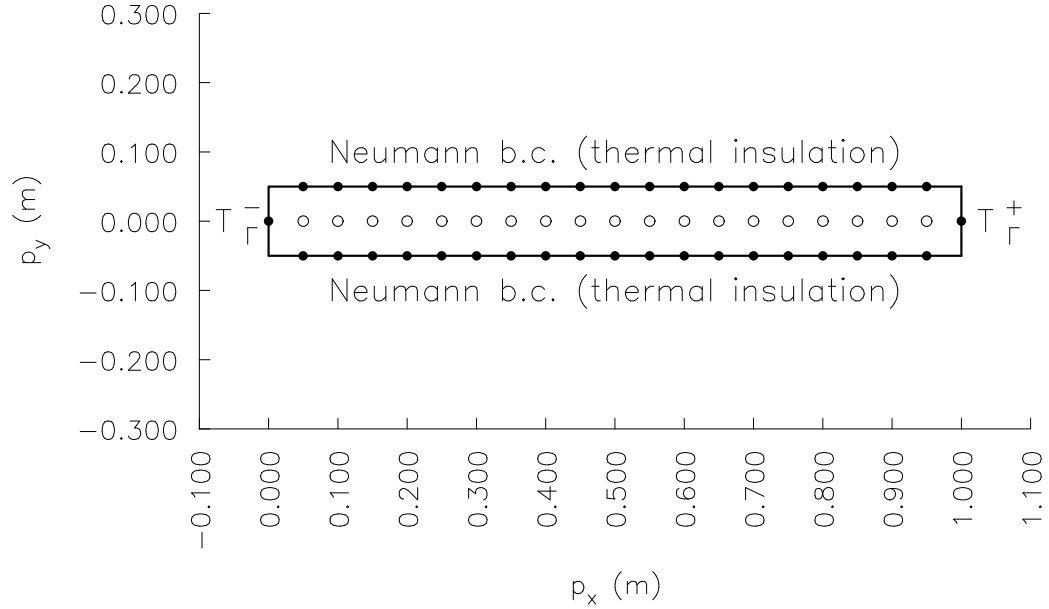
Figure 6.11: Test 3: Discretization schematics 21×3 with boundary conditions for solving the quasi-one-dimensional convective diffusive problem.

6.3.2 Numerical results

Space discretization sensitivity for material without phase change

The method is first tested with constant unit thermal properties and material without phase change, i.e. $h_m = 0 \, \text{J/(kgK)}$. The Péclet number in the following test is defined as

$$\text{Pe} = \frac{\rho_0 c_{p0} v_x \left(p_x^+ - p_x^- \right)}{k_0}. \tag{6.5}$$

The maximum absolute temperature error $T_{\max}$ and the average absolute temperature error T_{avg} are defined as in Section 6.1. The maximum relative nodal temperature and phase-change interface position errors are calculated from

$$
\gamma_{\max}(\%) = \left[\text{sign} \left(\gamma(\mathbf{p}_n, t) - \gamma_{\text{ana}}(\mathbf{p}_n, t) \right) / \gamma_{\text{ana}}(\mathbf{p}_n, t) \right] \cdot
$$
$$
\cdot \max \left| \left(\gamma(\mathbf{p}_n, t) - \gamma_{\text{ana}}(\mathbf{p}_n, t) \right) / \gamma_{\text{ana}}(\mathbf{p}_n, t) \right| \times 100\%; \, n = 1, 2, ..., N \tag{6.6}
$$

where γ and γ_{ana} stand for numerical and analytical solution of the phase-change interface position. The chosen error measures have been made compatible with the studies of [Dalhuijsen and Segal, 1986], [Pardo and Weckman, 1986], and [Šarler and Kuhn, 1998b].

Our investigation in Table 6.14 shows that the results are improving with the growth of the free parameter from 1 to 32 for both fine grids used 101×3, 201×3, and are optimal at 16 for grid 51×3.

It is also evident from Table 6.15 that the method converges with finer space discretization. From Table 6.16 and from Figure 6.12(a, b, c) we can conclude that the error is not growing with higher Péclet number as in conventional mesh methods. This is because of the interpolation with MQ-RBFs, where the curved functions are better approximated as linear or almost linear functions.

Table 6.15: Test 3: Material without phase change. Influence of the MQs free parameter on solution. $Pe = 20.0$ at three discretizations.

c	discretization	$c \cdot r_0$ (m)	T_{avg} (K)	T_{max} (K)
1.0	51×3	0.04	0.765300	0.98220000
1.0	101×3	0.02	0.880900	0.99970000
1.0	201×3	0.01	0.920500	0.99990000
2.0	51×3	0.08	0.247900	0.41920000
2.0	101×3	0.04	0.586300	0.82590000
2.0	201×3	0.02	0.823500	0.99450000
4.0	51×3	0.16	0.021349	0.03808800
4.0	101×3	0.08	0.084033	0.14730000
4.0	201×3	0.04	0.277900	0.45900000
8.0	51×3	0.32	0.001278	0.00321820
8.0	101×3	0.16	0.005665	0.01004100
8.0	201×3	0.08	0.023036	0.04078300
16.0	51×3	0.64	0.000633	0.00475410
16.0	101×3	0.32	0.000326	0.00076631
16.0	201×3	0.16	0.001448	0.00256500
32.0	51×3	1.28	0.000640	0.00485680
32.0	101×3	0.64	0.000155	0.00117190
32.0	201×3	0.32	0.000084	0.00017138

Table 6.16: Test 3: Material without phase change. Sensitivity of the results with respect to Péclet number at discretization 101×3 and the scaled MQs free parameter $c \cdot r_0 = 0.64$ m.

Pe	T_{avg} (K)	T_{max} (K)
0	0.000143	0.000224
10	0.000054	0.000202
20	0.000155	0.001172
30	0.000245	0.002734
40	0.000329	0.004864
50	0.000412	0.007854
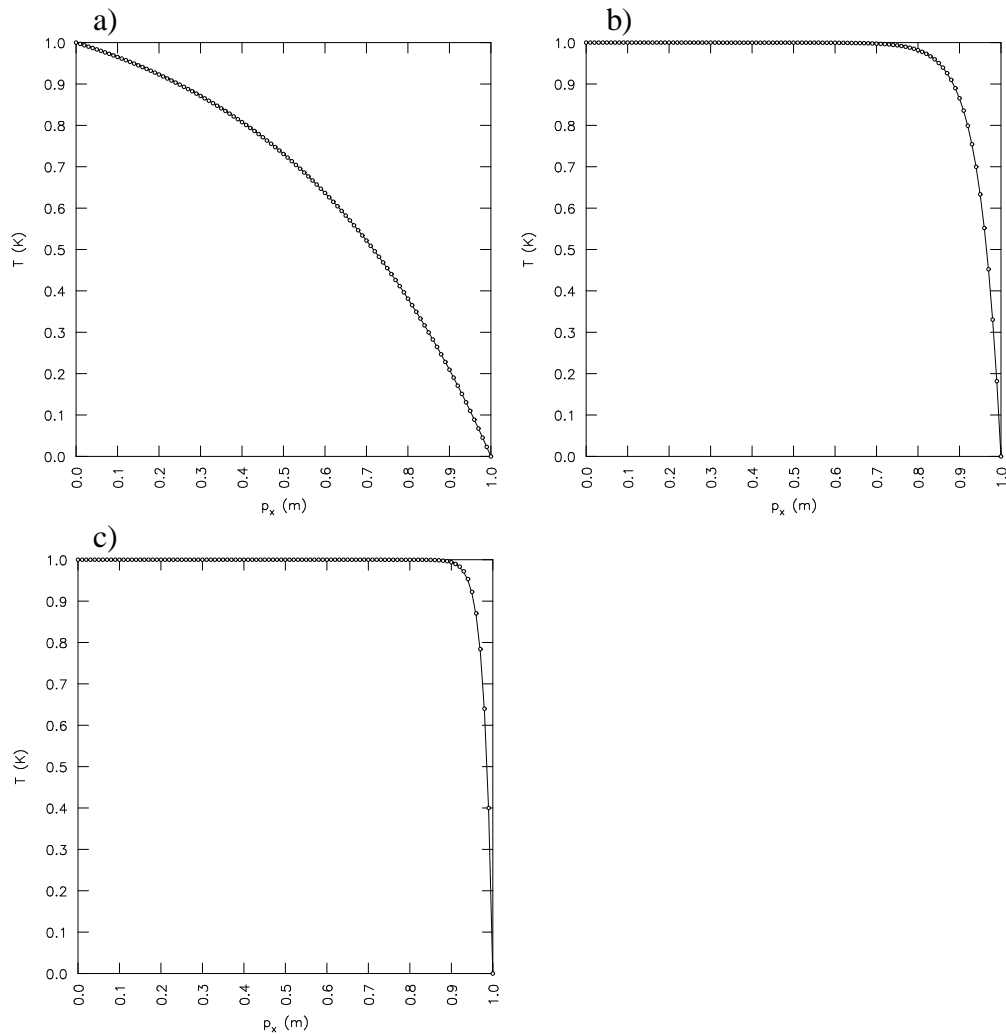
Figure 6.12: Test 3: Material without phase change. Comparison of the calculated temperatures ○ in the central nodes at $p_y = 0$ m with the analytical solution -. Discretization 101×3. (a) Pe = 2, (b) Pe = 20, (c) Pe = 50. The scaled MQs free parameter is set to $c \cdot r_0 = 0.64$ m.

Space discretization sensitivity for phase-change material
The method is tested next with the constant unit phase-change material. The isothermal melting temperature $T_m = 0.950\,\text{K}$ is, in the calculations, approximated by a narrow temperature range $T_S = 0.945\,\text{K}$, $T_L = 0.955\,\text{K}$ and linear variation of the liquid fraction over this temperature interval. The Stefan number, which defines the rate of solidification, is defined as

$$\text{Ste} = \frac{c_{p0}\left(T_\Gamma^- - T_\Gamma^+\right)}{h_m}\,. \tag{6.7}$$

Figure 6.13 shows the sensitivity of the method with respect to Péclet number, and Figure 6.14 shows the sensitivity of the method with respect to Stefan number. Related numerical data are given in Tables 6.17 and 6.18. The fact that the temperature accuracy degrades with lower Stefan numbers and higher Péclet numbers is a common expected feature of all one-domain methods. Sensitivity of the results with respect to the Péclet number (Table 6.17) obtained with the presented method did not gave the same facts, as at $\text{Pe} = 1.0$ the error is larger then at $\text{Pe} = 2.0$. Reason, similar as in previous test, can be in using radial basis functions for interpolation. All phase-change interface position errors have been evaluated at $p_y = 0\,\text{m}$ in this test. The position of the phase-change interface boundary is consistently under-predicted in cases with constant material properties of phases – a fact that compares well with the studies by [Pardo and Weckman, 1986], and [Šarler and Kuhn, 1998b]. Table 6.19 shows a comparison of the maximum relative temperature errors of LRBFCM with the reference FEM calculations [Pardo and Weckman, 1986] and Dual Reciprocity Boundary Element Method (DRBEM) calculations [Šarler and Kuhn, 1998b]. Comparison of the phase-change interface position error is shown in Table 6.20. The disrcetisation in FEM, that corresponds to LRBFCM discretization $N'\times 3$ is equal to $N'-1$ isoparametric hexahedral linear finite elements. The related discretization in DRBEM is equal to $2\times(N'-1)+4$ constant boundary elements and $N'-1$ domain nodes. The present method gives comparable results in terms of overall temperature accuracy and phase-change interface boundary position error at the compared node densities. The convergence of LRBFCM in this comparison exercise is illustrated in Figure 6.15.

Table 6.17: Test 3: Sensitivity of the results with respect to Péclet number at discretization 101×3, $\text{Ste} = 2.0$.

Pe	T_{avg} (K)	$T_{\max}$ (K)	p_{Mx} (m)	$p_{\text{err}\,x}$ (m)
0.5	0.000206	0.000635	0.089150	-0.000329
1.0	0.000977	0.002406	0.200251	-0.000161
2.0	0.000908	0.002528	0.513854	-0.003082
4.0	0.001064	0.004949	0.749926	-0.000662

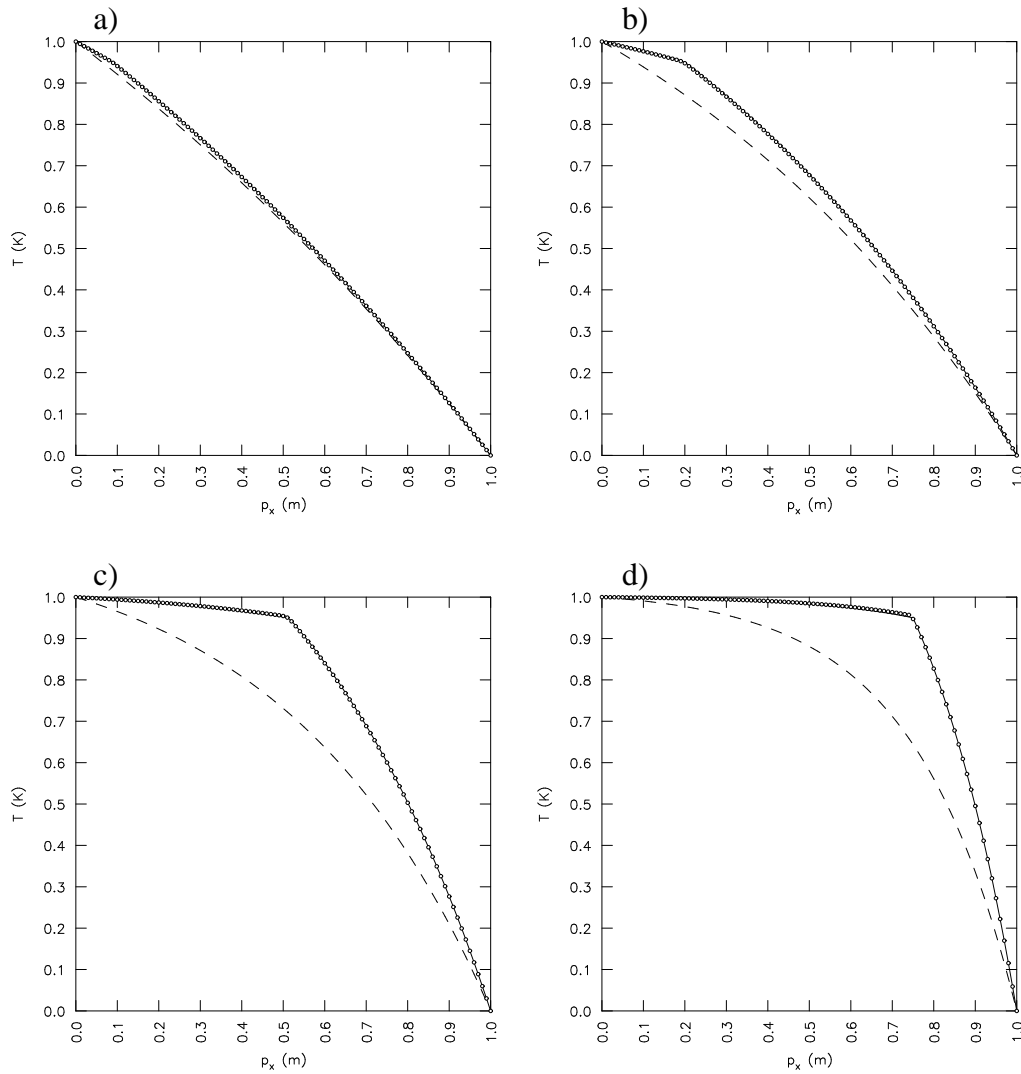**Table 6.18:** Test 3: Sensitivity of the results with respect to Stefan number at discretization 101×3, $\text{Pe} = 2.0$.

Ste	T_{avg} (K)	$T_{\max}$ (K)	p_{Mx} (m)	$p_{\text{err}\,x}$ (m)
0.5	0.003857	0.012703	0.810560	-0.000543
1.0	0.001407	0.004705	0.671921	-0.001538
2.0	0.000908	0.002528	0.513854	-0.003082
4.0	0.000742	0.001291	0.335296	-0.002565

Table 6.19: Test 3: Comparison of the maximum nodal temperature error of the LRBFCM with results of the FEM by [Pardo and Weckman, 1996] and the DRBEM by [Šarler and Kuhn, 1998b]. $\text{Pe} = 2.0$, $1/\text{Ste} = 0.7$.

Grid		21×3 $c\cdot r_0 = 1.6\,\text{m}$	41×3 $c\cdot r_0 = 0.8\,\text{m}$	81×3 $c\cdot r_0 = 0.4\,\text{m}$
LRBFCM	$T_{\max}\left(\%\right)$	2.57	1.24	0.41
DRBEM	$T_{\max}\left(\%\right)$	1.21	0.81	0.41
FEM	$T_{\max}\left(\%\right)$	2.15	1.06	0.46

Table 6.20: Test 3: Comparison of the phase-change interface position error of the LRBFCM with results of the FEM by [Pardo and Weckman, 1996] and the DRBEM by [Šarler and Kuhn, 1998b]. $\text{Pe} = 2.0$, $1/\text{Ste} = 0.7$, $p_{Mx} = 0.598739$ m.
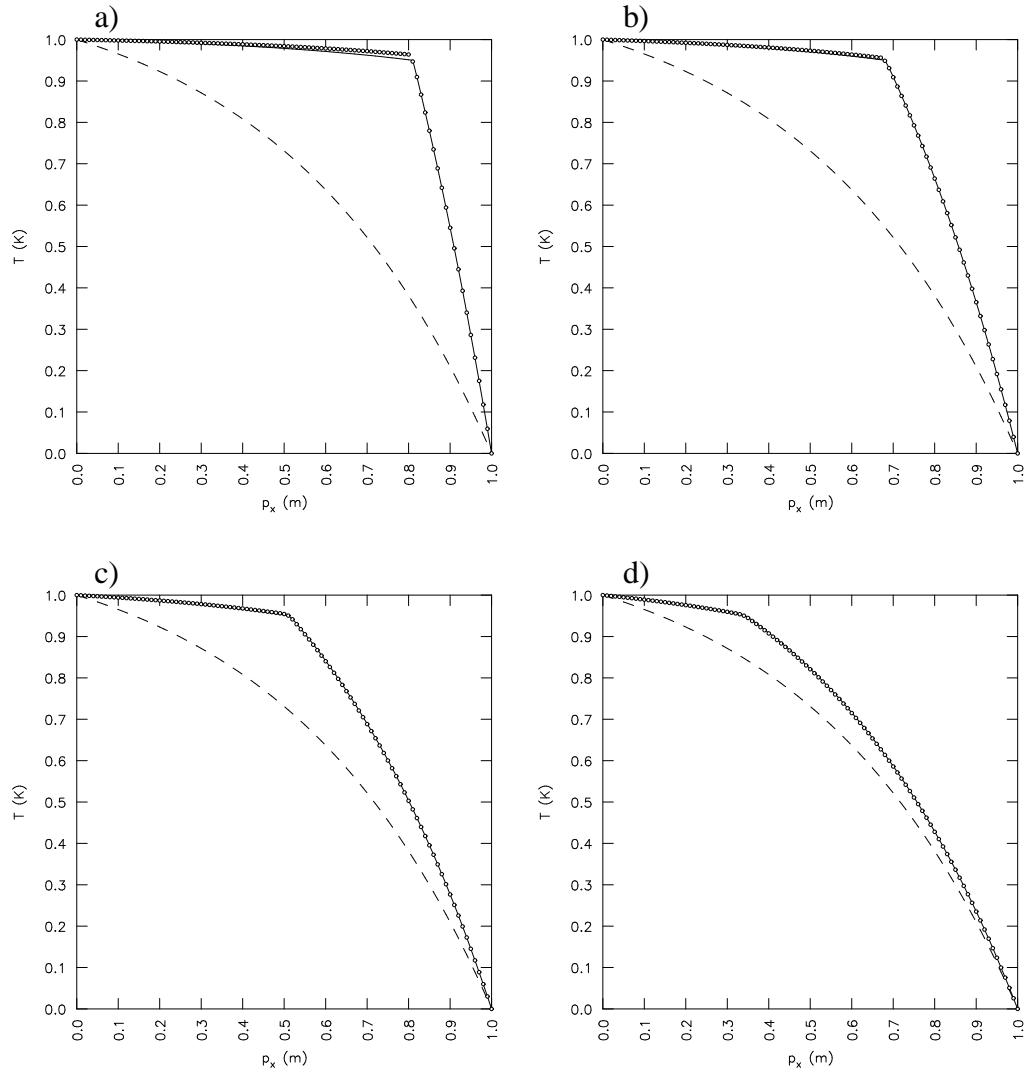
Grid		21×3 $c\cdot r_0 = 1.6\,\text{m}$	41×3 $c\cdot r_0 = 0.8\,\text{m}$	81×3 $c\cdot r_0 = 0.4\,\text{m}$
LRBFCM	$p_{\max\,x}\left(\%\right)$	-1.68	-1.33	-0.94
DRBEM	$p_{\max\,x}\left(\%\right)$	-1.51	-0.77	-0.46
FEM	$p_{\max\,x}\left(\%\right)$	-1.62	-0.82	-0.48

Figure 6.13: Test 3: Comparison of the calculated temperatures ○ in the central nodes $p_y = 0\,\mathrm{m}$ with analytical solution – for different Péclet numbers. Line - - denotes analytical solution with $\mathrm{Ste} = \infty$. Discretization $101{\times}3$. $\mathrm{Ste} = 2.0$. (a) $\mathrm{Pe} = 0.5$, (b) $\mathrm{Pe} = 1.0$, (c) $\mathrm{Pe} = 2.0$ and (d) $\mathrm{Pe} = 4.0$.

Figure 6.14: Test 3: Comparison of the calculated temperatures ○ in the central nodes $p_y = 0$ m with analytical solution – for different Stefan numbers. Line - - denotes analytical solution with $Ste = \infty$. Discretization 101×3. $Pe = 2.0$. (a) $Ste = 0.5$, (b) $Ste = 1.0$, (c) $Ste = 2.0$ and (d) $Ste = 4.0$.
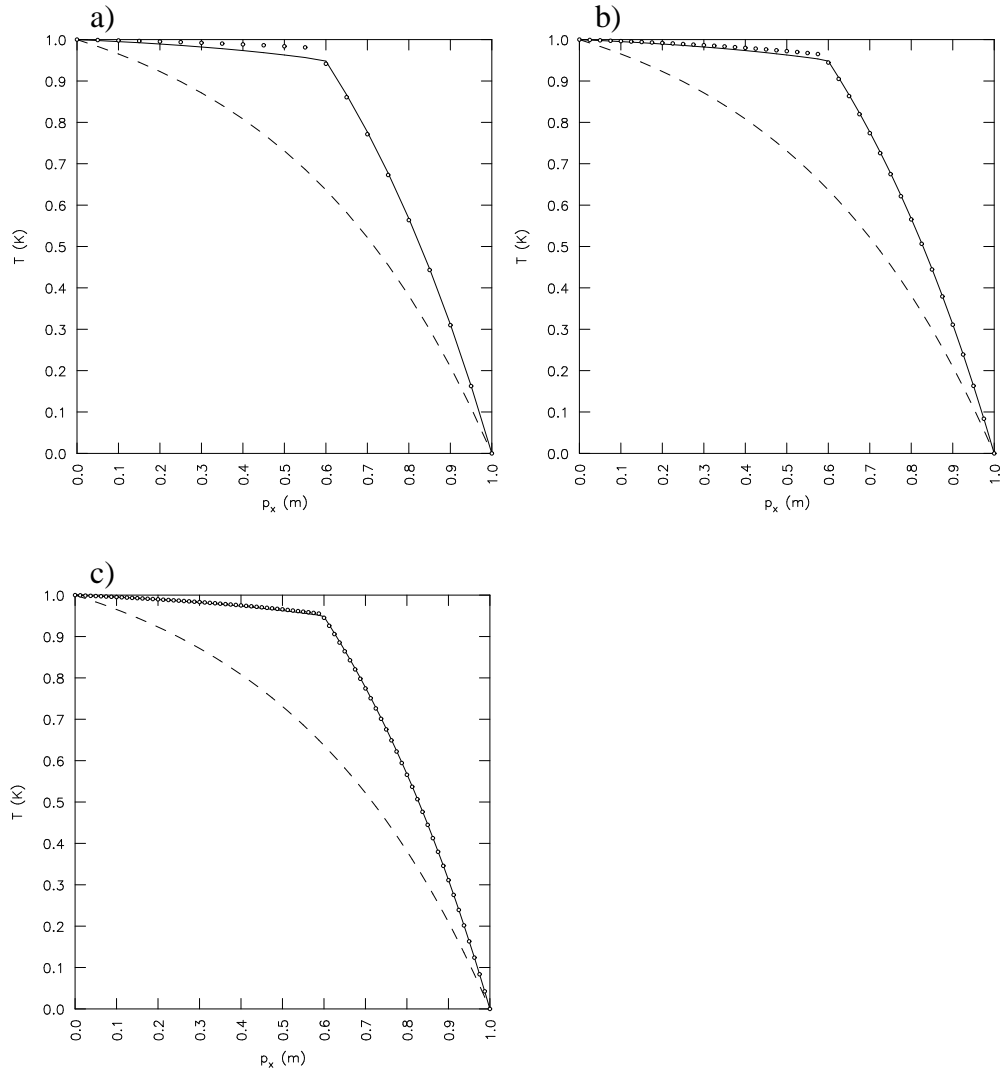
Figure 6.15: Test 3: Comparison of the calculated temperatures ○ in the central nodes $p_y = 0$ m with analytical solution – for test case from [Pardo and Weckman, 1996]. Line - - denotes analytical solution with $Ste = \infty$. $Pe = 2.0$, $1/Ste = 0.7$. Discretization (a) 21×3, (b) 41×3, and (c) 81×3.

Space discretization sensitivity for different material properties of the phases

The thermal conductivities of the solid and liquid phases at the melting point or in the phase-change interval usually do not differ by more than 100 % in pure metals or alloys. Similarly, the related alloy specific heats do not differ by more than 25 % [Brandes and Brook, 1992]. In the present study of the influence of the different material properties on the results of the present numerical method the cases with three times greater or lower thermal conductivity and cases with

two times lower or greater specific heat have been recalculated, which most probably covers all realistic situations. The results of these calculations are presented in Figure 6.16 and Table 6.21. The accuracy of the results does not principally differ from the accuracy of the cases with constant material properties.

Table 6.21: Test 3: Sensitivity of the results with respect to different material properties of the phases. Discretization 101×3, $\mathrm{Pe} = 1.0$, $\mathrm{Ste} = 2.0$.

c_{pS0}	c_{pL0}	k_{S0}	k_{L0}	T_{avg} (K)	$T_{\max}$ (K)	p_{Mx} (m)	$p_{\mathrm{err}\,x}$ (m)
1.0	1.0	1.0	1.0	0.000978	0.002406	0.200251	-0.000161
2.0	1.0	1.0	1.0	0.001478	0.003105	0.331708	-0.001201
1.0	2.0	1.0	1.0	0.000292	0.001009	0.210841	-0.000516
1.0	1.0	3.0	1.0	0.001430	0.006821	0.025634	0.001914
1.0	1.0	1.0	3.0	0.005002	0.012371	0.325451	-0.003810
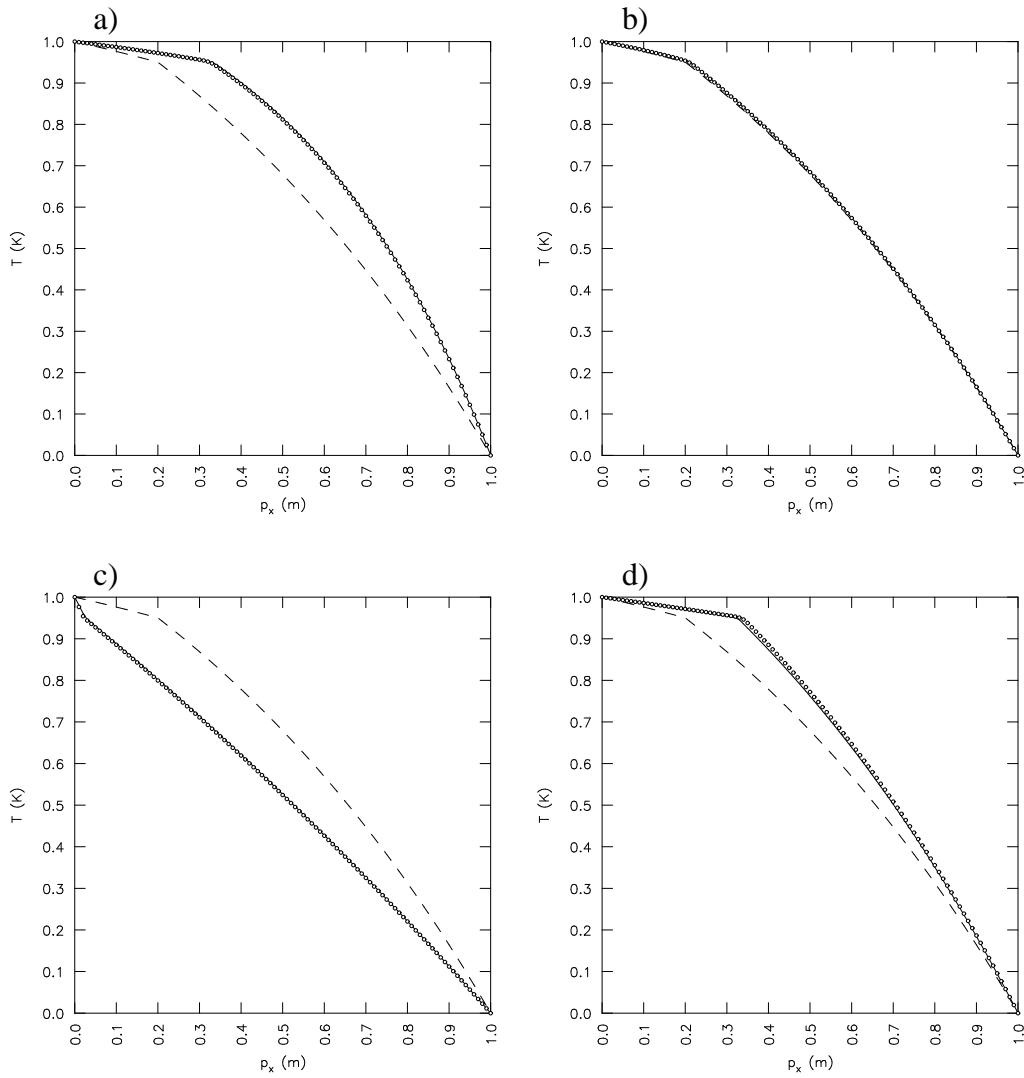
Figure 6.16: Test 3: Comparison of the calculated temperatures $\circ$ in the central nodes $p_y = 0\,\text{m}$ with analytical solution $-$. Line $-\,-$ denotes analytical solution with unit material properties. Discretization 101×3. $\text{Pe} = 1.0$. $\text{Ste} = 2.0$. (a) $c_{pS0} = 2.0\,\text{J/(kgK)}$, (b) $c_{pL0} = 2.0\,\text{J/(kgK)}$, (c) $k_{S0} = 3.0\,\text{W/(mK)}$, and (d) $k_{L0} = 3.0\,\text{W/(mK)}$.

6.4 Test 4: Direct-chill casting problem

6.4.1 Problem description
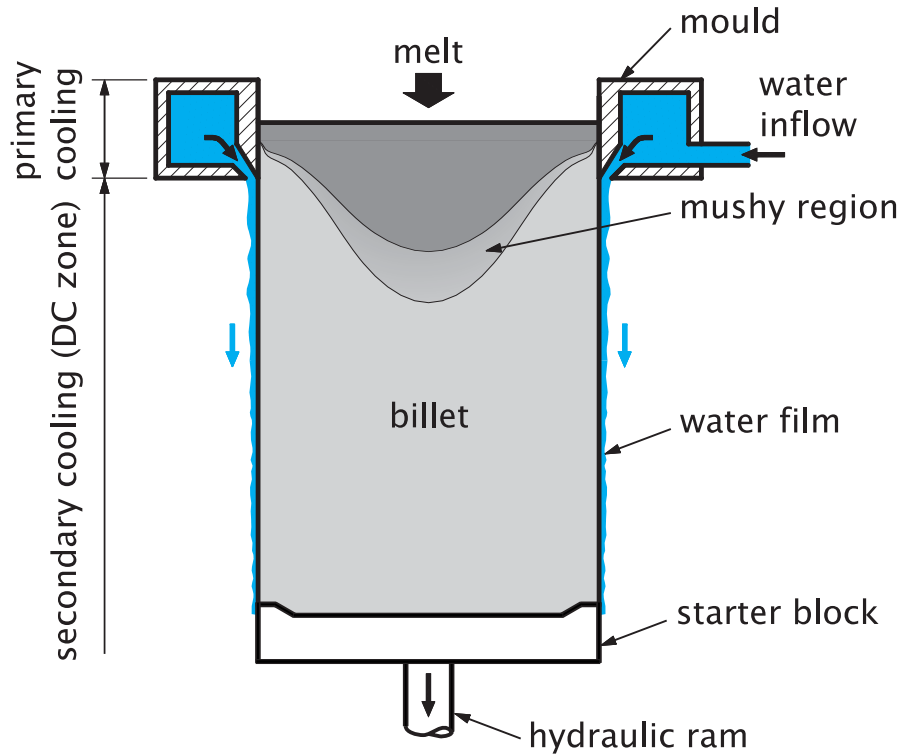
Figure 6.17: Test 4: Scheme of the DC casting process.

Direct chill (DC) casting (Figure 6.17) is currently the most common [Altenpohl, 1998] semi-continuous casting practice in production of aluminium alloys. The process involves molten metal being fed through a bottomless water-cooled mould where it is sufficiently solidified around the outer surface to take the shape of the mould and acquire sufficient mechanical strength to contain the molten core at the centre. As the strand emerges from the mould, water impinges directly from the mould onto the surface (direct-chill), flows over the cast surface and completes the solidification. Related transport, solid mechanics, and phase-change kinetics phenomena are extensively studied [Beckermann, 2000].

6.4.2 Numerical results

The solution of a simplified model of the DC casting process in two dimensions is presented. The numerical results are obtained by the solution procedure defined in Section 5.4. The steady state solution is shown, approached by a false transient calculation using a fixed time-step of $0.5\,$s. The enthalpy reference temperature T_{ref} has been set to $0\,$K. The following simplified DC casting case is considered. The computational domain is a rectangle (coordinates p_x, p_y) $-1.25\,$m$\leq p_y \leq 0\,$m, $0\,$m$\leq p_x \leq 0.25\,$m. The boundary conditions on the top at $p_y = 0\,$m are of the Dirichlet type with $T_\Gamma^D = 980\,$K, and the boundary conditions at the bottom at $p_y = -1.25\,$m are of the Neumann type with $F_\Gamma^N = 0\,$W/m^2. The boundary conditions at the outer surface are of the Robin type with $T_{\Gamma ref}^R = 298\,$K. The heat transfer coefficients between $0\,$m$\leq p_y \leq -0.01\,$m, $-0.0\,$m$\leq p_y \leq -0.06\,$m, $-0.06\,$m$\leq p_y \leq -0.1\,$m, and $-0.1\,$m$\leq p_y \leq -1.25\,$m, are $T_\Gamma^R = 0\,$W/(m^{2}K), $T_\Gamma^R = 3000\,$W/(m^{2}K), $T_\Gamma^R = 150\,$W/(m^{2}K), and $T_\Gamma^R = 4000$ W/(m^{2}K), respectively. Material properties correspond to a simplified Al4.5%Cu alloy as already used in [Šarler and Mencinger, 1999] and [Šarler *et al.*, 2005]: $\rho_0 = 2982\,$kg/m^3, $k_S = 120.7\,$W/(mK), $k_L = 57.3\,$W/(mK), $c_{pS} = 1032\,$J/(kgK), $c_{pL} = 1179\,$J/(kgK), $h_m = 348.2\,$kJ/kg, $T_S = 775\,$K, $T_L = 911\,$K. The liquid fraction increases linearly between T_S and T_L. The initial conditions are described by a linear variation of the temperature with the p_x coordinate from 298 K at the bottom to 980 K at the top of the cylinder. The uniform casting velocity is $v_{Sy} = v_{Ly} = -0.000633\,$m/s, $v_{Sx} = v_{Lx} = 0\,$m/s. The solution has been obtained on an uniform $27\times127-4$ (denoted as I) and $52\times252-4$ (denoted as 2) node arrangements as well as randomly displaced node arrangement I, where -4 means without corner nodes. A schematic of the uniform node arrangement I is shown in Figure 6.18(left). A non-uniform node arrangement is generated from the uniform node arrangement through transformation

$$p_{n\varsigma(\text{nonuniform})} = p_{n\varsigma(\text{uniform})} + c_{\text{random}}\, \delta r_{\min}\, p_{n\varsigma(\text{uniform})} \; ; \; \varsigma = x, y \qquad (6.8)$$

where c_{random} represents a random number $-1 \leq c_{\text{random}} \leq +1$, δ represents a displacement factor (in this work fixed to 0.25), and $r_{\min}$ the minimum distance between the two nodes in the uniform node arrangement. Only domain nodes have been subject to this transformation (Figure 6.18 (right)).

The accuracy analysis of the LRBFCM solutions is made by comparison with the FVM, which uses central-difference spatial discretization and explicit time discretization. Tables 6.22 and 6.23 show the average error, the absolute maximum error and the position of absolute maximum error as a function of MQs free parameter for node arrangement I and II, respectively. The best accuracy is reached with the higher values of free parameter, as already

concluded from accuracy analysis in previous tests. Figure 6.19 shows comparison of the temperature distribution for uniform node arrangement I between LRBFCM and FVM results. There is practically no visual difference. The LRBFCM solution was obtained with free parameter $c = 16.0$ and five-noded influence domain. The absolute difference of the same comparison is shown in Figure 6.20. The maximum value is less then $10\,\mathrm{K}$, appeared on the outer surface were the largest temperature gradients appear.

Figure 6.21 represents the absolute difference between the LRBFCM solutions calculated on uniform and non-uniform node arrangements. Despite the randomness of non-uniform node arrangement, the absolute difference is less then $5\,\mathrm{K}$. Results for non-uniform node arrangement was calculated with free parameter $c = 16.0$ and seven-noded influence domain.

The calculated temperature field along the slab at three different casting velocities is shown in Figure 6.22. The results show the expected response of the presented method on the casting velocity variations.

A similar comparison has been performed also with the DAM and FVM in [Šarler *et al*., 2005] with the maximum difference between DAM and FVM about 4 times bigger as in the present method. For the solution of the presented problem with DAM [Šarler *et al.*, 2005], we need 6 polynomial basis and at least 9 nodes in the influence domain which makes this meshless approach also less efficient as the present one.
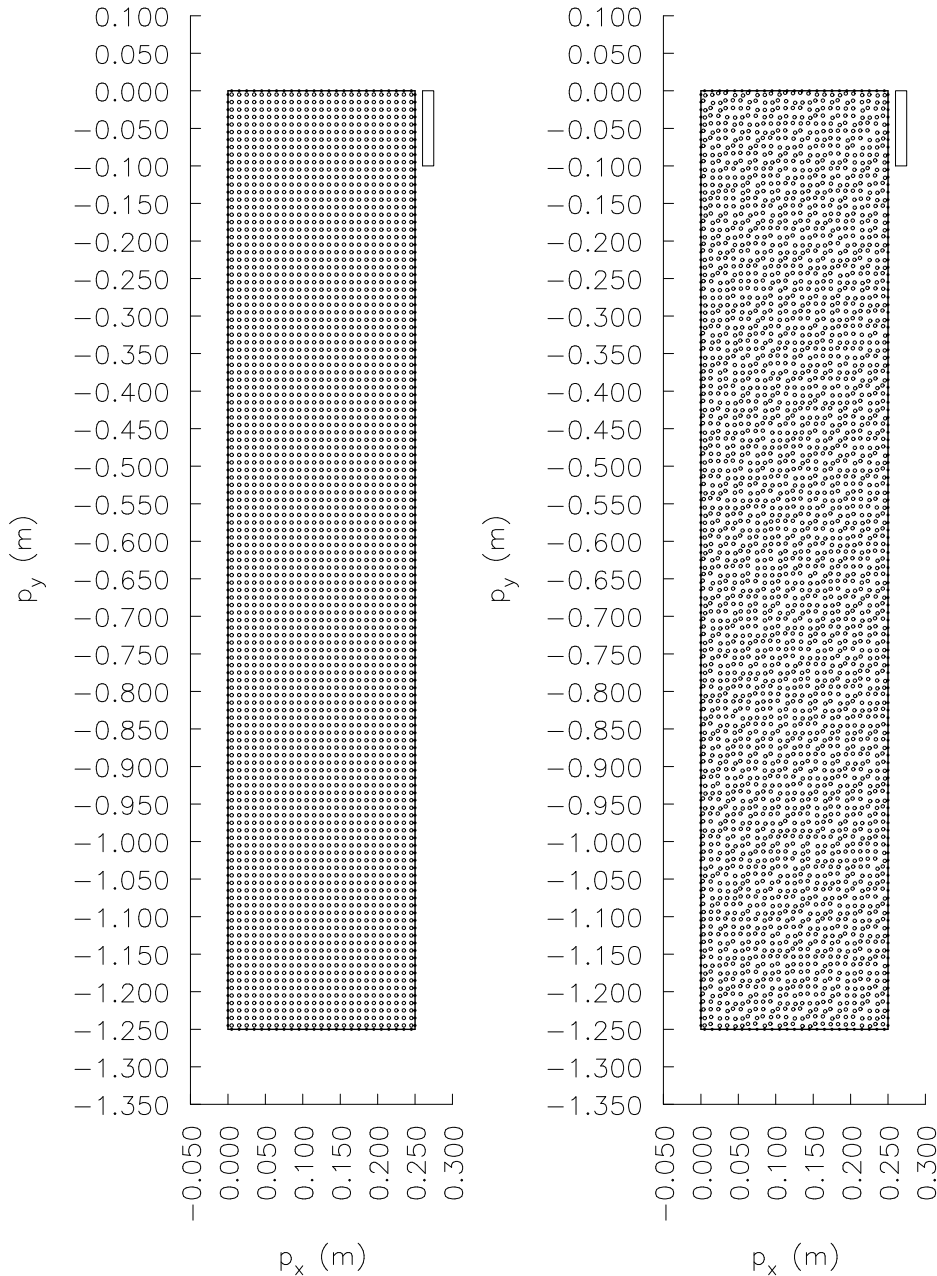
Figure 6.18: Test 4: Node arrangements. Left - uniform node arrangement I. Right - non-uniform randomly displaced node arrangement I. The upper right rectangle schematically represents the mold.
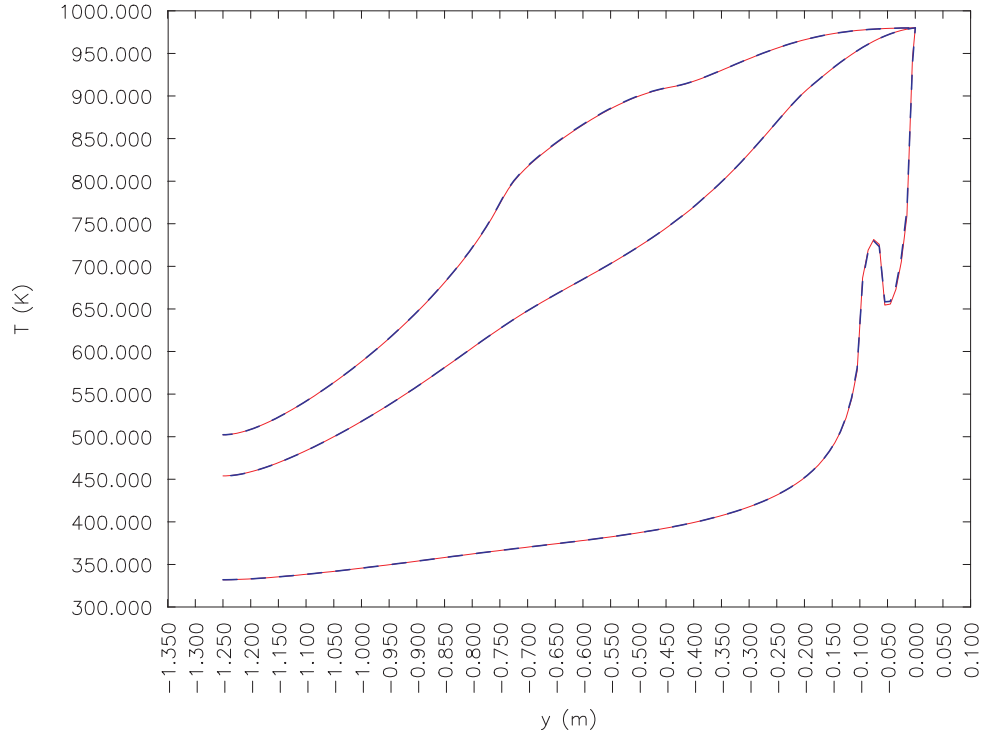
Figure 6.19: Test 4: Calculated temperature distribution in the slab. Node arrangement I. Solid red curve: FVM, dashed blue curve: LRBFCM. Upper curve – centerline temperature, center curve – mid-radius temperature, and lower curve – surface temperature.

Table 6.22: Test 4: Accuracy of the solution as a function of MQs free parameter for node arrangement I. Results compared with the FVM solutions.

c	T_{avg} (K)	T_{max} (K)	$p_{max\,x}$ (m)	$p_{max\,y}$ (m)
4	25.71230	81.2948	0.005	-0.735
8	1.71750	8.1644	0.250	-0.015
16	0.08673	8.2416	0.250	-0.015
32	0.20570	8.2561	0.250	-0.015
64	0.22360	8.2595	0.250	-0.015

Table 6.23: Test 4: Accuracy of the solution as a function of MQs free parameter for node arrangement II. Results compared with the FVM solutions.

c	T_{avg} (K)	T_{max} (K)	$p_{max\,x}$ (m)	$p_{max\,y}$ (m)
4	95.73460	249.27590	0.0025	-0.7225
8	6.80490	24.21560	0.0025	-0.7425
16	0.41530	4.82790	0.2500	-0.0125
32	0.05211	4.84360	0.2500	-0.0125
64	0.08941	4.84660	0.2500	-0.0125
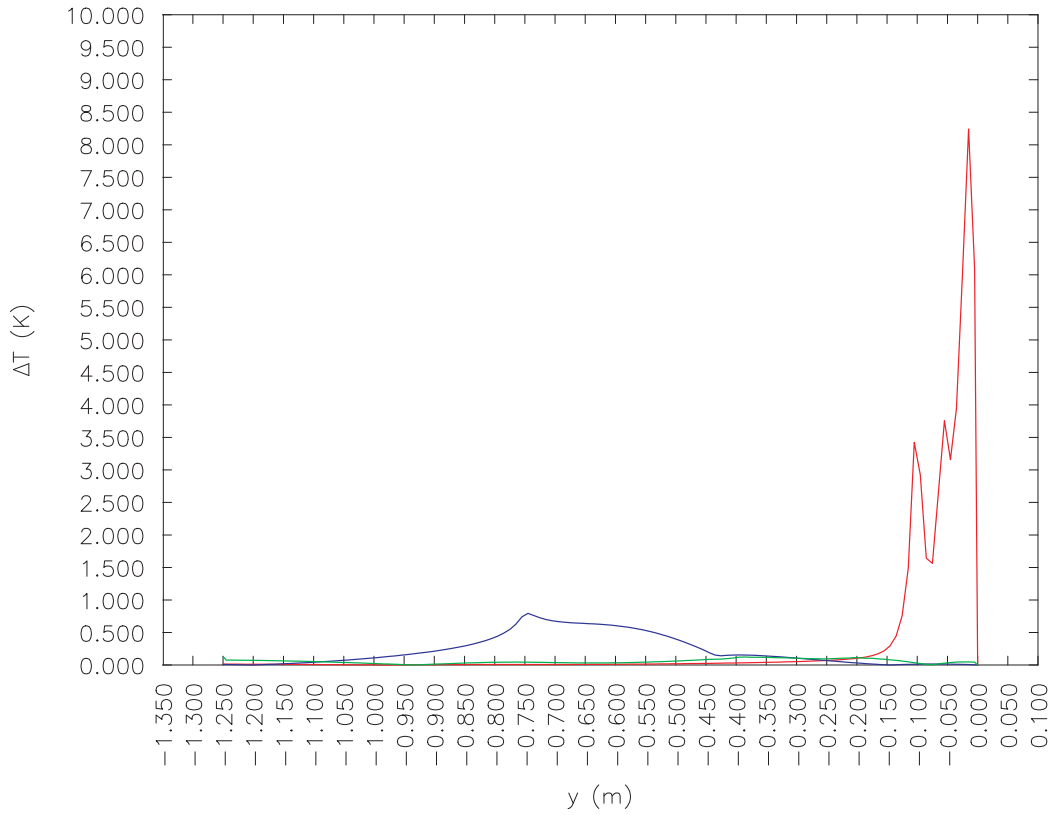
Figure 6.20: Test 4: Absolute difference between the FVM and the LRBFCM solutions. Node arrangement I. Red curve – surface temperature, green curve – mid-radius temperature, and blue curve – centerline temperature.
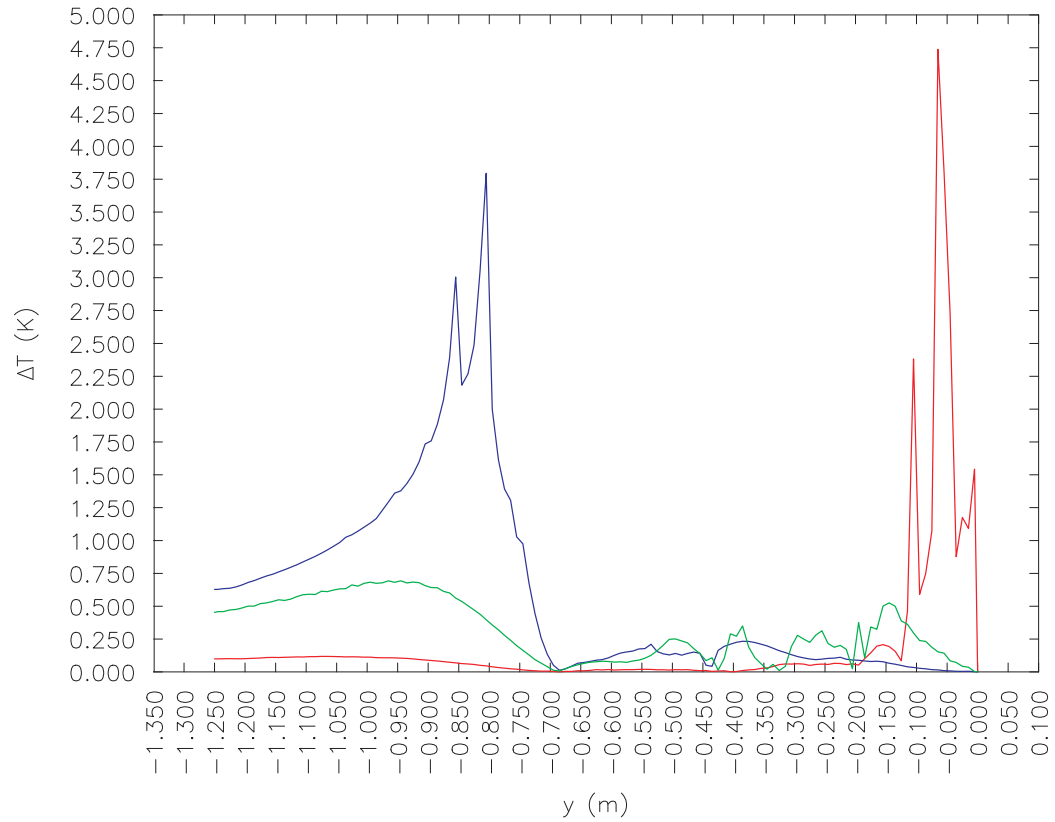
Figure 6.21: Test 4: Absolute difference between the LRBFCM solutions calculated in uniform and non-uniform node arrangements I. Red curve – surface temperature, green curve – mid-radius temperature, and blue curve – centerline temperature.
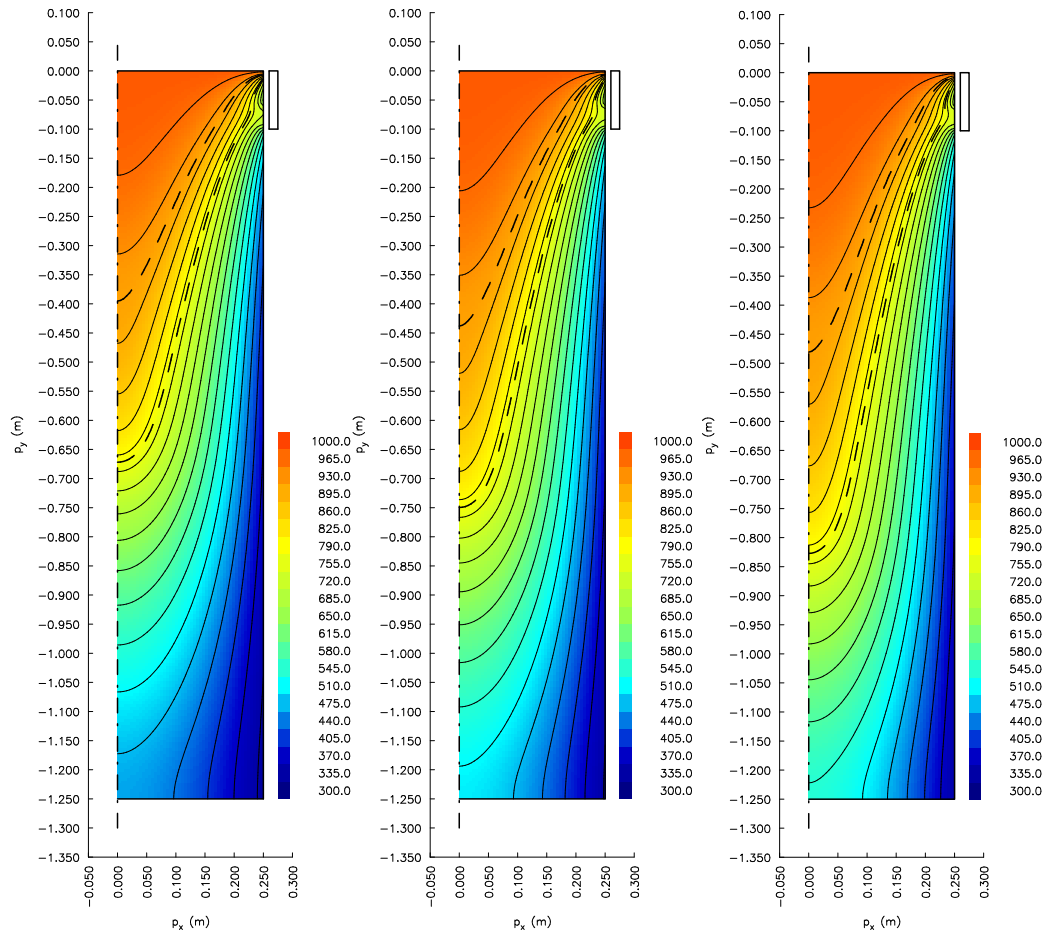
Figure 6.22: Test 4: Temperature field and isotherms in the slab obtained by the LRBFCM. Solidus and liquidus isotherms are dashed. Central figure – nominal casting velocity, left figure – reduced casting velocity for 10 %, right figure – enhanced casting velocity for 10 %. The spacing between the isotherms is 35.0 °C. The first plotted isotherm on the top is at 965.0 K.

6.5 Test 5: Start-up phase simulation of the Direct-chill casting problem

6.5.1 Problem description
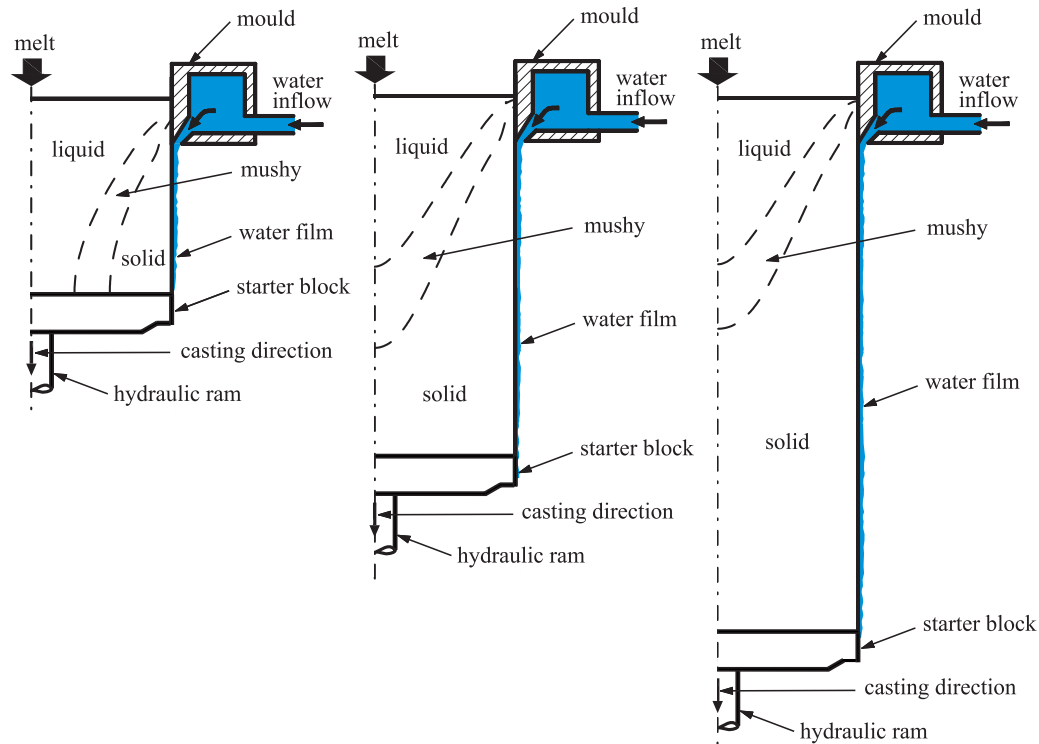
Figure 6.23: Test 5: Scheme of the start-up phase of the DC casting process at different time steps.

A technically crucial phase of the DC casting process is the start-up (or initial) phase, a period from the start of operation until a steady state. The DC casting start-up phase is short (several minutes) compared to the whole casting (several hours). In this phase, the starting block, which is initially in the mould (and carries the whole weight of the ingot throughout the process) starts to move downwards. The steady-state operation is approximately achieved when the starting block moves away from the mould for few typical transversal dimensions of the cast. Although short, this phase is of critical importance for the quality of the final product. In addition to the moving phase-change interface boundary the consideration of the start-up phase involves a moving boundary associated with the movement of the starting block. The numerical modeling and

simulation of the start-up phase serves as a tool for mitigation of several DC casting defects [Williams *et al.*, 2003].

6.5.2 Numerical results

The solution of the same simplified model of the start-up phase of DC casting process in axisymmetry is presented. The numerical results are obtained by the solution procedure defined in Section 5.5. The transient solution is calculated using a fixed time-step of 0.1 s. The MQs free parameter was set to *c=32* in accordance with the study in [Vertnik and Šarler, 2006]. The following simplified DC casting case is considered. The initial computational domain is a cylinder (coordinates p_z, p_r) $-0.01 \text{m} \le p_z \le 0 \text{m}$, $0 \text{m} \le p_r \le 0.25 \text{m}$. The boundary conditions on the top at $p_z = 0 \text{m}$ are of the Dirichlet type with $T_\Gamma^D = 980 \text{K}$, and the boundary conditions at the moving bottom are of the Neumann type with $F_\Gamma^N = 0 \text{W/m}^2$. The boundary conditions at the outer surface are of the Robin type with $T_{ref}^R = 298 \text{K}$. The heat transfer coefficients between $0 \text{m} \le p_z \le -0.01 \text{m}$, $-0.01 \text{m} < p_z \le -0.06 \text{m}$, $-0.06 \text{m} < p_z \le -0.1 \text{m}$, and $-0.1 \text{m} < p_z \le -1.25 \text{m}$, are $T_\Gamma^R = 0 \text{W/(m}^2\text{K)}$, $T_\Gamma^R = 3000 \text{ W/(m}^2\text{K)}$, $T_\Gamma^R = 150 \text{ W/(m}^2\text{K)}$, and $T_\Gamma^R = 4000 \text{ W/(m}^2\text{K)}$, respectively. Material properties from previous test (Section 6.4) are used. The initial temperature is 980K and uniform in the initial computational domain. The uniform casting velocity is $v_{Sz} = v_{Lz} = -0.000633 \text{m/s}$, $v_{Sr} = v_{Lr} = 0 \text{m/s}$.

The solution has been obtained on two node arrangements that are uniform in p_r direction. The coarser one (denoted as I) includes 25 domain nodes in p_r direction, and the finer one (denoted as II) 50 domain nodes, respectively. The domain nodes that are kept after moving the bottom have the same distance as the nodes in p_r direction. Each of the influence domains contains 5 nodes, as represented in Figure 6.25. The calculated results for times $t = 500 \text{s}$, $t = 1000 \text{s}$, and $t = 1500 \text{s}$ are shown in Figure 6.26. Figure 6.27 shows centerline, mid-radius and surface temperatures, together with the reference FVM solution [Mencinger, 2002], calculated in the same nodes. The FVM model employs the central-difference discretization scheme for convection-diffusion and is thus second-order accurate, which was clearly verified by calculating the observed order of convergence over three grids (25×125, 50×250 and 100×500 nodes). One could observe a slight difference between LRBFCM and FVM results in Figure 6.27(left) where the node arrangement I is used and practically no difference in Figure 6.27(right) where the node arrangement II is used.

In the comparison of the numerical results obtained by the LRBFCM with the 100×500 FVM solution (reference) one can observe very good agreement. The absolute temperature difference between the LRBFCM solution with node

arrangements I and II and the reference solution is shown in Figure 6.28. The comparison was made by RBF interpolation of the meshless solution in FVM nodes. The seemingly large differences that occur in a few nodes are attributed to very small longitudinal shifts of the temperature profile in regions of large gradients. Founding the source of this discrepancy and noting that everywhere else the LRBFCM solution is well inside the error band of the reference, we can conclude a very good accuracy performance of the meshless method and the proposed computation strategy.
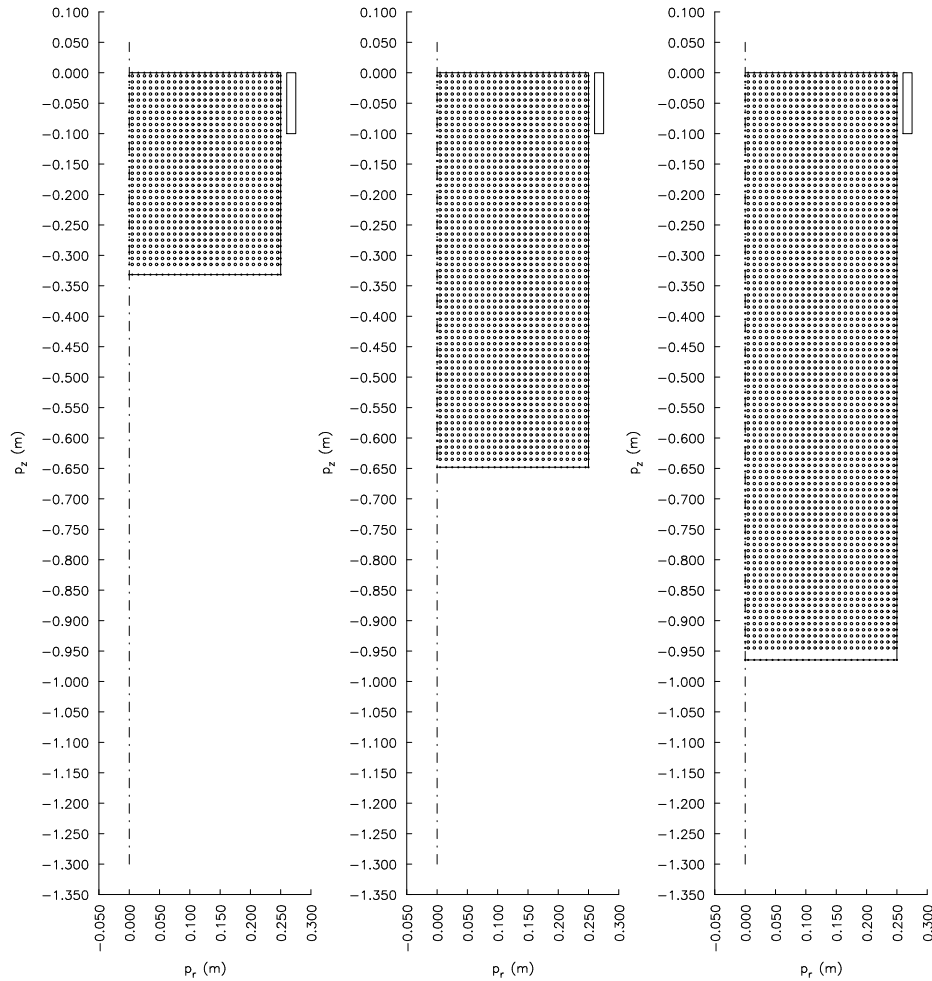
Figure 6.24: Test 5: Distribution of nodes at times $t = 500$ s, $t = 1000$ s, and $t = 1500$ s for the node arrangement I.
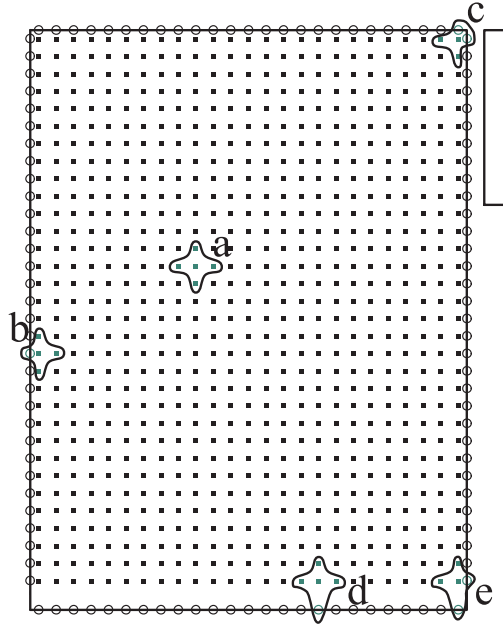
Figure 6.25: Test 5: Four types of different influence domains used in the computations. a) equidistant influence domain, b) boundary influence domain, c) corner influence domain, d) moving boundary influence domain and e) moving corner influence domain.
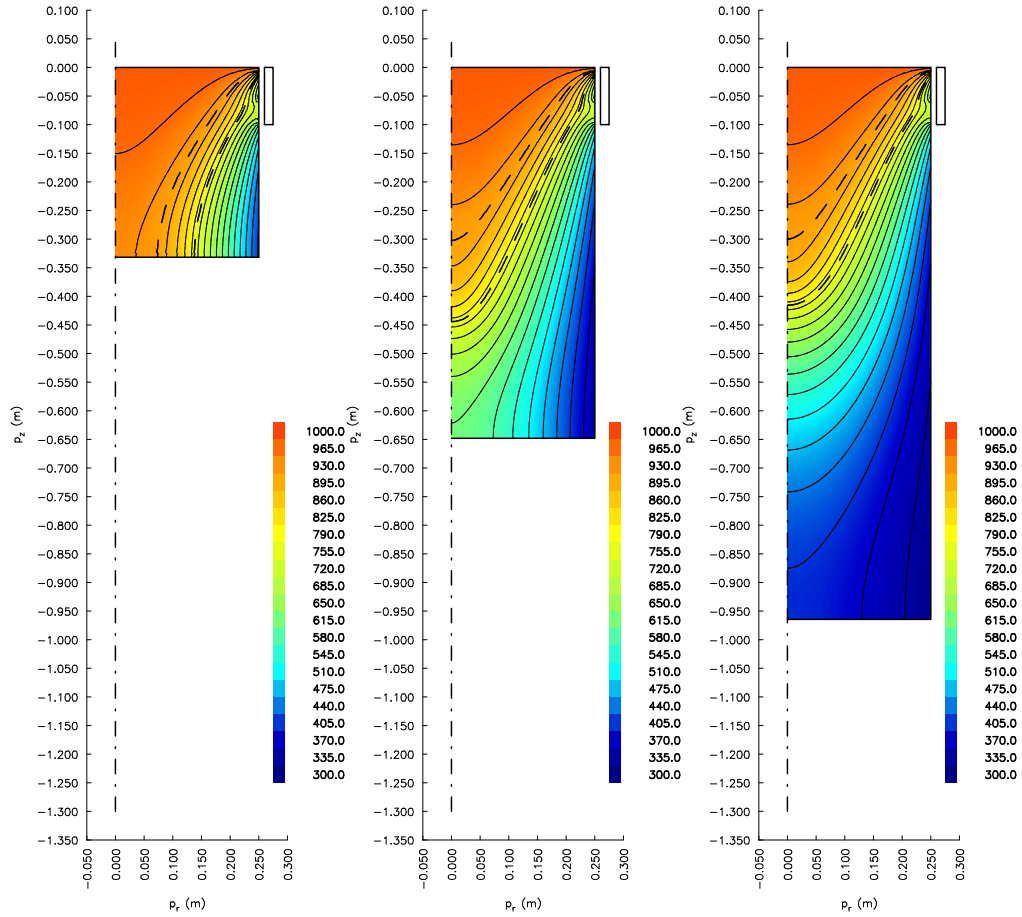
Figure 6.26: Test 5: Temperature field and isotherms of the DC casting start-up phase at times $t = 500$ s, $t = 1000$ s, and $t = 1500$ s calculated with the node arrangement II. The upper dashed line represents the liquidus, and the lower dashed curve the solidus temperature. The spacing between the isotherms is 35 K. The first plotted isotherm on the top is at 965 K.
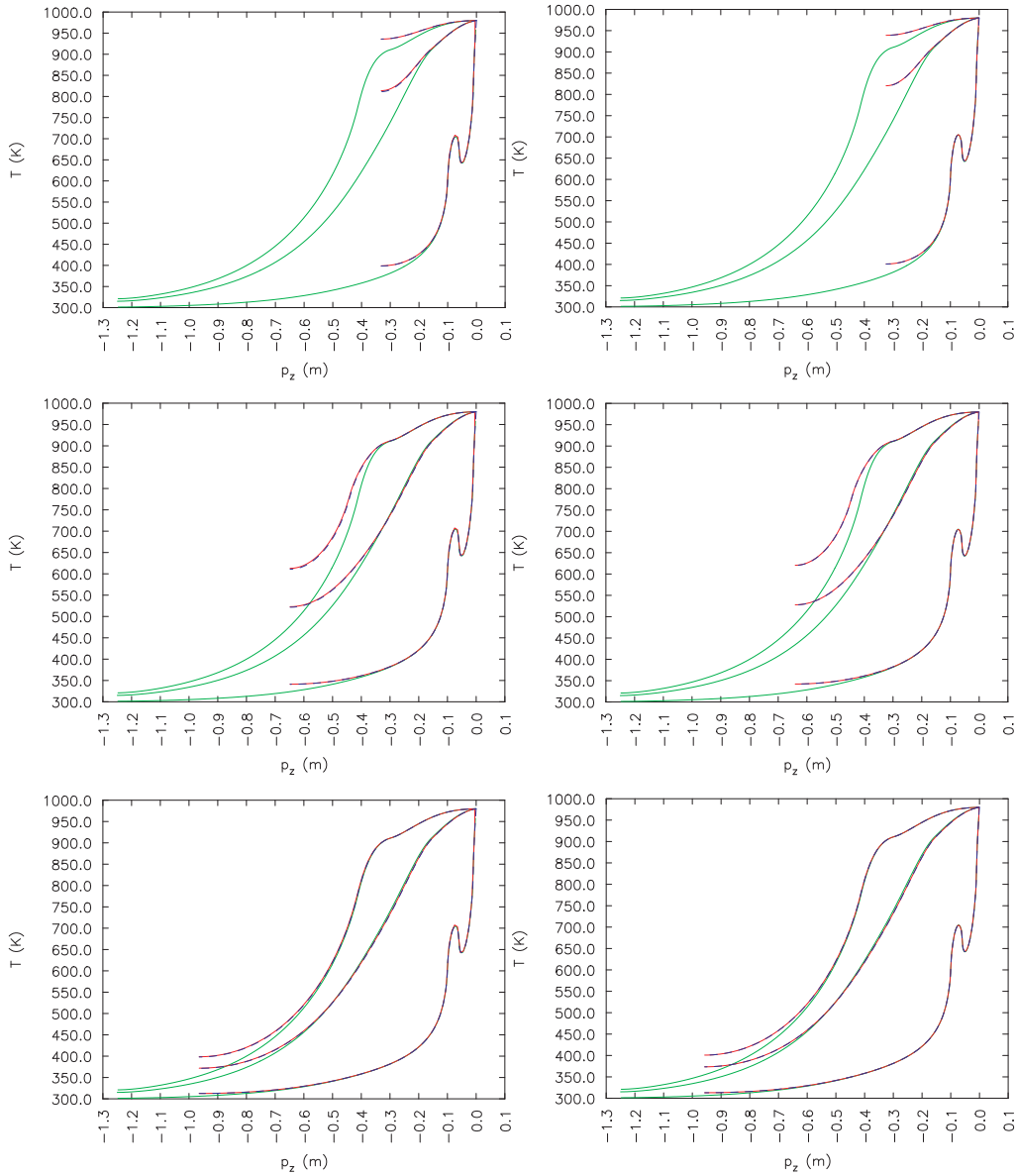
Figure 6.27: Test 5: Comparison of centerline (top), mid-radius (middle), and surface (bottom) temperatures calculated by the LRBFCM (solid red line) and the FVM with 100x500 grid (dashed blue line) at times $t = 500$ s, $t = 1000$ s, and $t = 1500$ s. The thin lines represent the steady-state solution, calculated by the LRBFCM. The left column represents calculations with node arrangement I, and the right one with node arrangement II.
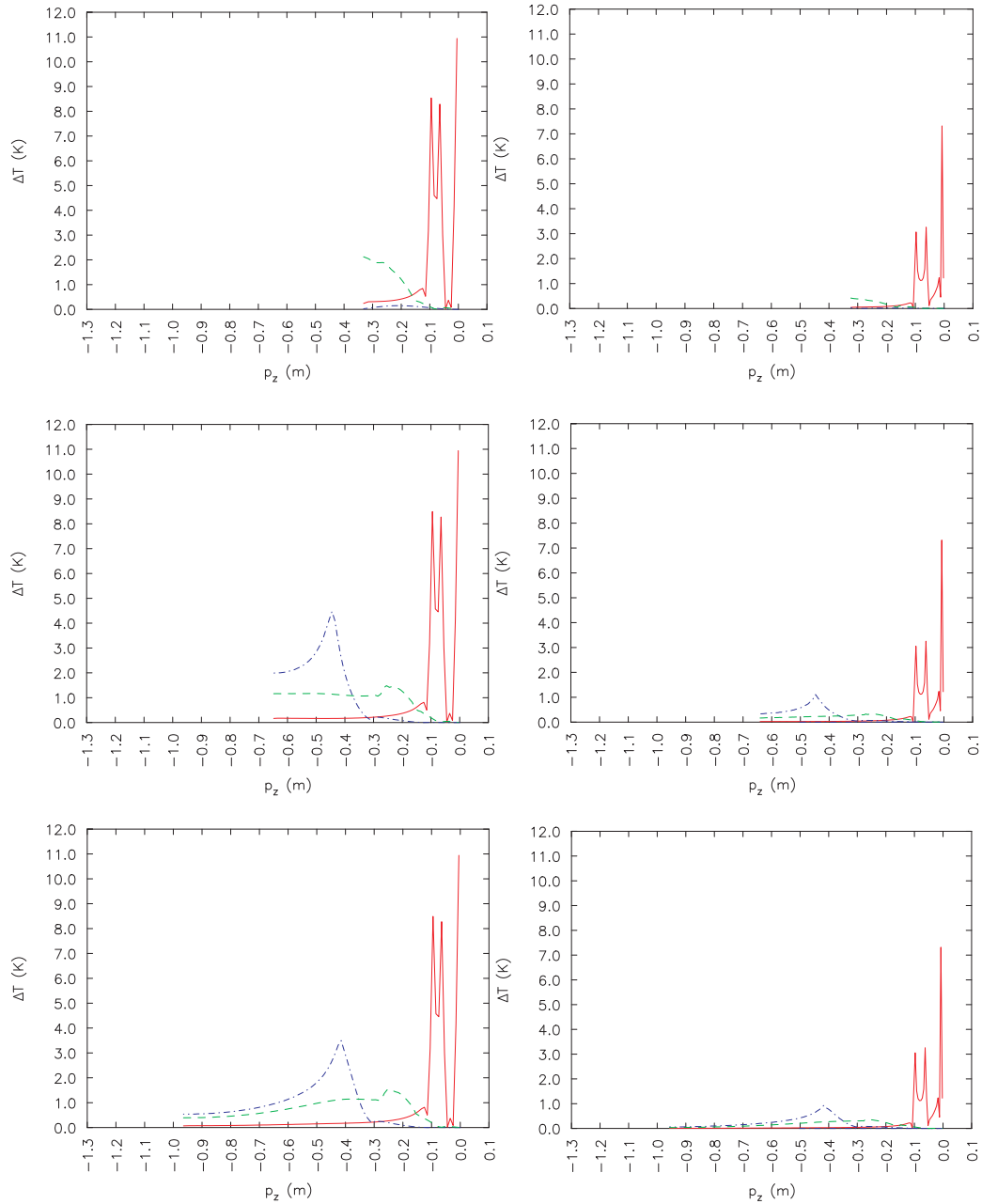
Figure 6.28: Test 5: The absolute temperature difference between the FVM with 100x500 grid and LRBFCM solutions at times $t = 500\,\text{s}$, $t = 1000\,\text{s}$, and $t = 1500\,\text{s}$. Lines represent: red - surface temperature, dashed green – mid-radius temperature and dashed-dot-dashed blue – centerline temperature. Left column represent difference with LRBFCM at node arrangement I and right column LRBFCM at node arrangement II.

7 Conclusions

This work represents a new (very) simple meshless formulation for solving a wide range of diffusion and convection-diffusion problems with phase change. Five numerical tests were presented to demonstrate the accuracy, stability, solvability and applicability of the method. The conclusions can be summarized in the following points:

- The one-domain mixture continuum formulation for solid-liquid phase-change system is used, which has several advantages regarding the multiple-domain formulation. The multiple-domain formulation requires an explicit tracking of the solid-liquid interface, where the node arrangement must be adopted or transformed in a such way, that the solid-liquid interface position is always discretized. This is an inconvenient task, especially for complicated geometries and multi-component alloys. The one-domain formulation reduces the multiple region formulation into a one single conservation equation, which implicitly includes the boundary condition of the phase-change interface. The formulation enables us to use a fixed node arrangement, where complicated geometry with multi-component material can be applied.
- The governing equation is solved in its strong formulation, and hence no numerical integration is required. In a strong formulation, the approximate unknown function should have sufficient degree of consistency, so that it is differentiable up to the order of PDEs. In this work, the unknown functions are approximated by the MQ-RBFs, which are infinitely differentiable.
- The time discretization is performed in a simple explicit way. The method can cope with very large problems since the computational effort grows approximately linear with the number of the nodes. The explicit time discretization form is only conditionally stable, which means that the time step value is restricted. The time step value for the LRBFCM with uniform node arrangements and 5 nodes in influence domains can be determined by the same stability criterions as for FDM. An implicit scheme can also be used where one large and sparse matrix must be filled and solved. Besides this, the matrix is usually not constant over calculation and must be inverted every time step, which is time consuming.

- It was found that the accuracy of the method monotonically increases with larger value of the free parameter. Because of the lack of the suitable theory for determining the proper value of the free parameter one can confidently use the highest values of it, which gives convergence (see all Tests).
- The free parameter in all tests was scaled with the maximal distance between nodes in each influence domain. The scaling is needed in order to use the fixed value of the free parameter for the non-uniform node arrangements. It was interesting to found that the optimal value of the scaled free parameter was almost the same for all presented examples, irrespective of specific properties of each problem.
- The size of each influence domain is presented by the number of nodes. Because the free parameter of the MQ-RBF also depends on the number of nodes in influence domain, we used a fixed number of nodes for all influence domains of the treated numerical examples. It was found out that the best accuracy is obtained with the smallest possible number of nodes in influence domain. For two-dimensional problems this means 5 nodes in each influence domain. Additional studies are required in order to determine the influence of positioning of the nodes at the boundary and domain, particularly for influence domains with more then 5 nodes. We can use more nodes, 9 for example, but then we are loosing accuracy. In examples with non-uniform node arrangements, also presented in this thesis, it is necessary to use more than 5 nodes (see Test 1 and 4). Nevertheless, we observed the same magnitude of the errors as in examples with uniform node arrangements and 5 nodes in influence domains.
- It was shown in the first and second tests, that the LRBFCM is more accurate as the FDM with first-order discretization of boundary conditions. The latter needs approximately four times bigger node arrangement as the LRBFCM to achieve the same order of accuracy. The developed method was also compared with the FVM, where the central-difference discretization scheme was used. The comparisons show that both methods gave approximately the same results at the same node arrangement.
- The developed method is almost independent of the problem dimension. The complicated geometry can easily be coped with. In this work, only the numerical examples with simple rectangular geometries are given. The solutions are obtained on uniform and also non-uniform node arrangements. The non-uniform node arrangements are used for diffusion (Test 1) and DC casting problem (Test 4). It was shown that the accuracy of the solution on the non-uniform node arrangement is almost the same as on uniform node arrangement.

When compared with other mesh-reduction or meshless methods used in the context of the represented examples, one can conclude:

- The method can cope with physically more involved situations than the front tracking BEM (Fic *et al.*, 2000), where the calculations are limited to a uniform velocity field, constant material properties of the phases, and isothermal phase change.
- When compared to DRBEM (Šarler and Kuhn, 1998b), the method does not need any integrations and boundary polygonization.
- The method appears much more efficient as the RBFCM (Kovačević *et al.*, 2003), because it does not require a solution of a large system of equations. Instead, small (5×5, 7×7 and 9×9 used in present work) systems of linear equations have to be solved in each time-step for each node. This feature of the method represents its principal difference from the other related local approaches, where the resultant matrix is large and sparse (Lee *et al.*, 2003; Shu *et al.*, 2003; Tolstykh and Shirobokov, 2005).

The LRBFCM is applicable for simulation of all kinds of diffusion, convection-diffusion, and moving boundary problems. The developments in this work can be straightforwardly extended to tackle other types of partial differential equations. Our work will continue on coupling of energy equation with Navier-Stokes equations.

Appendix A

A.1 Analytical solution of the heat conduction in a rectangle

The problem is posed on a two dimensional rectangular domain $\Omega: p_x^- < p_x < p_x^+$, $p_y^- < p_y < p_y^+$, and boundary $\Gamma_x^-: p_x = p_x^-$, $p_y^- \leq p_y \leq p_y^+$, $\Gamma_x^+: p_x = p_x^+$, $p_y^- \leq p_y \leq p_y^+$, $\Gamma_y^-: p_y = p_y^-$, $p_x^- \leq p_x \leq p_x^+$, $\Gamma_y^+: p_y = p_y^+$ and $p_x^- \leq p_x \leq p_x^+$, shown in Figure A1. The boundary conditions are on the south boundary Γ_y^- of the Dirichlet type with fixed temperature T_y^-, on the east and north boundaries Γ_x^+ and Γ_y^+ of the Robin type with prescribed heat transfer coefficients h_{TC} and zero temperature of the medium, and on the west boundary Γ_x^- of the Neumann type with zero heat flux.
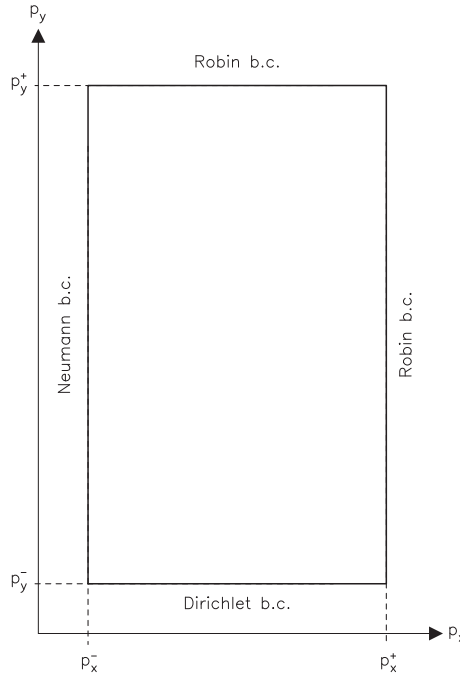
Figure A.1: Problem schematic

97

The analytical solution [Carslaw and Jaeger, 1995] of the test is

$$T_{ana}\left(p_x, p_y\right) = 2h_{TC}T_y^{-} \cdot$$

$$\cdot \sum_{n=1}^{\infty} \frac{\cos \beta_n p_x \left[\beta_n \cosh \beta_n \left(p_y^{+} - p_y\right) + h_{TC} \sinh \beta_n \left(p_y^{+} - p_y\right)\right]}{\cos \beta_n p_x^{+} \left[\left(\beta_n^2 + h_{TC}^2\right) p_x^{+} + h_{TC}\right]\left[\beta_n \cosh \beta_n p_y^{+} + h_{TC} \sinh \beta_n p_y^{+}\right]} \tag{A.1}$$

with β_n representing the positive roots of the equation

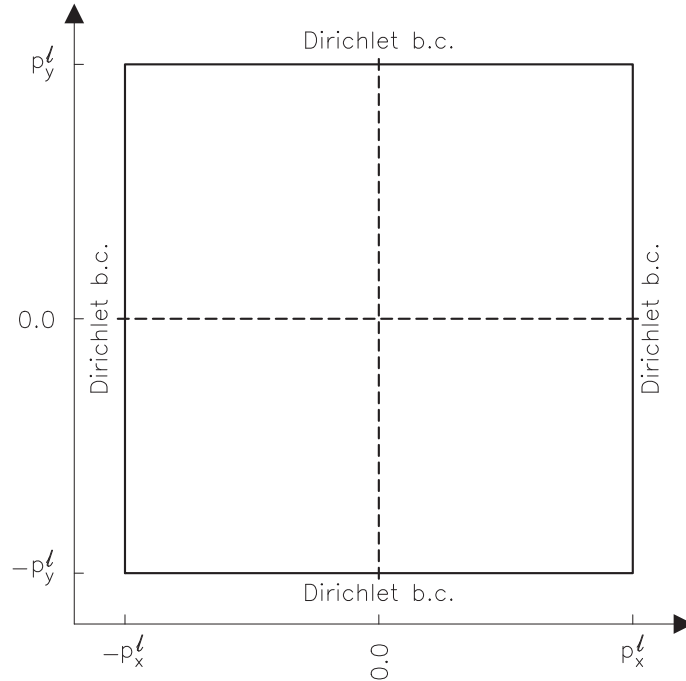$$\beta \tan\left(\beta p_x^{+}\right) = h_{TC} . \tag{A.2}$$

A.2   Analytical solution of the transient heat transfer in the rectangular corner

The geometry of the problem is formally posed on a similar region as the first test case, however the region is square with $p_x^{-} = 0\,\text{m}$, $p_x^{+} = 1.0\,\text{m}$, $p_y^{-} = 0\,\text{m}$, $p_y^{+} = 1.0\,\text{m}$, shown in Figure A2. Boundary conditions on the east Γ_x^{+} and north boundaries Γ_y^{+} are of the Dirichlet type with $T_\Gamma^D = 0\,^0\text{C}$, and on the west Γ_x^{-} and south boundaries Γ_y^{-} are of the Neumann type with $T_\Gamma^N = 0\left(\text{W/m}^2\right)/\left(\text{W/mK}\right)$. The initial conditions are $T_0 = 1\,^0\text{C}$. The analytical solution [Carlsaw and Jaeger, 1995] of the test is

$$T_{ana}\left(p_x, p_y, t\right) = T_{ana}\left(p_x, t\right)T_{ana}\left(p_y, t\right) \tag{A.3}$$

with

$$T_{ana}\left(p_\varsigma, t\right) = \frac{4}{\pi} \sum_{n=1}^{\infty} \frac{-1^n}{2n+1} \exp\left[-\frac{k\left(2n+1\right)^2 \pi^2 t}{4\rho c\left(p_\varsigma^l\right)^2}\right] \cos\left[\frac{\left(2n+1\right)\pi p_\varsigma}{2 p_\varsigma^l}\right]; \varsigma = x, y \tag{A.4}$$

Figure A.2: Initial value problem with boundary conditions and dimensions

A.3   Analytical solution of the convective-diffusive phase-change problem

The exact closed form solution for checking convective-diffusive solid-liquid phase-change problems appears to exist only for a relatively simple one-dimensional steady-state class of problems with uniform velocity field. The solution used by Pardo and Weckman [Pardo and Weckman, 1986] for checking their one-domain FEM-based numerical method belongs to this class of problems. Pardo and Weckman's solution for equal and constant thermal properties of the phases has been generalized by [Šarler and Kuhn , 1998a] to cope with the generally different and constant thermal properties of the solid k_{0S} , c_{0S} and liquid k_{0L} , c_{0L} phase. The extended analytical solution is particularly useful because it allows one to check the proper response of the numerical method regarding the temperature dependence of the material properties. The respective test case is defined as follows: The domain Ω is described by the Cartesian coordinate $p_x^- < p_x < p_x^+$. The boundary conditions at p_x^- and at p_x^+ are of the Dirichlet type with uniform temperatures $T_\Gamma = T_\Gamma^-$ and $T_\Gamma = T_\Gamma^+$. The material moves with the constant uniform velocity $\mathbf{v} = \mathbf{v}_S = \mathbf{v}_L$ with components $\mathbf{v}_x = \mathbf{v}_0$. The boundary temperatures and the isothermal

melting temperature are related by $T_{\Gamma^-} < T_M < T_{\Gamma^+}$. The liquid phase thus occupies the domain between p_x^- and the phase-change interface boundary at p_{Mx}, and the solid phase the domain between p_{Mx} and p_x^+. The corresponding exact temperature distribution in phase $\wp$ has been found [Šarler and Kuhn, 1998b] to be

$$T^{\wp}\left(p_x, p_y\right) = -\frac{\alpha_{\wp}}{v_x}\exp\left(\frac{v_x}{\alpha_{\wp}}p_x + A_P\right) + B_{\wp} \tag{A.5}$$

$$\alpha_{\wp} = \frac{k_{0\wp}}{\rho_0 c_{p0\wp}}; \quad \wp = S, L \tag{A.6}$$

with $\alpha_{\wp}$ denoting the thermal diffusivity of the phase $\wp$; the four constants are

$$A_S = \log\frac{\dfrac{v_x}{\alpha_S}\left(T_M - T_{\Gamma^+}\right)}{\exp\left(\dfrac{v_x}{\alpha_S}p_x^+\right) - \exp\left(\dfrac{v_x}{\alpha_S}p_{Mx}\right)} \tag{A.7}$$

$$A_L = \log\frac{\dfrac{v_x}{\alpha_L}\left(T_M - T_{\Gamma^-}\right)}{\exp\left(\dfrac{v_x}{\alpha_L}p_x^-\right) - \exp\left(\dfrac{v_x}{\alpha_L}p_{Mx}\right)} \tag{A.8}$$

$$B_{\wp} = T_M + \frac{\alpha_{\wp}}{v_x}A_{\wp}\exp\left(\frac{v_x}{\alpha_{\wp}}p_{Mx}\right); \quad \wp = S, L \tag{A.9}$$

The position of the phase-change interface boundary is determined from the transcendental equation

$$-\rho_0 h_M v_x = -k_L\frac{\partial}{\partial p_x}T^L\left(p_{Mx}, p_y\right) + k_S\frac{\partial}{\partial p_x}T^S\left(p_{Mx}, p_y\right) \tag{A.10}$$

It is in this thesis solved by the simple bisection.

Bibliography

Altenpohl, D. G. (1998). *Aluminium: Technology, Applications, and Environment: A profile of a Modern Metal*. Aluminium Association & TMS.

Atluri, S. N. and Shen, S. (2002). *The meshless local Petrov-Galerkin method*. Tech Science Press, Forsyth.

Atluri, S. N. (2004). *The Meshless Method for Domain and BIE Discretisations*. Tech Science Press, Forsyth.

Beckermann, C. (2000). Modeling of macrosegregation: applications and future needs. *International Matarials Reviews*, 47:243-261.

Bennon, W. D. and Incropera, F. P. (1987). A continuum model for momentum, heat and species transport in binary solid-liquid phase change systems - I. Formulation. *International Journal of Heat and Mass Transer*, 30:2161-70.

Brandes, E. A. and Brook, G. B. (1992). *Smithells Metals Reference Book*. Seventh Edition, Butterwoth-Heinemenn, Oxford.

Buhmann, M. D. (2003). *Radial Basis Function: Theory and Implementations*. Cambridge University Press, Cambridge.

Cameron, A. D., Casey, J. A. and Simpson, G. B. (1986). *Benchmark Tests for Thermal Analysis*. NAFEMS National Agency for Finite Element Methods & Standards, Department of Trade and Industry, National Engineering Laboratory, Glasgow.

Carr, J. C., Fright, W. R. and Beatson, R. K. (1997). Surface interpolation with radial basis functions for medical imaging. *IEEE Trans. Medical Imaging*, 16: 96-107.

Car, J. C., Beatson, R. K., Cherrie, J. B., Mitchell, T. J. Fright, W. R., McCallum, B. C. and Evans, T. R. (2001). Reconstruction and representation of 3D objects with radial basis functions. *Proceedings of the 28th annual conference on Computer graphics and interactive techniques,* pages 67-76, ACM Press, New York, USA.

Car, J. C., Beatson, R. K., McCallum, B. C., Fright, W. R., McLennan, T. J. and Mitchell, T. J. (2003). Smooth surface reconstruction from noisy range data. *Proceedings of the 1st international conference on Computer graphics and interactive techniques in Australasia and South East Asia, February 11 - 14, 2003, Melbourne, Australia,* pages 119-126, ACM Press, New York, USA.

Carlsaw, H. S. and Jaeger, J. C. (1995). *Conduction of Heat in Solids - Second Edition*. Clarendon Press, Oxford.

Cecil, T., Qian, J. and Osher, S. (2004). Numerical methods for high dimensional Hamilton-Jacobi equations using radial basis functions. *Journal of Computational Physics*, 196:327-347.

Chen, W. (2002). New RBF collocation schemes and kernel RBFs with applications. *Lecture Notes in Computational Science and Engineering,* 26:75-86.

Crank, J. (1984). *Free and moving boundary problems*. Oxford University Press, Oxford.

Dalhuijsen, A. J. and Segal, A. (1986). Comparison of finite element techniques for solidification problems. *International Journal of Numerical Methods in Engineering,* 29:1807-1829.

Dantzig, J. A. and Tucker III, C. L. (2001). *Modeling in materials processing*. Cambridge University Press, Cambridge.

Divo, E. and Kassab, A.J. (2005). Modeling of convective and conjugate heat transfer by a third order localized RBF meshless collocation method. In Nowak, A.J., Białecki, R.A. and Weçel, G., editors, *Eurotherm 82: Numerical Heat Transfer, September 13-16, 2005, Gliwice-Krakow, Poland*, pages 357-366, Zaklad Graficzny Politehniki Śląskiej, Gliwice.

Fasshauer, G. E. (1997). Solving partial differential equations by collocation with radial basis functions. In Mehaute, A.L., Rabut, C. and Schumaker, L.L., editors, *Surface Fitting and Multiresolution Methods*, pages 131-138.

Fic, A., Nowak, A. J. and Białecki, R. (2000). Heat transfer analysis of the continuous casting process by the front tracking BEM. *Engineering Analysis with Boundary Elements*, 24:215-23.

Franke, R. (1982). Scattered data interpolation: Tests of some methods. *Mathematics of Computation*, 38(157): 181-200.

Hardy, R. L. (1971). Multiquadric equations of topography and other irregular surfaces. *Journal of Geophysical Research*, 76:1905-1915.

Hong, C. P. (2004). *Computer modelling of heat and fluid flow in materials processing*. Institute of Physics Publishing, London.

Kansa, E. J. (1990a). Multiquadrics – a scattered data approximation scheme with applications to computational fluid dynamics - I. Surface approximation and partial derivative estimates. *Computers and Mathematics with Application*, 19:127-145.

Kansa, E. J. (1990b). Multiquadrics – a scattered data approximation scheme with applications to computational fluid dynamics - II. Solutions to parabolic, hyperbolic and elliptic partial differential equations. *Computers and Mathematics with Application* 19:147-161.

Kovačević, I., Poredoš, A. and Šarler, B. (2003). Solving the Stefan problem by the RBFCM. *Numeical Heat Transfer B,* 44B:1-24.

Lee, C. K., Liu, X. and Fan, S. C. (2003). Local muliquadric approximation for solving boundary value problems. *Computational Mechanics,* 30:395-409.

Liu, G. R. (2003). *Mesh Free Methods*. CRC Press, Boca Ratorn.

Liu, G. R. and Gu, Y. T. (2005). *An Introduction to Meshfree Methods and Their Programming*. Springer, Netherlands.

Mai-Duy, N. and Tran-Cong, T. (2001). Numerical solution of Navier-Stokes equations using multiquadric radial basis function networks. *Neural Networks* 14:185-199.

Mai-Duy, N. and Tran-Cong, T. (2001). Numerical solution of differential equations using multiquadrics radial basis function networks. *International Journal for Numerical Methods in Engineering*, 23:1807-1829.

Mai-Duy, N. and Tran-Cong, T. (2002). Mesh-free radial basis function network methods with domain decomposition for approximation of functions and numerical solution of Poisson's equations. *Engineering Analysis with Boundary Elements*, 26:133-156.

Mai-Duy, N. and Tran-Cong, T. (2003). Indirect RBFN method with thin plate splines for numerical solution of differential equations. *Computer Modeling in Engineering & Sciences*, 4:85-102.

Mencinger, J. (2002). Calculation of transient temperature field during semicontinuous casting of aluminium. In Škerget, L. and Marn, J., editors, *Proceedings Kuhljevi dnevi '02, Ribno pri Bledu, September 26.-27. 2002,* pages 81-88, Slovenian Society for Mechanics, Ljubljana.

Minkowycz, W. J. and Sparrow, E. M. (1997). *Advances in numerical heat transfer: Volume 1*. Taylor & Francis.

Nayroles, B., Touzot, G. and Villon, P. (1991). L'approximation diffuse. *Mecanique des Millieux Continus*, 2:293-296.

Özisik, M. N. (1994). *Finite difference methods in heat transfer*. CRC Press, Boca Raton, Florida.

Pardo, E. and Weckman, D. C. (1986). A fixed grid finite element technique for modelling phase change in steady-state conduction-advection problems. *International Journal for Numerical Methods in Engineering*, 23:1807-1829.

Power, H. and Barraco, W. A. (2002). Comparison analysis between unsymmetric and symmetric RBFCMs for the numerical solution of PDF's. *Computers and Mathematics with Applications*, 43:551-583.

Ragone, D. V. (1995). *Thermodynamics of materials*. John Wiley & Sons, Canada.

Roache, P. J. (1998). *Verification and Validation in Computational Science and Engineering*. Hermosa, Albuquerque.

Sadat, H. and Couturier, S. (2000). Performance and accuracy of a meshless method for laminar natural convection. *Numerical Heat Transfer B*, 37B:455-467.

Schaback, R. (1995). Error Estimates and Condition Numbers for Radial Basis Function Interpolation. *Advances in Computational Mathematics*, 3:251-264.

Shu, C., Ding, H. and Yeo, K. S. (2003). Local radial basis function-based differential quadrature method and its application to solve two-dimensional incompressible Navier-Stokes equations. *Computer Methods in Applied Mechanics and Engineering,* 192:941-954.

Šarler, B. (1995). Stefan's work on solid-liquid phase changes. *Engineering Analysis with Boundary Elements*, 16:83-92.

Šarler, B. (1996). Numerical procedure for calculating temperature field in continuous casting of steel. *Materials and Technology,* 30:217-223.

Šarler, B. and Kuhn, G. (1998a). Dual reciprocity boundary element method for convective-diffusive solid-liquid phase change problems, Part 1. Formulation. *Engineering Analysis with Boundary Elements*, 21:53-63.

Šarler, B. and Kuhn, G. (1998b). Dual reciprocity boundary element method for convective-diffusive solid-liquid phase change problems, Part 2. Numerical examples. *Engineering Analysis with Boundary Elements*, 21:65-79.

Šarler, B. and Mencinger, J. (1999). Solution of temperature field in DC cast aluminium alloy billet by the dual reciprocity boundary element method. *International Journal of Numerical Methods in Heat and Fluid Flow*, 9:267-297.

Šarler, B. and Perko, J. (2001). DRBEM solution of temperatures and velocities in DC cast aluminium slabs. In Brebbia, C.A., Kassab, A.J., Chopra, M.B. and Divo, E., editors, *Boundary element technology XIV*, pages 357-369, WIT Press, Southampton.

Šarler, B. (2004). *Chapter 9: Meshless Methods*. In Nowak, A.J., editor, *Advanced Numerical Methods in Heat Transfer*, pages 225-247, Silesian Technical University Press, Gliwice.

Šarler, B. (2005). A radial basis function collocation approach in computational fluid dynamics. *Computer Modeling in Engineering and Sciences*, 7:185-193.

Šarler, B. and Vertnik, R. (2005). Solution of the transient direct chill casting problem with simultaneous material and interphase moving boundaries by the local radial basis function collocation technique. In Chakrabarti, S. K., Hernández, S. and Brebbia, C. A., editors, *Fluid structure interaction and moving boundary problems*, pages 607-617, WIT Press, Southampton.

Šarler, B. and Vertnik, R. (2006). Meshfree explicit radial basis function collocation method for diffusion problems. *Computers and Mathematics with Applications*, 51:1269-1282.

Šarler, B., Kovačević, I. and Chen, C. S. (2004). A mesh-free solution of temperature in direct-chill cast slabs and billets. In Mammoli, A.A. and Brebbia, C.A., editors, *Moving Boundaries VII,* pages 271-280, WIT Press, Southampton.

Šarler, B., Perko, J. and Chen, C. S. (2004). Radial basis function collocation method solution of natural convection in porous media. *International Journal of Numerical Methods for Heat & Fluid Flow*, 14:187-212.

Šarler, B., Vertnik, R. and Perko, J. (2005). Application of Diffuse Approximate Method in Convective-Diffusive Solidification Problems. *Computers, Materials, Continua*, 2:77-83.

Tolstykh, A. I. and Shirobokov, D. A. (2003). On using radial basis functions in a "finite difference" mode with applications to elasticity problems. *Computational Mechanics,* 33:68-79.

Vertnik, R., Perko, J. and Šarler, B. (2004). Solution of temperature field in DC cast aluminium alloy billet by the Diffuse Approximate Method. *Materials and Technology,* 38:257-261.

Vertnik, R. and Šarler, B. (2005). Solution of the heat transfer model of the start-up phase of the direct chill casting process by a meshless numerical method. In Nowak, A. J., Wecel, G. and Bialecki, R. A., editors, *Eurotherm Seminar 82 : numerical heat transfer 2005, September 13-16, Gliwice-Cracow, Poland*, pages 367-376, Institute of Thermal Technology, Silesian University of Technology, Gliwice.

Vertnik, R. and Šarler, B. (2006). Meshless local radial basis function collocation method for convective-diffusive solid-liquid phase change problems. *International Journal of Numerical Methods for Heat & Fluid Flow*, 16:617-640.

Vertnik, R., Založnik, M. and Šarler, B. (2006). Solution of transient direct-chill aluminium billet casting problem with simultaneous material and interphase moving boundaries by a meshless method. *Engineering analysis with boundary elements*, 30:847-855.

Voller, V. R., Swaminathan, S. and Thomas, B. G. (1990). Fixed-grid techniques for phase change problems: a review. *Internatinal Journal for Numerical Methods in Engineering*, 30:875-898.

Wang, J.G. and Liu, G.R. (2002). On the optimal shape parameter of radial basis functions used for 2D meshless method. *Computer Methods in Applied Mechanics and Engineering*, 26:2611-2630.

Williams, A.J., Croft, T.N. and Cross, M. (2003). Modelling of ingot development during start-up phase of direct chill casting. *Metallurgical and Materials Transactions*, 34B:727-734.

Založnik, M. (2006). *Modeling of macrosegregation in direct chill casting*, PhD thesis, University of Nova Gorica.

Zhang, X., Song, K. Z., Lu, M. W. and Liu, X. (2000). Meshless methods based on collocation with radial basis functions. *Computational Mechanics*, 26:333-343.

Zienkiewicz, O.C. and Taylor R.L. (2000). *The finite element method, Volume 1, The basics*. Butterworth-Heinemann, Woburn.